MULTI-OBJECTIVE DESIGN OF DYNAMIC WIRELESS CHARGING SYSTEMS FOR HEAVY – DUTY VEHICLES

by

Akhil Prasad

A Thesis

Submitted to the Faculty of Purdue University

In Partial Fulfillment of the Requirements for the degree of

Master of Science in Electrical Engineering

School of Electrical and Computer Engineering

West Lafayette, Indiana

December 2020

THE PURDUE UNIVERSITY GRADUATE SCHOOL
STATEMENT OF COMMITTEE APPROVAL

Dr. Steven D. Pekarek, Chair

School of Electrical and Computer Engineering

Dr. Dionysios Aliprantis

School of Electrical and Computer Engineering

Dr. Shreyas Sundaram

School of Electrical and Computer Engineering

Approved by:

Dr. Dimitrios Peroulis

Dedicated to my mother.

ACKNOWLEDGMENTS

I would like to express my gratitude towards Dr. Steve Pekarek for guiding me in this research with his novel ideas. I am highly indebted to him for helping me understand the problems associated with my research and suggesting methods to solve them.

I would also like to thank Dr. Dionysios Aliprantis for his valuable contributions to the project. I would also like to thank Dr. Shreyas Sundaram for serving in my committee.

I would like to thank my friends Diala, Theodora and Ethan for the fun times we had while working in the project team. I would also like to thank Pallavi and Tim for their constant support.

Finally, I would like to thank my mother without whose encouragement and support I would not have been able to complete this research.

TABLE OF CONTENTS

LIST OF TABLES

LIST OF FIGURES

ABSTRACT

Presently, internal combustion engines provide power to move the majority of vehicles on the roadway. While battery-powered electric vehicles provide an alternative, their widespread acceptance is hindered by range anxiety and longer charging/refueling times. Dynamic wireless power transfer (DWPT) has been proposed as a means to reduce both range anxiety and charging/refueling times. In DWPT, power is provided to a vehicle in motion using electromagnetic fields transmitted by a transmitter embedded within the roadway to a receiver at the underside of the vehicle. For commercial vehicles, DWPT often requires transferring hundreds of kW through a relatively large airgap (> 20 cm). This requires a high-power DC-AC converter at the transmitting end and a DC-AC converter within the vehicle.

In this research, a focus is on the development of models that can be used to support the design of DWPT systems. These include finite element-based models of the transmitter/receiver that are used to predict power transfer, coil loss, and core loss in DWPT systems. The transmitter/receiver models are coupled to behavioral models of power electronic converters to predict converter efficiency, mass, and volume based upon switching frequency, transmitter/receiver currents, and source voltage. To date, these models have been used to explore alternative designs for a DWPT intended to power Class 8-9 vehicles on IN interstates. Specifically, the models have been embedded within a genetic algorithm-based multi-objective optimization in which the objectives include minimizing system mass and minimizing loss. Several designs from the optimization are evaluated to consider practicality of the proposed designs.

1. INTRODUCTION

With the world witnessing the effects of climate change, it is important to take steps towards cleaner energy future. One of the biggest steps in this direction is the replacement of internal combustion engine (ICE) vehicles with battery electric vehicles (BEV). Currently the ICE vehicles overwhelm BEVs in sales and production with more than 90% of the vehicle sales in 2019 being ICE vehicles [1]. The use of conventional fuel in ICE vehicles results in the emission of greenhouse gases and harmful particles. Furthermore, the mining of the petroleum resources again entails the use of fossil fuels. On the other hand, BEVs can present a much cleaner alternative and also possess a much higher well to wheel efficiency [2]. However, the BEVs possess the following disadvantages compared to their ICE counterparts:

1. Lower energy density of power source
2. Range anxiety
3. Longer charging (refueling) times

The above-mentioned problems become much more pronounced when the vehicle size increases from passenger cars to heavy duty trucks. In an effort to address these shortcomings, battery charging through dynamic wireless power transfer (DWPT) is being considered. In contrast to stationary charging systems, the DWPT system charges the vehicle while the vehicle is in motion. This alleviates the problems of range anxiety, on board battery size and reduces the need for vehicles to stop at charging stations and encounter the long charging periods. Since DWPT systems are designed to charge vehicles while in motion, the transmitter for this system are located within the roadways.

DWPT systems can be classified into capacitive power transfer (CPT) and inductive power transfer (IPT) systems. CPT systems achieve power transfer by means of electric fields whereas IPT systems employ magnetic fields. Both CPT and IPT systems consist of transmitters embedded within the roadway and receivers within the vehicle. For CPT systems, the transmitter and receiver consist of a simple metallic plate and power supply cables. For IPT systems, the transmitter and receiver consist of a magnetically permeable core and associated windings.

Since DWPT systems are meant for charging BEVs while in motion, the air gap between the transmitter and the receiver is large. This large air gap results in substantial power loss thereby

decreasing the efficiency of the system. To reduce the loss, compensation circuits are employed at both the transmitter and the receiver. Furthermore, in order to transfer power through the large air gap, high frequency power electronic converters are required at both the transmitter and receiver side.

Each part of the DWPT system – the transmitter and receiver, compensation circuit, and the power electronic converters – contribute to the total power loss of the system. The transmitter and receiver parts cause ohmic power loss in the windings and in IPT systems, the transmitter and receiver cores give rise to core loss. The compensation circuit elements – capacitors and inductors – also lose energy. Finally, power electronic converters suffer from conduction and switching losses. In addition to the power loss, each component also adds to the mass of the system. The mass of the receiver side components is of particular interest since this leads to an increase in the vehicle mass and hence an increase in the power requirement of the vehicle. On the transmitter side, the mass of the components can be assumed to be a proxy for the cost of the components.

In order to consider the above-mentioned trade-offs between system size (mass) and loss a multi-objective optimization problem is formulated with the geometrical dimensions of the transmitter and receiver and the electrical quantities including transmitter winding current and system operating frequency as the design variables. Constraints are imposed on both the geometrical and electrical design variables to ensure practical operation and safety of the end users. The inverse of the system mass and power loss which includes the sum of the mass and power loss of each component in the system are the selected as the objectives of the multi-objective optimization. This multi-objective optimization is then performed using a genetic algorithm in order to obtain a Pareto-optimal front of designs.

In the following subsection of this chapter previous works in the field of DWPT has been reviewed finally Section 1.2 then presents the organization of the thesis.

1.1 Literature Review

One of the earliest advancements in the field of DWPT was made by the University of California Berkeley, when they undertook the Partners for Advanced Transit and Highways (PATH) program in 1992 [3]. In the PATH program one of the first buses capable of receiving power through a DWPT system. The roadway inductor was typically 3 – 4 ft wide and each of its segments is up to several hundred feet long [3]. Furthermore, the pick-up inductor was also 3 ft

wide and 6 – 15 ft long, depending on the power requirement of the vehicle. The PATH was successfully able to transfer about 60 kW of power to the pick-up inductor through an air gap of 7.6 cm at an efficiency of 60%. However, the buses could not be commercialized due to their size. The large size was due to low operating frequency of 400 Hz caused by the unavailability of fast power electronic switches, lack of high permeability ferrite cores, and conductors such as litz wires.

In [4], the authors employed an E-type ferrite core for DWPT application. The E-shaped transmitter cores embedded within the roadway are segmented into blocks. The primary/transmitter winding was wound around the center leg of the E type transmitter cores. the associated compensation circuit component values were determined using an inverter switching frequency of 20 kHz. The transmitter circuit was designed to deliver a power of 100 kW. The pick-up module in [4] consisted of five ferrite core blocks each rated for 20 kW. Furthermore, each pick-up module was equipped with two rectifier and regulator units to convert the ac power to dc and to boost the rectifier voltage to a level suitable for battery charging [4]. The authors also considered methods to mitigate stray magnetic fields using passive and active shielding. Using the E-type topology the authors in [4] were able to achieve an efficiency of 80% while transferring 100 kW through an air gap of 26 cm.

In [5], the authors developed an I-shaped ferrite core for DWPT application. Unlike the E-type transmitter inductor, the I-type core windings are arranged such that the magnetic poles on adjacent blocks are of opposite polarity. The individual I-shaped core blocks are connected using a ferrite bottom plate to enable low reluctance path for flux flow. The pick-up of the I-type system consists of ferrite plates with pick-up windings wound around it. The length and width of the pick-up was chosen to be 100 cm and 80 cm respectively in order to decrease sensitivity to lateral misalignment. The inverter switching frequency used for this system was 20 kHz and the transmitter winding current was set at 200 A. The I-type system achieved an efficiency of 76% while transferring a power of 27 kW through an air gap of 20 cm.

In [6], an S-shaped transmitter ferrite core has been developed for DWPT application. The system with the S-shaped cores have a pick-up similar to the system with the I-type core. Similar to the I-type cores the power line winding is wound in such a manner that the adjacent S-type core blocks have opposite magnetic polarity. The authors have also compared different winding methods in order to decrease the length of the conductor. The main advantages of the S-type cores over the I-type core is the fact that the S-type cores could be packed into modules thereby reducing

the construction cost and time. Furthermore, the system with S-type cores was found to be more tolerant to lateral displacement compared to the I-type core. The authors were able to transfer a power of 9.5 kW with a system efficiency of about 70% using the S-type core.

While extensive work has been done in developing DWPT systems employing IPT, high power large air gap CPT circuits for DWPT applications are still being researched. In [7], the authors describe a CPT circuit capable of transferring 2.4 kW of power through an air gap of 15 cm. The capacitive transmitter and receiver are made of 610 mm x 610 mm metal plates. Similar to the IPT systems, the CPT circuit has a compensation circuit and high frequency power electronic converters both at the transmitter and receiver side. Operating the inverter at a frequency of 1 MHz, the authors were able to achieve an efficiency of 92% with no misalignment. Some of the challenges faced by high power CPT systems have been explored in this thesis.

1.2 Thesis Outline

This work begins with an analysis of CPT systems. In Chapter 2, a detailed description of a CPT system has been provided and a time domain simulation of the CPT circuit has been conducted. Having explored the shortcomings of the CPT system, the remainder of the thesis concentrates on IPT systems.

Chapter 3 starts with the discussion of two transmitter and receiver geometries for the IPT system. The utilization of finite element analysis (FEA) has been justified and detailed calculations involving the self and mutual inductances of the transmitter and receiver system in order to condense the transmitter – receiver system into a two winding transformer has been shown. Finally, in Chapter 3, the use of 2D FEA over 3D FEA has been justified and one of the geometries has been eliminated.

Chapter 4 discusses the significance of compensation circuits in an IPT system and gives detailed calculations concerning the design of each component of the compensation circuit. The calculations of the mass, volume and power loss occurring within the compensation circuit components have also been shown in Chapter 4.

Chapter 5 is dedicated to the calculations of mass and power loss occurring within the power electronic converters. A detailed metamodel is given in Chapter 5 in order to calculate the mass, conduction and switching losses occurring in the converters. Furthermore, temperature

considerations and a thermal equivalent circuit – based method to calculate the junction temperatures of the switches have also been described.

Chapter 6 gives a brief description of design variables which are to be optimized in order to arrive at a set of non – dominant designs. This set of designs, which form a Pareto front, vary from a high mass/cost high efficiency designs to low mass/cost low efficiency. From this set of designs an informed decision can be on the choice of the design to implemented.

Finally, Chapter 7 discusses the results of the optimization. Therein, salient characteristics of the designs have been discussed and possible reasons behind the exhibition of such characteristics have been stated. Furthermore, a comparison between three designs have provided and the values of the compensation circuit components, power electronic converters and their masses and volumes have been provided.

2. CAPACITIVE DYNAMIC WIRELESS POWER TRANSFER

One of the methods to achieve dynamic wireless power transfer is through capacitive power transfer (CPT). In a CPT circuit, the transmitter and receiver are composed of two metallic plates each and the power is transferred by means of the electric field generated between the plates. Some of the advantages that the CPT has over its inductive counterpart are as follows[7]:

1. Unlike magnetic fields, electric fields are not sensitive to the presence of ferromagnetic materials, like iron, around the transmitter or the receiver. This reduces the leakage flux paths.
2. Magnetic fields cause eddy current losses in ferromagnetic metals which could lead to potential thermal issues.

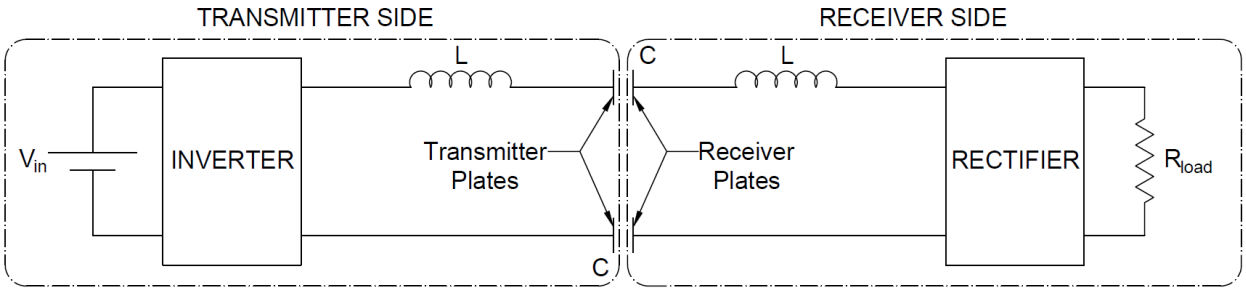

Figure 1. Capacitive charging circuit

A simple CPT circuit is shown in Fig.1. The circuit comprises of three main components:

1. Power electronic converters – high frequency inverter and rectifier
2. The compensation inductor
3. The transmitter/receiver capacitor

The power electronic converters are needed to convert the input voltage from dc to high frequency ac at the source end and then from the high frequency ac to dc at the load end. The transmitter/receiver capacitor values obtained in the wireless power transfer circuits are in the range of nano-farads to picofarads [7] which result in high impedance values even with operating frequencies in the kilohertz to megahertz range. In order to overcome this, compensation inductors are used which have been shown connected in series with the capacitors in Fig. 1. The

compensation inductors are sized such that the equivalent impedance that the circuit presents to the source becomes zero at the fundamental operating frequency of the circuit. The value of the inductance is computed using (1).

$$L = \frac{1}{(\omega^2 C)} \tag{1}$$

where,

ω: ac resonant frequency in rad/s

C: plate capacitance

The capacitance of the transmitter-receiver plates is assumed to be its value at complete alignment given by (2).

$$C = \frac{g}{(\epsilon_0 A)} \tag{2}$$

where,

g: air gap between transmitter and receiver plates

A: Area of the transmitter and receiver plates

ϵ_0: Permittivity of air

The power transferred to the resistive load at the resonant frequency is estimated using (3).

$$P = \frac{V_{in}^2}{(\epsilon_0 A)} \tag{3}$$

2.1 LCLC Capacitive Power Transfer Circuit

The capacitive circuits such as the one shown in Fig.1 suffer from the high voltage across the capacitors and hence results in the need to make the capacitance larger which requires that the air gap between the transmitter and the receiver plates be on the order of millimeters which is impractical for vehicular applications. In order to enable charging across large air gaps the LCLC CPT circuit shown in Fig. 2 has been proposed in [7]. The main parts of the circuit are:

1. The power electronics converters
2. The filter circuit consisting of L_{f1}, C_{f1}, L_{f2} and C_{f2}
3. The compensation inductors - L_1 and L_2
4. The voltage sharing capacitors - C_1 and C_2
5. The transmitter and receiver capacitors - C_{s1} and C_{s2}

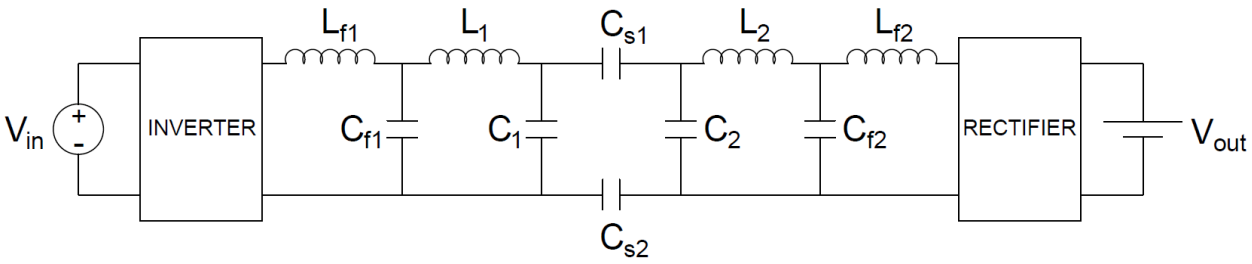

Figure 2. LCLC capacitive power transfer circuit

The power electronics converters, once again, convert the dc voltage to high frequency ac and vice versa. In order to explain the working of the other parts of the circuit a simplified circuit model is considered, wherein the source is considered to be an ac sinusoidal source with the frequency being equal to the fundamental frequency of the square wave input available at the output of the inverter. This circuit is shown in Fig. 3.

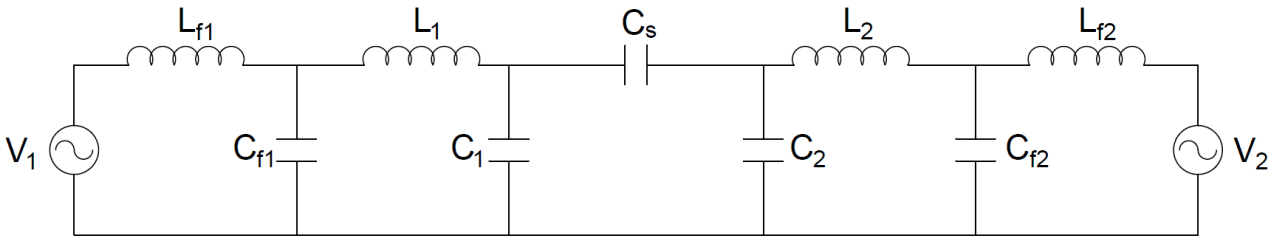

Figure 3. Equivalent LCLC capacitive power transfer circuit

Fig. 3 also shows the circuit with the transmitter/receiver capacitor pair converted to a single equivalent capacitor with the capacitance being equal to the series combination of the capacitors. This simplification is justified since it can be verified by using Kirchhoff's voltage law

that the current that flows in both the capacitors are the same and so are the voltages which can be added. Furthermore, it is easier to derive the state model of the circuit shown in Fig. 3 compared to the original circuit.

In order to explain the circuit and derive the formula for the inductances - L_{f1}, L_1, L_2 and L_{f2} - the circuit will be broken up into two parts – the filter components with the sinusoidal voltage source and the middle part of the circuit consisting of the compensation inductor and the capacitors. Superposition along with phasor analysis is used to analyze the circuit.

Consider the circuit shown in Fig. 4. This circuit shows the filter components and the voltage source with a load impedance connected in parallel with the capacitor.

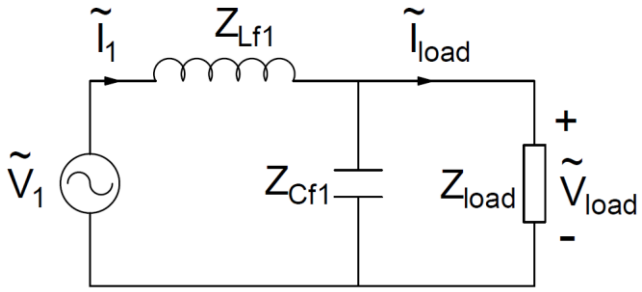

Figure 4. Equivalent filter circuit

The load voltage and current are given by:

$$\tilde{V}_{Load} = \left(\frac{Z_{CLoad}}{Z_{CLoad} + Z_{Lf1}}\right)\tilde{V}_1 \tag{4}$$

$$\tilde{I}_{Load} = \left(\frac{Z_{Cf1}}{Z_{Cf1} + Z_{Load}}\right)\tilde{I}_1 \tag{5}$$

where,

$$Z_{Cf1} = \frac{1}{(j\omega C_{f1})} \tag{6}$$

$$Z_{CLoad} = \frac{Z_{Cf1} Z_{Load}}{Z_{Cf1} + Z_{Load}} \tag{7}$$

$$Z_{Lf1} = j\omega L_{f1} \tag{8}$$

and

$$\tilde{I}_1 = \frac{\tilde{V}_1}{Z_{CLoad} + Z_{Lf1}} \tag{9}$$

Substituting the value of $\tilde{I}_1$ in (5) and (4) the load current and voltage can be calculated as:

$$\tilde{I}_{Load} = \frac{Z_{Cf1} \tilde{V}_1}{Z_{Lf1} Z_{Cf1} + Z_{Load}(Z_{Lf1} + Z_{Cf1})} \tag{10}$$

$$\tilde{V}_{Load} = \frac{Z_{Cf1} Z_{Load}}{Z_{Lf1} Z_{Cf1} + Z_{Load}(Z_{Lf1} + Z_{Cf1})} \cdot \tilde{V}_1 \tag{11}$$

At resonance the component impedances are related as follows:

$$Z_{Lf1} + Z_{Cf1} = 0 \Rightarrow L_{f1} = \frac{1}{\omega^2 \cdot C_{f1}} \tag{12}$$

The equations of the load current and the load voltage at resonance are then given by:

$$\tilde{I}_{load} = \frac{\tilde{V}_1}{Z_{Lf1}} \tag{13}$$

$$\tilde{V}_{Load} = \frac{Z_{Load}}{Z_{Lf1}} \tilde{V}_1 \tag{14}$$

It can be seen from (13) that the load current does not depend upon the load impedance at resonance. Hence it can be said that this part of the circuit behaves like a current source with the value of the current given by (13). Fig. 5 shows the circuit in Fig. 3 with the initial part of the circuit replaced with a current source.

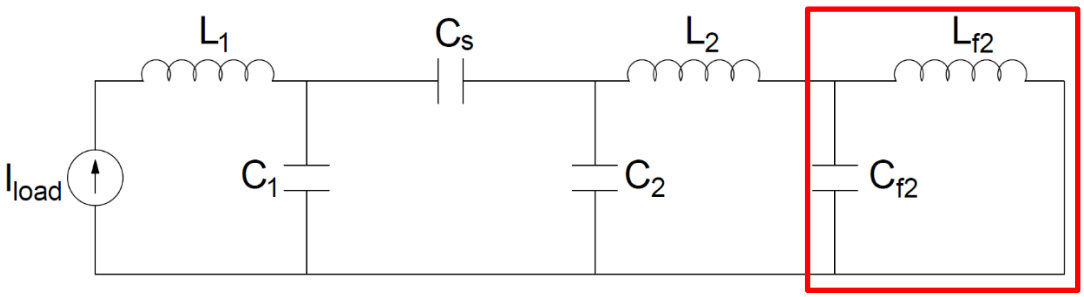

Figure 5. Equivalent circuit with filter circuit replaced by current source

With this part of the circuit we intend to calculate the load impedance which appears across the current source.

$$L_{f2} = \frac{1}{\omega^2 C_{f2}} \tag{15}$$

Choosing the values of L_{f2} and C_{f2} such that at resonance they are related by (15) we see that the part of the circuit indicated within the red box presents an infinite impedance to the current source and hence no current flows through L_2. The impedance presented to the current source by the rest of the circuit is given by:

$$Z_{Load} = Z_{L1} + Z_{Cp1} \tag{16}$$

where,

$$Z_{L1} = j\omega L_1 \tag{17}$$

$$Z_{Cp1} = \frac{1}{(j\omega C_{p1})} \tag{18}$$

$$C_{p1} = C_1 + \frac{C_s C_2}{C_s + C_2} \tag{19}$$

$$L_1 = \frac{1}{\omega^2 C_{p1}} + L_{f1} \tag{20}$$

If the value of the inductance of L_1 given by (20) is substituted in (17), then the impedance presented by this part of the circuit to the current source is given by (21).

$$Z_{Load} = Z_{Lf1} \tag{21}$$

Substituting this value of load impedance back into (14) gives us:

$$\tilde{V}_{Load} = \tilde{V}_1 \tag{22}$$

Furthermore, the substitution of the load impedance value in (9) yields and using the relation between impedances during resonance given by (12) we get:

$$\tilde{I}_1 = \frac{\tilde{V}_1}{Z_{CLoad} + Z_{Lf1}} = 0 \tag{23}$$

Equation (23) implies that the source current does not depend on the source voltage but depends only on the load/battery voltage. A similar analysis can be conducted by considering only the load/battery voltage since the circuit is symmetric. Therefore, using receiver side voltage as the source and performing a similar analysis one can conclude that the current flowing into the battery depends only on the input voltage and not the battery voltage. Next, the phase relationship between the input and output variables are derived. It had been proved earlier that the input current does not depend on the input voltage. Using the circuit shown in Fig. 5, the voltage across capacitor C_2 can be calculated as follows:

$$\tilde{V}_{C2} = \tilde{I}_{load} \frac{Z_{C1}}{Z_{C1} + Z_{Cs} + Z_{C2}} Z_{C2} \tag{24}$$

where,

$$Z_{C1} = \frac{1}{j\omega C_1} \tag{25}$$

$$Z_{C2} = \frac{1}{j\omega C_2} \tag{26}$$

$$Z_{Cs} = \frac{1}{j\omega C_s} \tag{27}$$

and,

$$\tilde{I}_{load} = -\frac{\tilde{V}_1}{Z_{Cf1}} \tag{28}$$

Since at resonance no current flows through the inductor L_2, we can say that the voltage across capacitor C_{f2} is the same as that across capacitor C_2. Therefore, the output current flowing through the inductor L_{f2} is given by:

$$\tilde{I}_2 = \frac{\tilde{V}_{C2}}{Z_{Lf2}} \tag{29}$$

In (29)

$$Z_{Lf2} = j\omega L_2 \tag{30}$$

At resonance:

$$Z_{Lf2} = -Z_{Cf2} = -\frac{1}{j\omega C_{f2}} \tag{31}$$

Therefore,

$$\tilde{I}_2 = -\frac{\tilde{V}_{C2}}{Z_{Cf2}} = -j\tilde{V}_{C2}(\omega C_{f2}) \tag{32}$$

Substituting the expressions for the impedances into (13) and (24), one obtains the value of the output current as follows:

$$\tilde{I}_2 = j\tilde{V}_1\left(\frac{\omega C_s C_{f1} C_{f2}}{C_1C_2 + C_2C_s + C_1C_s}\right) \tag{33}$$

From (33) one can observe that the output current leads the input voltage by 90 degrees. Since the output voltage is rectified by using an H-bridge, the output voltage also leads the input voltage by 90 degrees[7]. Using a similar analysis, the input current can be computed resulting in:

$$\tilde{I}_1 = -1i \cdot \tilde{V}_2 \cdot \left(\frac{\omega C_s C_{f1} C_{f2}}{C_1C_2 + C_2C_s + C_1C_s}\right) \tag{34}$$

From (34) it can be seen that the input current lags the output voltage by 90 degrees and hence is in phase with the input voltage. Using (33) and (34) and the fact that the input voltage and current are in phase with each other, the average value of the input power can be calculated using (35).

$$P_{in} = \tilde{V}_1 \cdot \tilde{I}_1 = \tilde{V}_1\tilde{V}_2\left(\frac{\omega C_s C_{f1} C_{f2}}{C_1C_2 + C_2C_s + C_1C_s}\right) \tag{35}$$

Similarly, the output power can be calculated using:

$$P_{out} = \tilde{V}_2 \cdot \tilde{I}_2 = \tilde{V}_1 \tilde{V}_2 \left(\frac{\omega C_s C_{f1} C_{f2}}{C_1 C_2 + C_2 C_s + C_1 C_s} \right) \quad (36)$$

Note that in the absence of any resistances, the output power equals the input power. However, in reality this will not be the case due to the power loss occurring in the capacitors and inductors and also due to the leakage of electric flux between the transmitter and receiver plates.

2.2 Simulation and case for inductive power transfer

The LCLC capacitive power transfer circuit shown in Fig. 2 is simulated in SIMULINK. Equations (37) - (44) describe the state model which has been used to model the circuit. The circuit has been simulated for a transfer a power of 2.4 kW across an air gap of 15 cm. The circuit parameter and component values used for simulation have been listed in Table 1 and the definitions of the variables used in (37) - (44) have been provided in Tables 2 and 3. The values used for capacitors C_{s1}, C_{s2}, C_1, C_2, C_{f1} and C_{f2} has been obtained from [7] and the inductance values can be calculated using the equations derived in the previous section.

$$\frac{di_{Lf1}}{dt} = \frac{v_1 - v_{Cf1}}{L_{f1}} \quad (37)$$

$$\frac{dv_{Cf1}}{dt} = \frac{i_{Lf1} - i_{L1}}{C_{f1}} \quad (38)$$

$$\frac{di_{L1}}{dt} = \frac{v_{Cf1} - v_{C1}}{L_1} \quad (39)$$

$$\frac{dv_{C1}}{dt} = \frac{(C_2 + C_s) i_{L1} - C_s i_{L2}}{C_1 C_2 + C_s (C_1 + C_2)} \quad (40)$$

$$\frac{dv_{C2}}{dt} = \frac{C_s i_{L1} - (C_2 + C_s) i_{L2}}{C_1 C_2 + C_s (C_1 + C_2)} \quad (41)$$

$$\frac{di_{L2}}{dt} = \frac{v_{C2} - v_{Cf2}}{L_2} \tag{42}$$

$$\frac{dv_{Cf2}}{dt} = \frac{i_{L2} - i_{Lf2}}{C_{f2}} \tag{43}$$

$$\frac{di_{Lf2}}{dt} = \frac{v_{cf2} - v_2}{L_{f2}} \tag{44}$$

Table 1. Circuit Component Values

Component/Parameter	Value
L_{f1}	11.6 μH
C_{f1}	2.18 nF
L_1	231 μH
C_1	100 pF
C_{s1}	36.7 pF
C_{s2}	36.7 pF
C_2	100 pF
L_2	242 μH
C_{f2}	2.18 nF
L_{f2}	11.6 μH
$\|v_1\|$	265 V
$\|v_2\|$	280 V

Table 2. State Variables Description

State Variables	Variable Description
i_{Lf1}	Current through inductor L_{f1}
v_{Cf1}	Voltage across capacitor C_{f1}
i_{L1}	Current through inductor L_1
v_{C1}	Voltage across capacitor C_1
v_{C2}	Voltage across capacitor C_2
i_{L2}	Current through inductor L_2
v_{Cf2}	Voltage across capacitor C_{f2}
i_{Lf2}	Current through inductor L_{f2}

Table 3. Input Variables Description

Input Variables	Variable Description
v_1	Transmitter side inverter output voltage
v_2	Receiver side rectifier input voltage

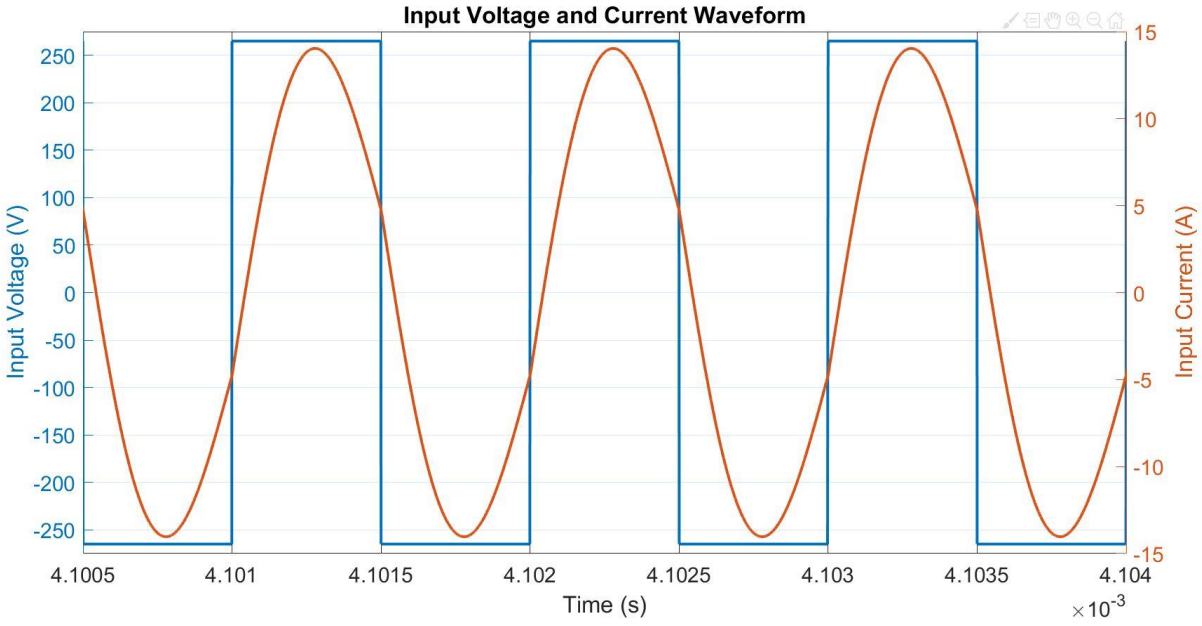

Figure 6. Input voltage and current waveform

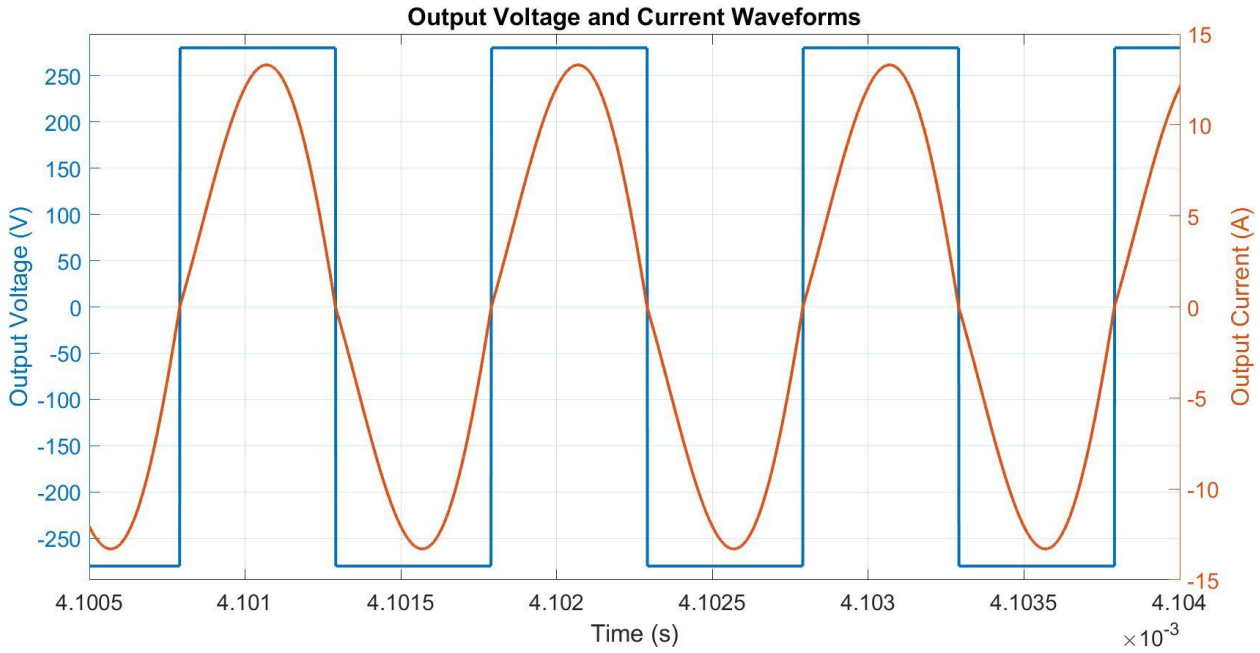

Figure 7. Output voltage and current waveform

Figs. 6 and 7 show the input and output voltage and current waveforms of the circuit. The frequency used for the simulation is 1 MHz. It can be seen from Fig. 6 that the input voltage is a square wave and the input current has an almost sinusoidal form. Another observation is that the input voltage and current are in phase. The output voltage and current waveforms exhibit similar waveform characteristics as the input waveforms. The 90^{o} phase shift between the input and output waveforms, derived in (33) and (34) can also be observed when we compare Figs. 6 and 7.

Dynamic wireless charging requires the CPT circuit to be capable of transferring hundreds of kilowatts of power through the air gap. In order to understand the circuit's response at such high power levels, the circuit is simulated with the input voltage level changed to 11kV such that the circuit is capable of transferring a power of 280 kW.

Figs. 8 and 9 show the voltages occurring across the air gap and across the capacitor C_2 inside the vehicle. The voltages across the air gap and within the vehicle have amplitudes greater than 400 kV and 100 kV respectively, making it potentially unsafe for the pedestrians and drivers.

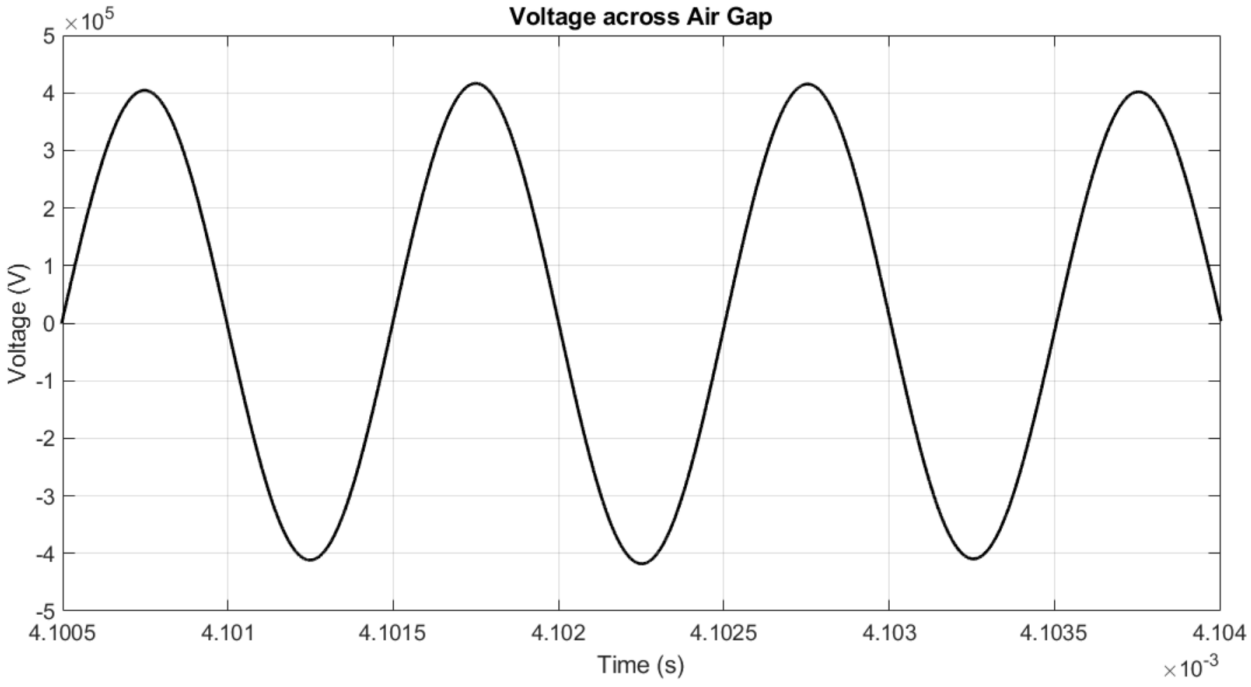

Figure 8. Voltage across air gap

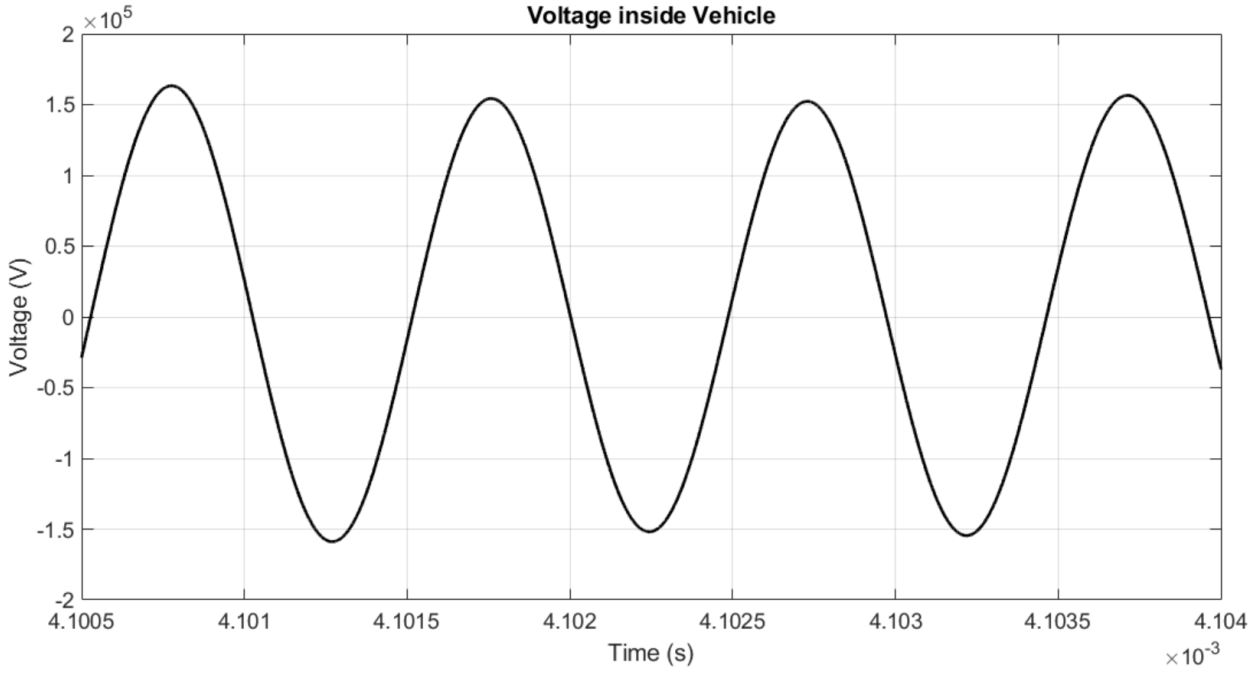

Figure 9. Voltage inside vehicle

To consider further one can use the voltage and current relation of a capacitor to derive a simple formula for the voltage across of the capacitor in terms of the capacitance, the switching angular frequency and the power level.

$$V_C = \sqrt{\frac{P_C}{(2\pi \cdot freq \cdot C)}} \tag{45}$$

It can be seen that for a given power level, the only way we can achieve lower voltage levels is to increase the capacitance or to increase the switching frequency. The only way to increase the capacitance is by increasing the area of the plates. Since the dimensions of the receiver plates are limited by the dimensions of a vehicle, this parameter cannot be increased drastically to reduce the voltage. The only other option available is to increase the switching frequency. This means that one needs to operate at switching frequencies in the range of several tens of MHz while conducting high currents. The lack of existing availability of such high frequency power electronic switches limits this option for the foreseeable future.

To summarize, the unsafe voltage levels appearing across the air gap and within vehicle and limitations to mitigate this high voltage renders the implementation of CPT method impractical given modern technology limits. Although this is a technology which could be implemented with further advances in the power electronic switches, it is more prudent to an alternative – inductive power transfer – for dynamic wireless power transfer.

3. TRANSMITTER AND RECEIVER

3.1 E – Type transmitter and receiver System

The E-type transmitter-receiver system, as the name suggests, consists of 'E' shaped transmitter and receiver cores. The transmitter is embedded within a pre-fabricated concrete slab while the receiver is placed within the EV. The following section gives a description of the E – type transmitter and receiver and the flux diagram obtained using an E – type transmitter-receiver system.

3.1.1 Transmitter Description

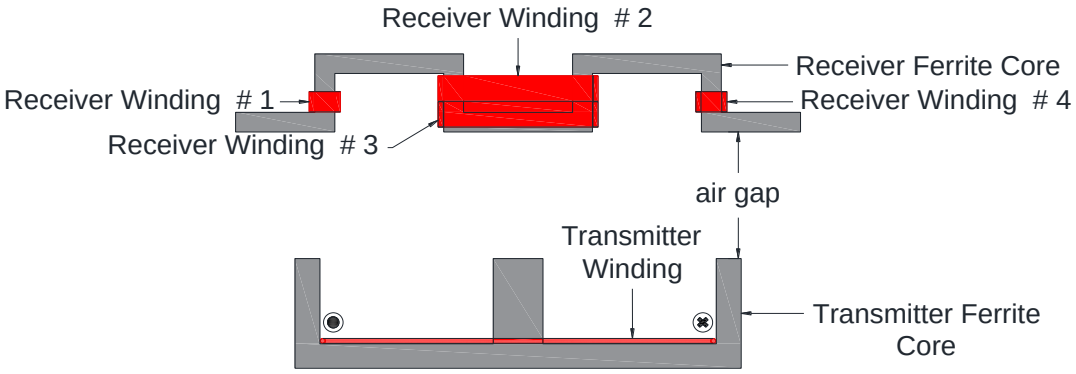

Figure 10. E – type transmitter and receiver

The E-type transmitter and receiver core and the transmitter and receiver windings along with the current direction is shown in Fig. 10. The E-type transmitter is embedded within the roadway and is made up of 15ft x 12 ft concrete slabs with multiple 'E' shaped ferrite cores embedded within each one of them as shown in Fig. 11. The ferrite core is divided into multiple units due to the brittle nature of ferrite. Dividing the cores into multiple units help the cores to withstand the pressure of the vehicles on the road and also helps in integration with the concrete slab as the concrete is allowed to flow in between individual units.

The transmitter winding consists of litz wire which is wound around the center leg or around the side legs. The choice of litz wire is attributed to its ability to uniformly distribute the current within the wire under high frequency operation.

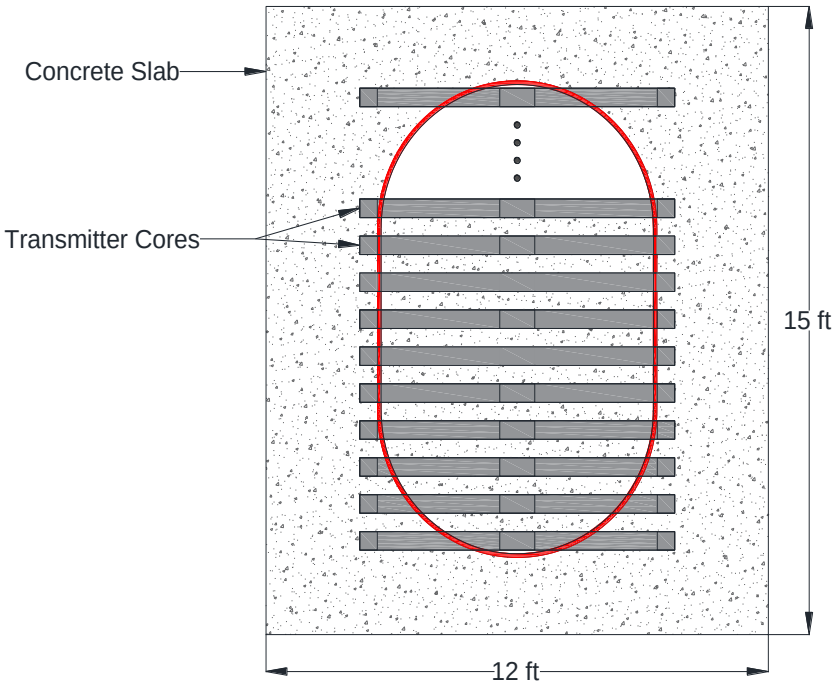

Figure 11. E - Type transmitter core layout

3.1.2 Receiver Description

The receiver for the E-type system consists of an almost E shaped ferrite core with windings. Unlike the transmitter, the receiver core is a uniform ferrite core since it will not be subjected to high pressure conditions like the transmitter.

The receiver winding consists of litz wire turns wrapped around the vertical limbs of the core. The receiver winding is composed of four coils of litz wire. The center two limbs house two coils, each with 5 turns and the end limbs house one coil, each with 4 turns. Each of these coils could be connected in various series and parallel combinations. In this study all the coils are connected in series to mitigate losses caused by circulating currents which would be encountered in the case of parallel connected coils.

3.1.3 Flux Path

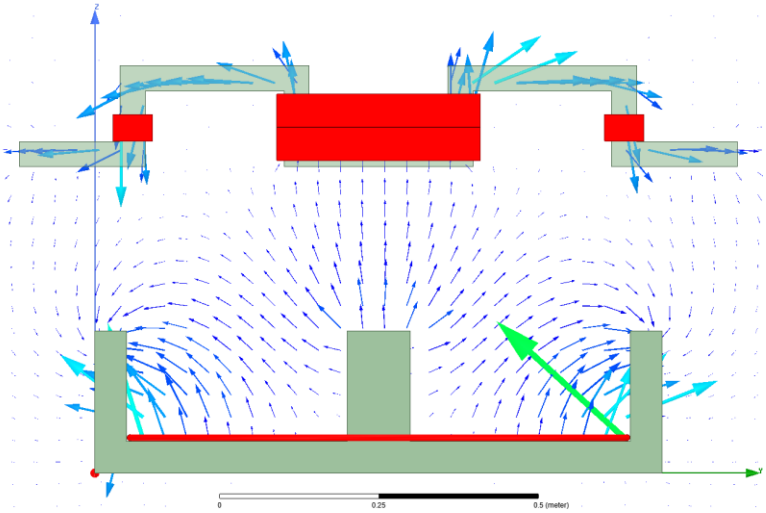

Figure 12. E - Type system flux diagram

For the direction of current shown in the Fig.10, we can see from Fig.12 that the flux emanates from the middle leg of the transmitter, links the receiver windings and returns back through the side legs. For the opposite direction of current the flux emanates from the side legs and returns through the middle leg. It is evident from the flux paths that in either case (different current directions), the flux through the middle leg is larger than the flux which flows through the side legs. Therefore, it can be said that the width of the middle leg should be at least twice the width of the side legs to limit the effects of saturation of the core.

3.2 Double – D Type transmitter and receiver system

The Double-D type transmitter-receiver system was first introduced in [8]. The Double-D type architecture is a loosely coupled transmitter – receiver system aimed at charging EVs with a power transfer capability of 2kW over an air gap of 200mm at an operating frequency of 20kHz. Fig. 13 shows the Double-D type transmitter introduced in [8].

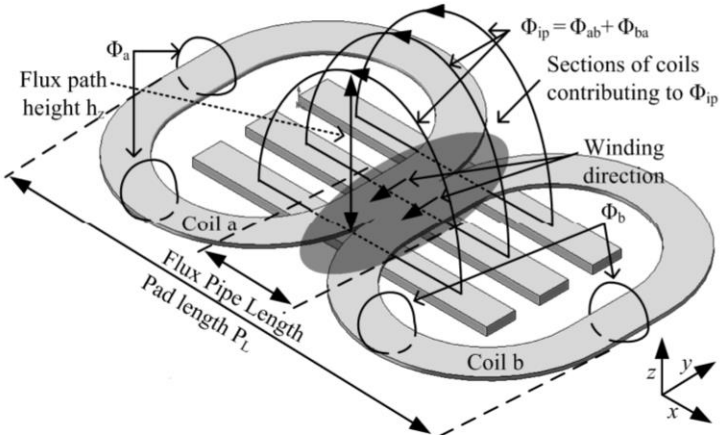

Figure 13. Double - D transmitter [8]

3.2.1 Original DD Transmitter

The original DD Transmitter had a core made up of individual ferrite bars separated at a fixed distance. The transmitter winding consists of two co-planar coils placed on top of the ferrite bars. The part in the center constitutes what the authors in [8] describe as a flux pipe because the coils are magnetically in series and electrically connected in parallel. Furthermore, an aluminum shielding is also placed between the coils and the ferrite bars. It is suggested in [8] that in order to increase the mutual flux, the flux pipe portion of the transmitter must be made as long as possible. Doing so results in two coils shaped like a 'D' placed back to back and hence the name 'DD'. The following advantages were observed as a result of utilizing the DD transmitter:

1. Single sided flux paths
2. Average flux path height proportional to half the length of the transmitter
3. Insensitivity to aluminum shielding
4. Low leakage flux out of the back

3.2.2 Magment Double – D Transmitter

Fig. 14 shows the DD transmitter developed by Magment. The DD transmitter developed by Magment differs from the original DD transmitter developed by the authors of [8] in both structure and material. Magment's DD transmitter's core, unlike the original DD transmitter, does not consist of ferrite bars separated by a fixed distance from each other. Magment's transmitter core is instead composed of magnetizable concrete – MC40 which can be poured to make a rigid

continuous/unsegmented structure capable of enduring the high pressure imposed by heavy vehicles travelling on the roadway.

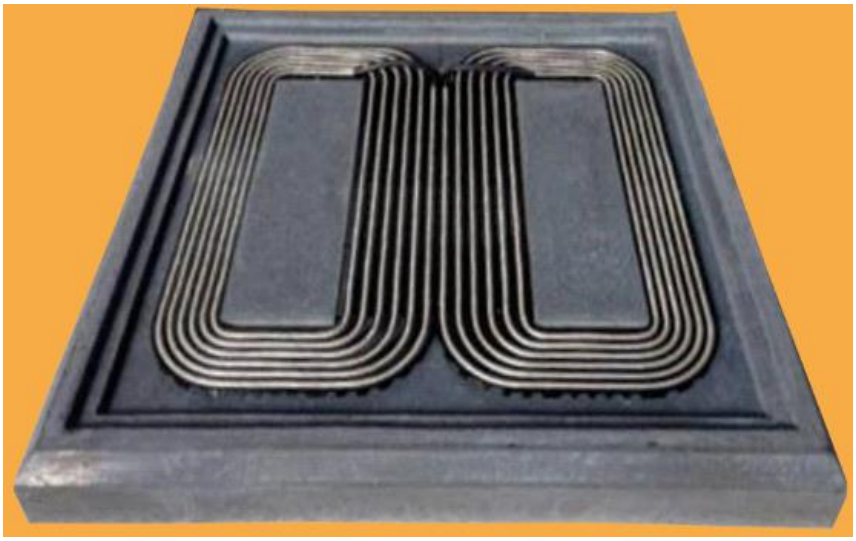

Figure 14. Magment Double – D transmitter [9]

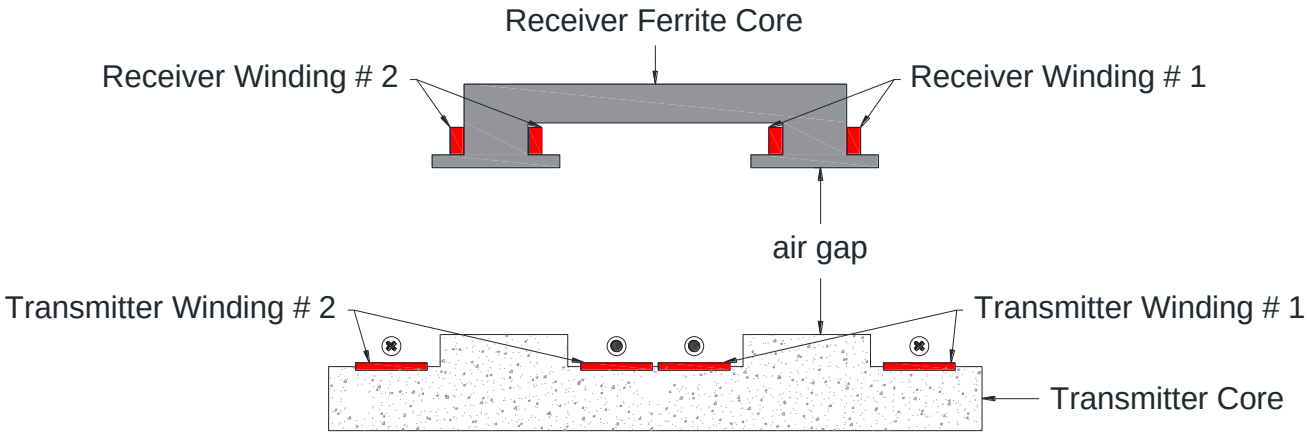

Figure 15. Double – D transmitter and receiver system

The continuous structure of the transmitter core also aids in model simplicity, specifically, the finite element analysis (FEA) of this system only requires a 2D analysis. Another difference is the presence of stubs on the transmitter, which is not present on the original DD transmitter. The presence of the stubs makes it possible for the magnetic flux to complete its path more effectively

by reducing the effective reluctance of the magnetic flux path. This would mean that the taller the stub the lower the reluctance of the mutual flux path. But the height of the stub is constrained by the height of the concrete slab within which the transmitter is embedded and also by stress which will be placed on the transmitter by the vehicles above. As seen in Fig. 15, the transmitter winding is wound around each stub in such a manner as to produce magnetic poles of opposite polarity on each stub. The conductors are chosen to be litz wires suitable for high frequency operation. The magnetic properties of the core material – magnetizable concrete – developed by Magment are provided in Table 4 [10].

Table 4. MC40 properties

Property	**Measurement Conditions**	**Values**
Initial permeability	25˚C	40 ± 10%
Flux density @ H = 25 kA/m	25˚ C	450 mT
Coercive field strength	100˚ C	390 mT
Curie – temperature		Greater than 210˚ C
Resistivity (DC)		20 Ω m
Density		3750 kg/m^3
Relative loss factor	1 MHz	Less than 0.5 x 10^{-3}
Relative temperature coefficient	-40˚ C … 150˚ C	Less than 50 x 10^{-6}/K
Hysteresis material constant	10 kHz	Less than 3 x 10^{-6}/K
DC – Bias (percent permeability change)	@ 4 kA/m	55%
	@ 8 kA/m	33%
Relative core losses	@ 50 kHz, 100mT	300 kW/m^3
Specific heat		700 J/(kg K)
Thermal conductivity		3 W/mK
Young's modulus		25000 MPa
Compressive strength		Greater than 50 MPa
Tensile strength		2 MPa
Linear expansion coefficient		12 x 10^{-6}/K

3.2.3 Double – D Receiver

Fig. 15 shows the receiver for the DD type system. The receiver consists of a U-shaped core made out of Magment's magnetizable concrete. This shape of the core aids in reducing the reluctance of the mutual flux's path. The receiver windings are made of litz wire wound around each leg/tooth of the receiver. The position of the receiver windings may be changed, for example – the winding could be wound around the base of the receiver core. However, since the system is

a loosely coupled system, the leakage flux constitutes the majority of the flux and we require that mutual flux links the receiver windings as much as possible. This is achieved by placing the receive windings on the two legs of the core. Another modification that has been made to a generic U-core is the addition of the tooth tips to the teeth of the receiver. This once again makes it possible for the receiver to link as much mutual flux as possible.

3.2.4 Flux path

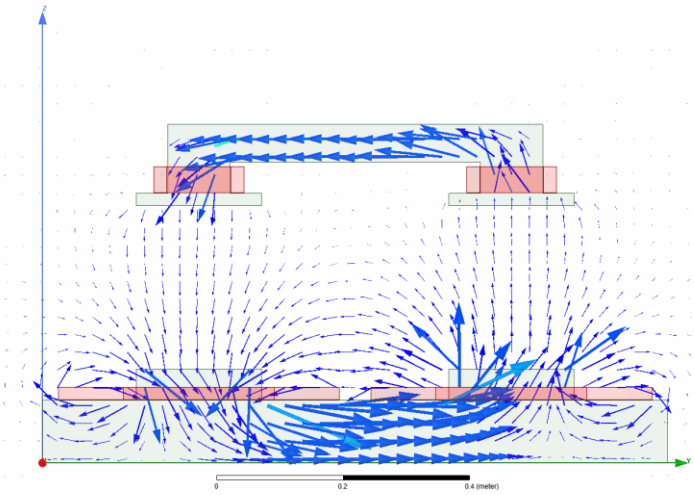

Figure 16. Flux diagram for Double-D type system

The flux path for the given Double-D transmitter receiver system is shown in Fig. 26. It can be seen that for the current direction given in Fig. 15 flux emanates from the right stub into the air gap, links the receiver windings on both legs and returns through the left stub. Since the entire flux(mutual) originates on one stub and returns through the other, the area of the stub faces has been made the same. Also, it can be seen once again that most of the flux is leakage flux.

3.3 Finite Element Analysis

Both the E-type and Double-D type systems are loosely coupled systems owing to the large air gap present between the receiver and transmitter systems. The presence of the air gap makes it nearly impossible to employ magnetic equivalent circuit-based methods to calculate the circuit quantities like the inductances of the windings. Therefore, finite element analysis (FEA) is used to

calculate the inductances and the core loss associated with the system. To this end, the Ansys Maxwell tool made available by Ansys Electronics Desktop is used for the FEA.

3.3.1 Equivalent Inductance Calculation

For circuit analysis of the DWPT system, the multiple winding transmitter and receiver must be reduced to an equivalent two winding transformer. To accomplish this, consider the four winding-transformer shown in Fig. 17 is considered.

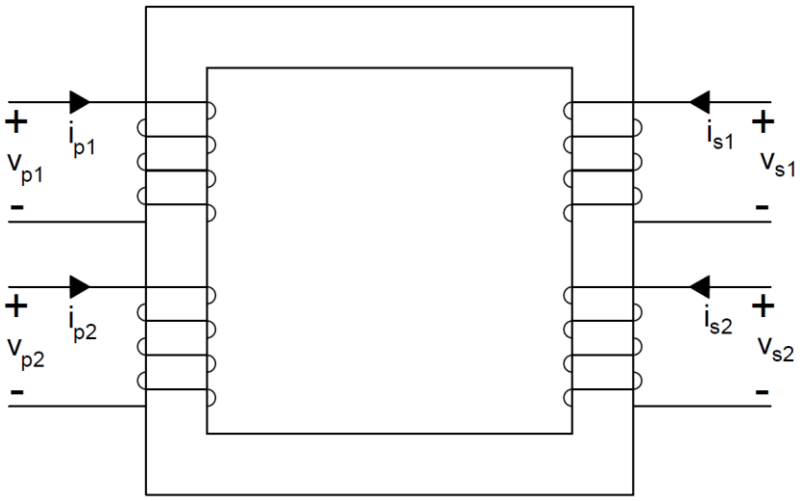

Figure 17. Four winding transformer

Fig. 17 is a close representation of the Double-D system and can also be used for the E-type system by changing the number of coils in the primary and secondary sides. In Fig. 17, the windings p1 and p2 constitute the primary/transmitter windings and s1 and s2 constitute the secondary/receiver windings.

The flux linkages of each coil can be written as:

$$\lambda_{p1} = L_{p1p1}i_{p1} + L_{p1p2}i_{p2} + L_{p1s1}i_{s1} + L_{p1s2}i_{s2} \quad (46)$$

$$\lambda_{p2} = L_{p2p1}i_{p1} + L_{p2p2}i_{p2} + L_{p2s1}i_{s1} + L_{p2s2}i_{s2} \quad (47)$$

$$\lambda_{s1} = L_{s1p1}i_{p1} + L_{s1p2}i_{p2} + L_{s1s1}i_{s1} + L_{s1s2}i_{s2} \quad (48)$$

$$\lambda_{s2} = L_{s2p1} i_{p1} + L_{s2p2} i_{p2} + L_{s2s1} i_{s1} + L_{s2s2} i_{s2} \tag{49}$$

where,

$$L_{xy} = \frac{N_x N_y}{R_m} \tag{50}$$

$$x \in \{p1, p2, s1, s2\}$$

$$y \in \{p1, p2, s1, s2\}$$

The description of the variables used in (46) – (50) have been given in Table 5.

Table 5. Variable Description for (46) - (50)

Variable	Description
λ_{p1}	Flux linkage of winding p1
λ_{p2}	Flux linkage of winding p2
λ_{s1}	Flux linkage of winding s1
λ_{s2}	Flux linkage of winding s2
L_{p1p1}	Self-inductance of winding p1
L_{p1p2}	Mutual inductance of winding p1 and p2
L_{p1s1}	Mutual inductance of winding p1 and s1
L_{p1s2}	Mutual inductance of winding p1 and s2
L_{p2p2}	Self-inductance of winding p2
L_{p2s1}	Mutual inductance of winding p2 and s1
L_{p2s2}	Mutual inductance of winding p2 and s2
L_{s1s1}	Self-inductance of winding s1
L_{s1s2}	Mutual inductance of winding s1 and s2
L_{s2s2}	Self-inductance of winding s2
N_x	Number of turns in winding ‘x’

Assuming the ohmic resistances of the coils to be negligible, the voltage equations of each winding can be written as:

$$v_{p1} = \frac{d\lambda_{p1}}{dt} = L_{p1p1}\frac{di_{p1}}{dt} + L_{p1p2}\frac{di_{p2}}{dt} + L_{p1s1}\frac{di_{s1}}{dt} + L_{p1s2}\frac{di_{s2}}{dt} \tag{51}$$

$$v_{p2} = \frac{d\lambda_{p2}}{dt} = L_{p2p1}\frac{di_{p1}}{dt} + L_{p2p2}\frac{di_{p2}}{dt} + L_{p2s1}\frac{di_{s1}}{dt} + L_{p2s2}\frac{di_{s2}}{dt} \tag{52}$$

$$v_{s1} = \frac{d\lambda_{s1}}{dt} = L_{s1p1}\frac{di_{p1}}{dt} + L_{s1p2}\frac{di_{p2}}{dt} + L_{s1s1}\frac{di_{s1}}{dt} + L_{s1s2}\frac{di_{s2}}{dt} \tag{53}$$

$$v_{s2} = \frac{d\lambda_{s2}}{dt} = L_{s2p1}\frac{di_{p1}}{dt} + L_{s2p2}\frac{di_{p2}}{dt} + L_{s2s1}\frac{di_{s1}}{dt} + L_{s2s2}\frac{di_{s2}}{dt} \quad (54)$$

The power transferred by each coil can be expressed as:

$$P_{p1} = v_{p1}i_{p1} = i_{p1}(L_{p1p1}\frac{di_{p1}}{dt} + L_{p1p2}\frac{di_{p2}}{dt} + L_{p1s1}\frac{di_{s1}}{dt} + L_{p1s2}\frac{di_{s2}}{dt}) \quad (55)$$

$$P_{p2} = v_{p2}i_{p2} = i_{p2}(L_{p2p1}\frac{di_{p1}}{dt} + L_{p2p2}\frac{di_{p2}}{dt} + L_{p2s1}\frac{di_{s1}}{dt} + L_{p2s2}\frac{di_{s2}}{dt}) \quad (56)$$

$$P_{s1} = v_{s1}i_{s1} = i_{s1}(L_{s1p1}\frac{di_{p1}}{dt} + L_{s1p2}\frac{di_{p2}}{dt} + L_{s1s1}\frac{di_{s1}}{dt} + L_{s1s2}\frac{di_{s2}}{dt}) \quad (57)$$

$$P_{s2} = v_{s2}i_{s2} = i_{s2}(L_{s2p1}\frac{di_{p1}}{dt} + L_{s2p2}\frac{di_{p2}}{dt} + L_{s2s1}\frac{di_{s1}}{dt} + L_{s2s2}\frac{di_{s2}}{dt}) \quad (58)$$

In order to derive the equivalent inductance of the transmitter and the receiver windings consider the two winding transformer shown in Fig. 18.

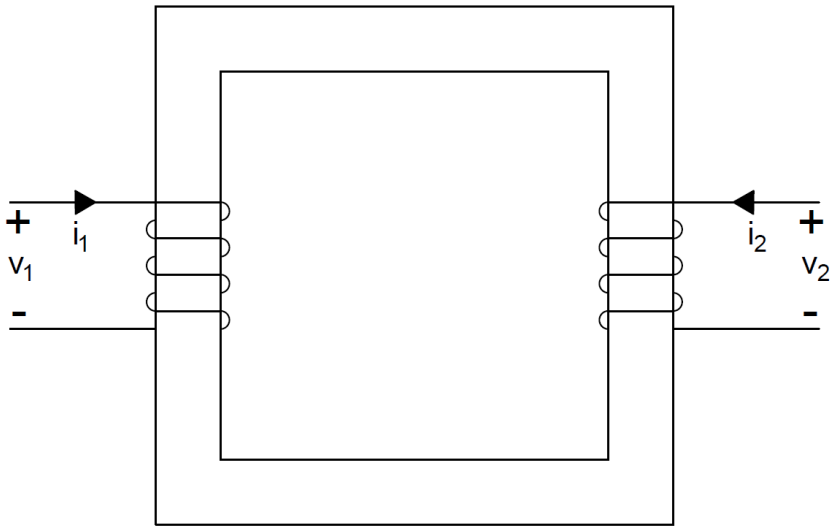

Figure 18. Equivalent two winding transformer

The voltage equations for the windings can be written as:

$$v_1 = L_{11}\frac{di_1}{dt} + M\frac{di_2}{dt} \tag{59}$$

$$v_2 = M\frac{di_1}{dt} + L_{22}\frac{di_2}{dt} \tag{60}$$

Using power balance, the power transferred by the equivalent primary winding in Fig. 18 should be equal to the power transferred by the primary windings in Fig. 17. Similarly, the power transferred by the equivalent secondary winding in Fig. 18 must equal the power transferred by the secondary windings in Fig. 17.

$$v_1 i_1 = v_{p1} i_{p1} + v_{p2} i_{p2} \tag{61}$$

Expanding (61) using (59), (51) and (52)

$$\begin{aligned} L_{11} i_1 \frac{di_1}{dt} + Mi_1\frac{di_2}{dt} = {} & L_{p1p1} i_{p1}\frac{di_{p1}}{dt} + L_{p1p2} i_{p1}\frac{di_{p2}}{dt} \\ & + L_{p1s1} i_{p1}\frac{di_{s1}}{dt} + L_{p1s2} i_{p1}\frac{di_{s2}}{dt} + L_{p2p1} i_{p2}\frac{di_{p1}}{dt} + \\ & + L_{p2p2} i_{p2}\frac{di_{p2}}{dt} + L_{p2s1} i_{p2}\frac{di_{s1}}{dt} + L_{p2s2} i_{p2}\frac{di_{s2}}{dt} \end{aligned} \tag{62}$$

Rewriting (62):

$$\begin{aligned} \frac{L_{11}}{2}\frac{di_1^2}{dt} + Mi_1\frac{di_2}{dt} = {} & \frac{1}{2}\left(L_{p1p1} + 2L_{p1p2} + L_{p2p2}\right)\frac{d\left(i_{p1} + i_{p2}\right)^2}{dt} + \\ & L_{p1s1} i_{p1}\frac{di_{s1}}{dt} + L_{p1s2} i_{p1}\frac{di_{s2}}{dt} + L_{p2s1} i_{p2}\frac{di_{s1}}{dt} + L_{p2s2} i_{p2}\frac{di_{s2}}{dt} \end{aligned} \tag{63}$$

Comparing the quantities containing the derivative of the primary currents only, one can write:

$$L_{11} = \left(L_{p1p1} + 2L_{p1p2} + L_{p2p2}\right) \tag{64}$$

Similarly, expressing the power balance equation for the secondary side can be written as:

$$\begin{aligned} \frac{L_{22}}{2}\frac{di_2^2}{dt} + Mi_2\frac{di_1}{dt} = {} & \frac{1}{2}(L_{s1s1} + 2L_{s1s2} + L_{s2s2})\frac{d(i_{s1} + i_{s2})^2}{dt} + \\ & L_{p1s1} i_{s1}\frac{di_{p1}}{dt} + L_{p1s2} i_{s2}\frac{di_{p1}}{dt} + L_{p2s1} i_{s1}\frac{di_{p2}}{dt} + L_{p2s2} i_{s2}\frac{di_{p2}}{dt} \end{aligned} \tag{65}$$

Comparing the quantities containing the derivative of the secondary currents only one can write:

$$L_{22} = (L_{s1s1} + 2L_{s1s2} + L_{s2s2}) \tag{66}$$

Thus, to calculate the equivalent mutual inductance (63) and (65) are added and the mutual inductance terms are compared:

$$M\frac{d(i_1 i_2)}{dt} = L_{p1s1}\frac{d(i_{p1}i_{s1})}{dt} + L_{p1s2}\frac{d(i_{p1}i_{s2})}{dt} + L_{p2s1}\frac{d(i_{p2}i_{s1})}{dt} + L_{p2s2}\frac{d(i_{p2}i_{s2})}{dt} \tag{68}$$

Connecting the primary windings of Fig. 17 in series and secondary windings of Fig. 17 in series:

$$i_1 = i_{p1} = i_{p2} \tag{69}$$

$$i_2 = i_{s1} = i_{s2} \tag{70}$$

Substituting the relations in (23) and (24) into (22) one can write:

$$M = L_{p1s1} + L_{p1s2} + L_{p2s1} + L_{p2s2} \tag{71}$$

The equivalent inductances derived in (64), (66) and (71) can be used for a T-equivalent circuit for the Double -D system.

Using similar derivation, the equivalent inductances for the E-type system can be derived as:

$$L_{11} = L_{tx,tx} \tag{72}$$

$$L_{22} = L_{low,low} + L_{up,up} + L_{left,left} + L_{right,right} + 2(L_{low,left} + L_{low,up} + L_{low,right} + L_{up,left} + L_{up,right} + L_{left,right}) \tag{73}$$

$$M = L_{tx,low} + L_{tx,left} + L_{tx,right} + L_{tx,up} \tag{74}$$

3.3.2 Transmitter and receiver system analysis

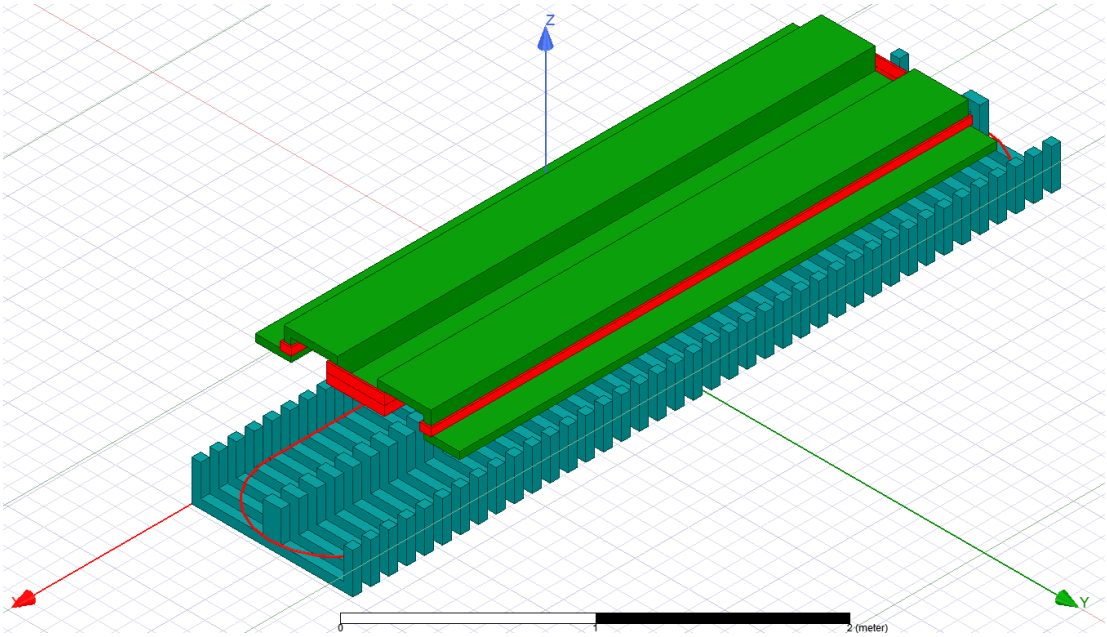

Figure 19. Ansys model of E-Type transmitter and receiver

Fig. 19 depicts the E-type transmitter and receiver system in the Ansys Maxwell simulation environment. In Fig. 19, the transmitter core embedded within one concrete slab is shown along with the entire receiver core which would be a part of the vehicle. This simplification or reduction of the entire transmitter – receiver system for magnetic analysis purposes is made primarily for reduction in runtime.

3.3.3 Validity of 2D FEA

The time taken to complete the 3D FEA of a single system design such as the one shown in Fig. 19 is over 30 minutes. Since the aim is to utilize the FEA in conjunction with the genetic algorithm toolbox – GOSET - we need rapid computations since this requires evaluating several thousand designs to arrive at the optimal design. The 2D FEA is a better candidate for optimization when the time taken is factor in the design process. The disadvantage of using 2D FEA is the error in the computation caused by not computing the flux that is normal to the plane of the design. Therefore, the difference between the parameters computed using 3D FEA and that computed using 2D FEA must be small in order for us to use 2D FEA in place of 3D FEA.

The following setup is used to compare the two methods. The 3D FEA model is already shown in Fig. 19. The only variable in this model is the thickness of the individual cores. The 2D FEA analysis in Maxwell assumes a length/depth of one meter for each component in the model. Therefore, in order to obtain the inductance, we need to multiply the inductance values given by the 2D FEA by the depth of the component with which the parameter is related. In order to compare the two methods, the cross section of the model is setup in the 2D FEA environment. The presence of the air gap between the cores in the 3D FEA is taken into account next. First, the core material properties are declared in the 2D FEA environment and the simulation is completed. Next the material properties are changed to that of air/vacuum and the simulation is run again to obtain the parameters when the winding is wound around an air/core. In order to obtain the parameter value in the results of the 2D simulation are multiplied with their respective lengths and then by the respective number of cores and air columns and added together.

The inductance calculation using 2D FEA is performed using (75) – (77).

$$L_{tx} = Ndt_{max}L_{tx,ferrite} + (N-1)(1-d)t_{max}L_{tx,air} \tag{75}$$

$$L_{rx} = dlen_{rx}L_{rx,ferrite} + (1-d)len_{rx}L_{rx,air} \tag{76}$$

$$M = dlen_{rx}M_{ferrite} + (1-d)len_{rx}M_{air} \tag{77}$$

Table 6 gives the definitions of the variables involved in (75) – (77).

Table 6. Variable description for (75) - (77)

Variable	Description
N	Number of transmitter cores in 1 concrete slab
t_{max}	Maximum thickness of 1 core
d	Ratio of thickness to maximum thickness of core
len_{rx}	Length of receiver core
$L_{tx,ferrite}$	Transmitter self-inductance with ferrite core computed using 2D FEA
$L_{tx,air}$	Transmitter self-inductance with air core computed using 2D FEA
$L_{rx,ferrite}$	Receiver self-inductance with transmitter ferrite core computed using 2D FEA
$L_{rx,air}$	Receiver self-inductance with transmitter air core computed using 2D FEA
$M_{ferrite}$	Mutual inductance with transmitter ferrite core computed using 2D FEA
M_{air}	Mutual inductance with transmitter air core computed using 2D FEA
L_{tx}	Equivalent transmitter self-inductance
L_{rx}	Equivalent receiver self-inductance
M	Equivalent mutual inductance

The parameters associated with the finite element simulation in ANSYS Maxwell have been specified in Table 7.

Table 7. ANSYS Maxwell FEA setup

Adaptive setup maximum number of passes	30
Adaptive setup percent error	1%
Mesh refinement per pass	30%
Minimum number of passes	2
Minimum number of converged passes	1

The comparison between the inductance values obtained using 3D FEA and the calculated values using 2D FEA and (75) – (77) is shown in Figs. 20 – 22 for the transmitter self-inductance, receiver self-inductance and the mutual inductance respectively. It can be seen clearly that the there is significant difference between the 3D FEA and 2D FEA values when the ferrite thickness is lower. This difference decreases as the thickness of the ferrite core increases. Therefore, we could replace the 3D FEA with 2D FEA provided we have a large ferrite(or magnetically permeable material) to air ratio. The main hindrance to this design is the brittle nature of ferrite since the transmitter core needs to bear the pressure of the heavy vehicles on the roadway.

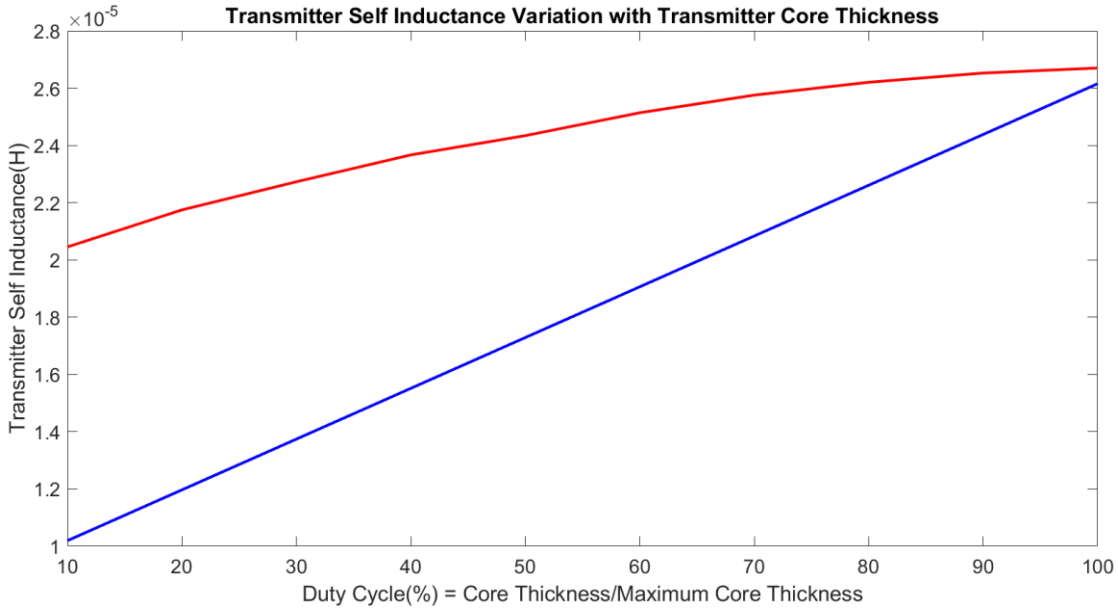

Figure 20. Transmitter self inductance comparison (3D FEA vs 2D FEA)

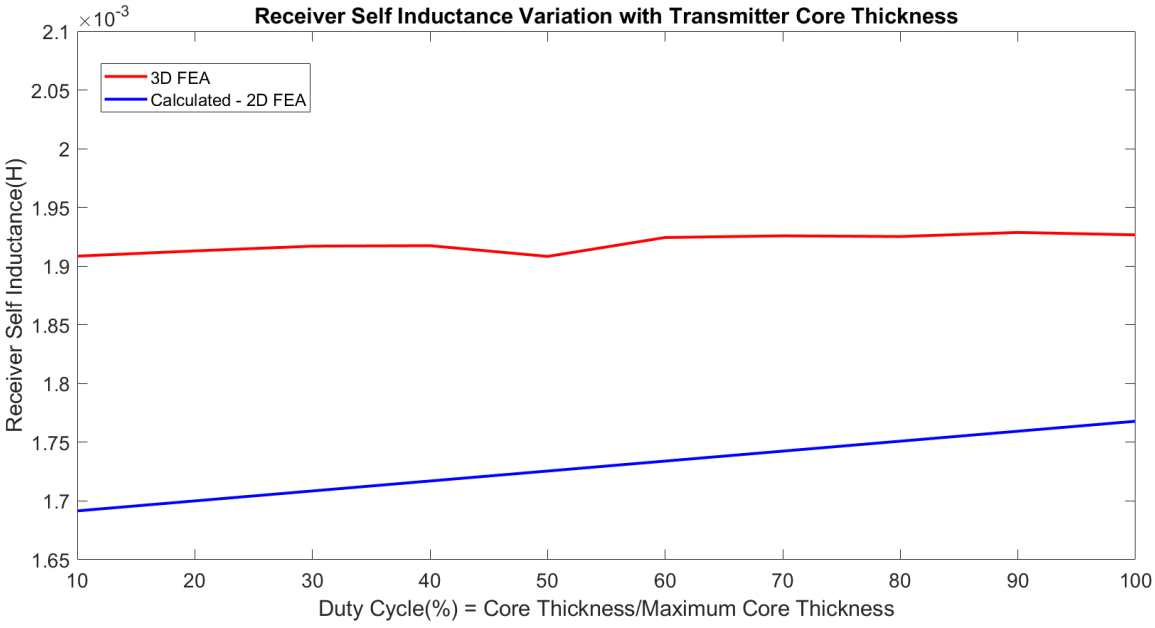

Figure 21. Receiver self inductance comparison (3D FEA vs 2D FEA)

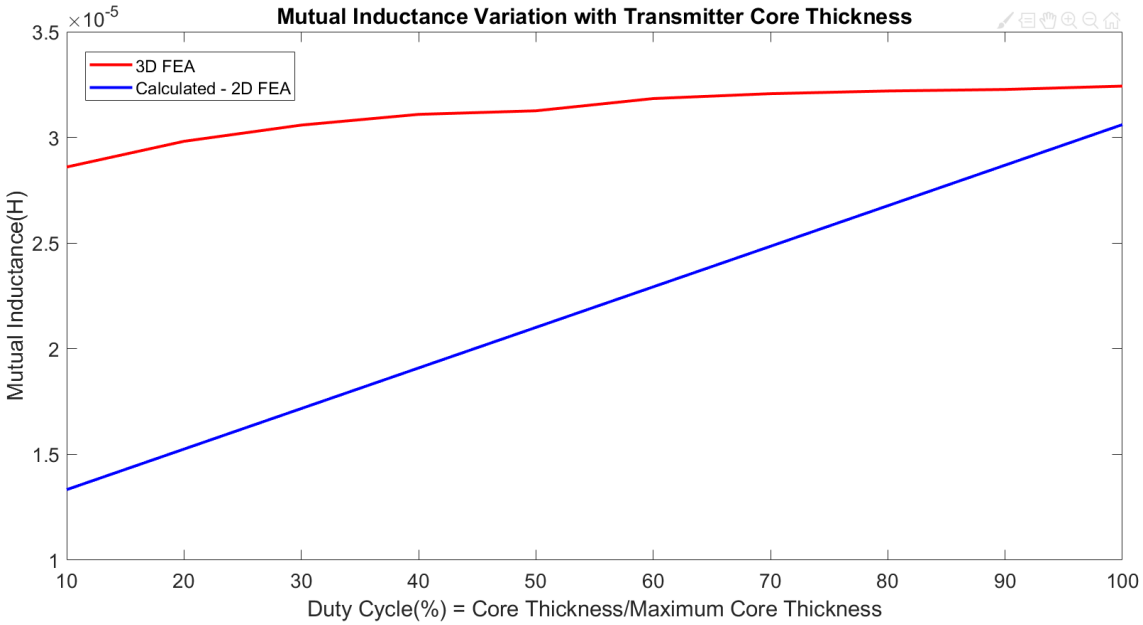

Figure 22. Mutual inductance comparison (3D FEA vs 2D FEA)

The solution to the problem is to use a core made of a magnetically permeable material which can bear the stress, such as the magnetizable concrete - MC40 made by MAGMENT. One of the main advantages of using MC40 is that we no longer need to make segmented cores for the transmitter. Instead the transmitter core could be made of a single block of concrete of the desired cross-section. This will lead to even lower difference between the results calculated using 2D and 3D analysis. Table 8 compares the inductance values obtained using 3D FEA the values obtained using of 2D FEA method for the Double-D system.

Table 8. Double-D System Inductance comparison

Inductances	3D FEA Values	2D FEA Values
Transmitter Self Inductance	2.255 mH	2.314 mH
Receiver Self Inductance	2.15 mH	1.99 mH
Mutual Inductance	0.516 mH	0.479 mH

It can be seen from Table. 8 that the inductance values are quite close to each other. Therefore, the Double-D system is selected for optimization.

Two important parameters of the Double-D system which are calculated for optimization are the mass of the transmitter and receiver and the core loss occurring within the transmitter and

receiver. The mass of the transmitter and receiver cores can be calculated by multiplying the volume of the transmitter and receiver with the density. The core loss occurring within the transmitter and receiver is calculated using 2D FEA in Ansys Maxwell.

3.4 Transmitter and Receiver Winding Ohmic Loss and Mass

The ohmic loss occurring within the transmitter and receiver windings is an important parameter contributing to the overall power loss occurring within the system and hence affecting the efficiency of the system. The high switching frequency of the power electronic converters increases the ohmic loss due to skin effect in a uniform conductor. In order to avoid this litz wire has been used which results in a uniform distribution of current within the conductor. The parameters influencing the ohmic loss include the resistance of the conductor, which depends on the length and the cross sectional are of the conductor, and the current through the conductor. In order to calculate the resistance of the windings litz wire data provided in [11] is employed. Fig. 23 shows a snapshot of the data used in calculation of the resistances.

Equivalent AWG	Circular Mil Area	Number of Wires	AWG of Wire	Film Coating[1]	Construction Type	Outer Insulation[2]	Nominal OD	Nominal LBS/ 1000 FT	Direct Current Resistance OHMS/ 1000 FT^	Construction
RECOMMENDED OPERATING FREQUENCY - 20 KHZ TO 50 KHZ										
30	100	4	36	S	1	-	.013	.318	110.100	4/36
28	175	7	36	S	1	-	.017	.557	62.900	7/36
26	250	10	36	S	1	SN	.023	.839	44.050	10/36
24	400	16	36	S	1	SN	.029	1.340	27.530	16/36
22	675	27	36	S	1	SN	.037	2.220	16.320	27/36
20	1025	41	36	S	1	SN	.044	3.350	10.740	41/36
18	1625	65	36	S	2	SN	.059	5.440	6.980	5X13/36
16	2625	105	36	S	2	SN	.074	8.740	4.320	3X35/36
14	4125	165	36	S	2	SN	.092	13.660	2.750	5X33/36
12	6625	265	36	S	2	SN	.116	21.830	1.710	5X53/36
10	10500	420	36	S	2	DN	.158	35.630	1.110	5X3X28/36
8	16500	660	36	S	2	DN	.197	59.010	.710	5X3X44/36
6	26250	1050	36	S	2	DN	.247	92.450	.450	5X5X42/36
4	45000	1800	36	S	2	DN	.322	156.420	.260	5X5X72/36
2	66500	2660	36	S	2	DN	.373	228.670	.180	7X5X76/36
1	84000	3360	36	S	5	SNB	.548	318.000	.140	6(5X4X28/36)
1/0	108000	4320	36	S	5	SNB	.655	420.000	.109	9(5X3X32/36)
2/0	135000	5400	36	S	5	SNB	.728	522.000	.087	9(5X3X40/36)
3/0	171000	6840	36	S	5	SNB	.870	682.000	.069	12(5X3X38/36)
4/0	211500	8460	36	S	5	SNB	.962	840.000	.055	12(5X3X47/36)

Figure 23. Litz wire specifications [11]

3.4.1 Transmitter Winding Ohmic Loss and Mass Calculation

The calculation of transmitter winding ohmic loss depends on the transmitter current and the resistance of the transmitter winding. The transmitter current and the conductor diameter are values generated by the optimization process and hence are inputs. Therefore, the only parameter affecting the resistance of the transmitter winding is the length of the winding.

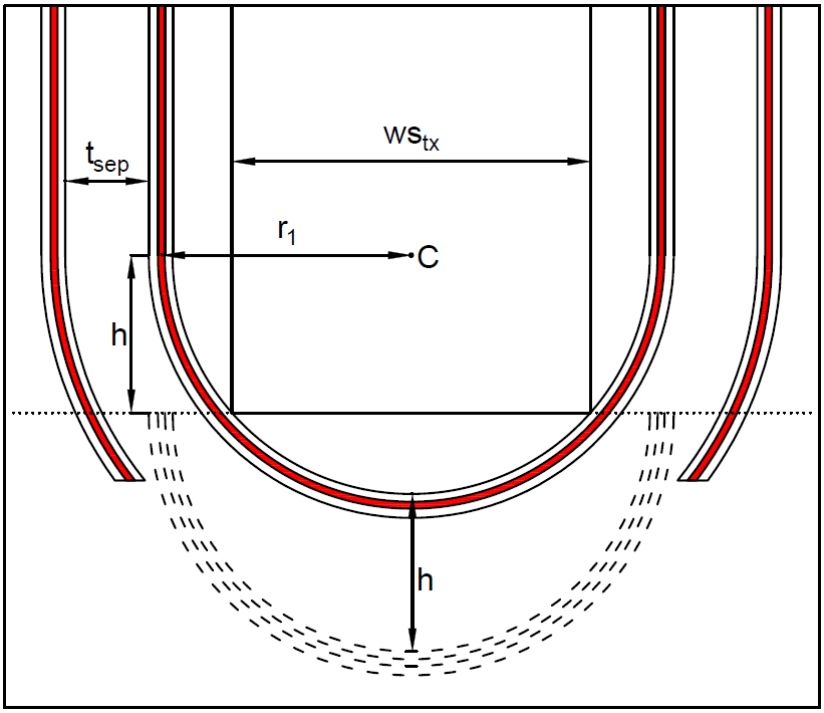

Figure 24. Transmitter top view

Fig. 24 is employed to calculate the length of the transmitter winding. In Fig. 24, the red part shows the conductor, the black lines next to the conductor indicate the edges of the slots, the white part indicates the transmitter core and the dotted part indicate a fictitious conductor or the position of the conductor before the conductor is placed in its position. The dotted part of the figure is instrumental in calculating the length of the straight part of the winding. First, the length of the semi-circular arc is calculated.

The radius of the arc formed by the first turn is calculated by (78):

$$r_1 = 0.5ws_{tx} + sep_{tx} + 0.5dia_{slot} \tag{78}$$

The separation between adjacent turns is given by:

$$s_t = t_{sep} + dia_{slot} \tag{79}$$

where,

t_{sep}: the separation between adjacent slots

The value of t_{sep} is kept fixed at 0.002 m in this study. Using (78) and (79), the radius of the arc formed by the kth turn can be calculated using (80).

$$r_k = r_1 + (k-1)s_t \tag{80}$$

The next step is to calculate the length of the straight part of the winding. Assume that before placing the conductor in the slot the conductor was in the dotted position. When it is in the dotted position the length of the straight part of the winding is equal to twice the length of the transmitter l_{tx} which is equal to 3.95 m. When the conductor is placed in the slot this length reduces by $2h$. The value of h is calculated using (81).

$$h = \sqrt{(0.5ws_{tx} + sep_{tx})^2 - 0.5ws_{tx}^2} \tag{81}$$

Using (78), (80) and (81) the total length of the transmitter winding can be calculated as:

$$len_{tw} = 2\left(\sum_{k=1}^{N} 2\pi r_k + 2N(l_{tx} - 2h)\right) \tag{82}$$

In order to calculate the resistance, the data given in Fig. 23 is employed and the following step by step procedure is adopted:

1. First the diameter of the conductor is used to find within which band the conductor belongs. The maximum and minimum radii - r_o and r_i – and the maximum and minimum resistances/304.8 m(1000 ft) - $resis_o$ and $resis_i$ are noted.
2. A linear interpolation is done to obtain the resistance/304.8 m corresponding to the diameter of the conductor. In the linear interpolation it is assumed that the variation of resistance per unit length is inversely proportional to the area. The resistance/304.8 m is calculated as:

$$resis_{tw} = resis_i + \left(\frac{resis_o - resis_i}{\frac{1}{a_o} - \frac{1}{a_i}}\right)\frac{1}{a_{tx}} \tag{83}$$

where,

$$a_o = \pi r_o^2 \tag{84}$$

$$a_i = \pi r_i^2 \tag{85}$$

$$a_{tx} = 0.25\pi dia_{tx}^2 \tag{86}$$

3. The resistance of the transmitter winding is then calculated as:

$$r_{tx} = resis_{tw}\left(\frac{len_{tw}}{304.8}\right) \tag{87}$$

In a similar manner the mass of the transmitter winding is calculated using (88):

$$m_{tx} = m_{tw}\left(\frac{len_{tw}}{304.8}\right) \tag{88}$$

In (88), m_{tw} refers to the mass per 304.8 m (1000 ft) of the conductor for a specific value of the conductor diameter. This value is once again calculated using a procedure similar to the resistance per 304.8 m – by using the data provided in Fig. 23 and linear interpolation.

3.4.2 Receiver Winding Ohmic Loss and Mass Calculation

In order to calculate the receiver winding ohmic loss and mass, the expression for winding resistance in Chapter 3 of [12] is utilized. This expression is given in (89).

$$r_{rx} = \frac{2V_{cl}N^2}{k_{pf}A_{cl}^2\sigma} \tag{89}$$

Where,

V_{cl}: Volume of a single coil

A_{cl}: Cross-sectional area of a single coil

k_{pf}: Packing factor

N: Number of turns

σ: Conductivity of the receiver winding conductor

The volume of the coil is calculated using (90).

$$V_{cl} = \left(2(l_{rx} \cdot Nh \cdot dia_{rx}) + 2(wt \cdot Nh \cdot dia_{rx}) + \pi(r_{co}^2 - r_{ci}^2)\right)N_v \cdot dia_{rx} \tag{90}$$

where,

$$r_{co} = r_{ci} + Nh \cdot dia_{rx} \tag{91}$$

r_{ci}: distance between receiver core tooth and coil

The value of r_{ci} is assumed to be fixed at 0.001 m.

The cross-sectional area of the coil is calculated using (92).

$$A_{cl} = N \cdot dia_{rx}^2 \tag{92}$$

The packing factor k_{pf} of the receiver coil is assumed to be 0.785 since it is assumed that the winding is arranged as shown in figure 3.2 (b) of Chapter 3 in [12].

In order to calculate the conductivity σ, the following procedure is followed:

1. The resistance per 304.8 m, $resis_{rw}$, corresponding to the diameter of the conductor is found using the procedure outlined for transmitter winding and the data shown in Fig. 23.
2. The value of the conductivity σ is found using (93).

$$\sigma = \frac{304.8}{(resis_{rw} a_{rx})} \tag{93}$$

In order to calculate the mass of the receiver winding the length of the winding is first calculated using (94).

$$len_{rw} = \frac{2V_{cl}}{A_{cl}} \tag{94}$$

Having found the length, the mass of the winding is calculated using (88).

4. COMPENSATION CIRCUIT

The large air gap between the transmitter and the receiver produces a large amount of leakage flux. To mitigate the power loss due to leakage flux, an inductor – capacitor – capacitor (LCC) compensation circuit is connected between the power electronic converter and the transmitter/receiver coil. The double-sided LCC compensation circuit makes the resonant frequency of the compensated coils independent of the coupling coefficient and the load [13]. Fig. 25 shows the circuit representation of the system with the LCC compensation circuit between the power electronics converter and the transmitter/receiver.

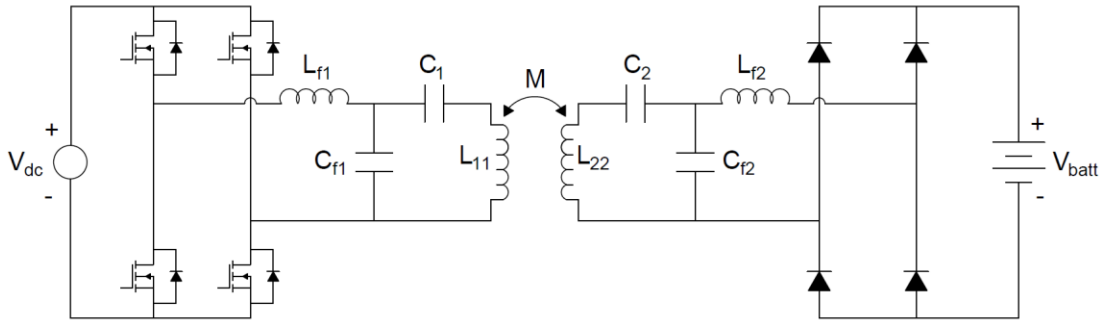

Figure 25. Circuit representation of DWPT system

The computation of the LCC circuit component values is provided in [13] and has been re-iterated for convenience in the following section. Fig. 26 shows the T-equivalent circuit with the circuit elements of the receiver side referred to the transmitter.

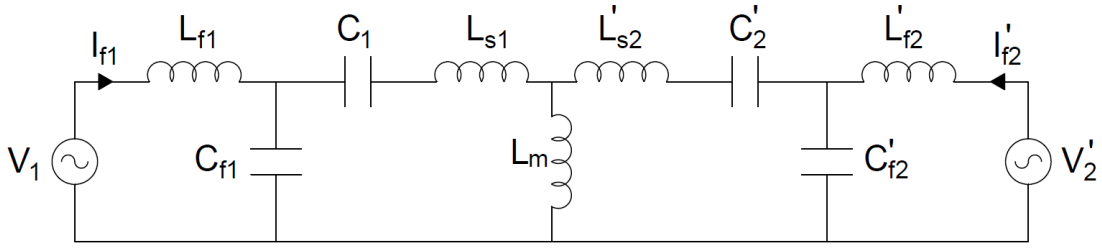

Figure 26. T-equivalent circuit with sinusoidal sources

In order to compute the values of the referred components, the turns ratio of the receiver turns to the transmitter turns is defined in (95).

$$n = \sqrt{\frac{L_{22}}{L_{11}}} \tag{95}$$

The expression for the coupling coefficient is given in (96).

$$k = \frac{M}{\sqrt{(L_{11}L_{22})}} \tag{96}$$

The calculations of the T-equivalent circuit components are then established using:

$$L_m = kL_{11} \tag{97}$$

$$L_{l1} = (1-k)L_{11} \tag{98}$$

$$L'_{l2} = \frac{(1-k)L_{22}}{n^2} \tag{99}$$

$$L'_{f2} = \frac{L_{f2}}{n^2} \tag{101}$$

$$C'_2 = n^2 C_2 \tag{102}$$

$$C'_{f2} = n^2 C_{f2} \tag{103}$$

$$V'_2 = \frac{V_2}{n} \tag{104}$$

In the analysis and the calculation of the circuit component values, it has been assumed that the voltage sources are sinusoidal. Once again phasor analysis and the superposition principle are employed for circuit analysis. Employing the superposition principle with only the transmitter side voltage source, one finds that the voltage source combined with the inductor L_{f1} and capacitor C_{f1} acts as a current source at the resonant frequency. At the resonant frequency, the impedances of the components are related as in (105).

$$Z_{Cf1} + Z_{Lf1} = 0 \tag{105}$$

where,

$$Z_{Cf1} = \frac{1}{j\omega C_{f1}} \tag{106}$$

$$Z_{Lf1} = j\omega L_{f1} \tag{107}$$

and ω is the resonant angular frequency in rad/s. The resonant frequency corresponds to the fundamental component of the inverter ac output.

Using (105) the value of the filter capacitor can be calculated as:

$$C_{f1} = \frac{1}{\omega^2 L_{f1}} \tag{108}$$

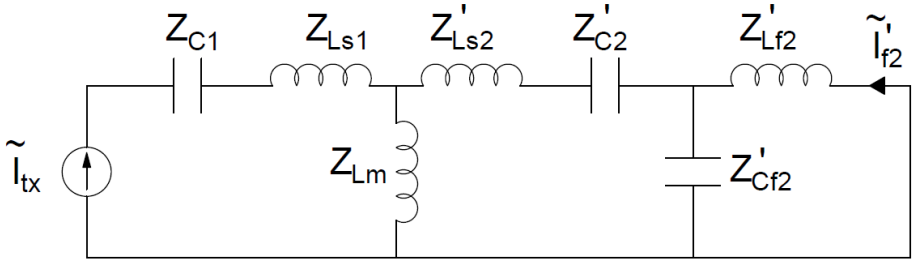

Figure 27. Equivalent circuit with filter components replaced by current source

Fig. 27 shows the circuit in Fig. 26 with the voltage source and the filter components replaced by the current source. The value of the current source is given by (109).

$$\tilde{I}_{tx} = \frac{\tilde{V}_1}{Z_{Lf1}} \tag{109}$$

At the resonant frequency the impedances of inductor L_{f2} and capacitor C_{f2} are related as (110).

$$Z_{Cf2} + Z_{Lf2} = 0 \tag{110}$$

where,

$$Z_{Cf2} = \frac{1}{j\omega C_{f2}} \tag{111}$$

$$Z_{Lf2} = j\omega L_{f2} \tag{112}$$

Therefore, at the resonant frequency the parallel circuit consisting of L_{f2} and C_{f2} act as an open circuit and no current flows through the inductance L'_{l2} and the capacitance C'_2. The net impedance presented to the current source can thus be expressed as:

$$Z_{load} = Z_{L11} + Z_{C1} \tag{113}$$

where,

$$Z_{C1} = \frac{1}{j\omega C_1} \tag{114}$$

$$Z_{L11} = j\omega L_{11} \tag{115}$$

The voltage appearing across this impedance is given by:

$$\tilde{V}_{load} = \tilde{I}_{load} Z_{load} = \tilde{V}_1 \frac{Z_{L11} + Z_{C1}}{Z_{Lf1}} \tag{116}$$

Selecting the value of Z_{C1} such that $\tilde{V}_{load} = \tilde{V}_1$, one finds:

$$Z_{C1} = Z_{Lf1} - Z_{L11} \tag{117}$$

Using (117) the value of the capacitor C_1 is then computed as:

$$C_1 = \frac{1}{\omega^2 (L_{11} - L_{f1})} \tag{118}$$

Using similar reasoning the receiver side capacitance values are computed using (119) – (120).

$$C_{f2} = \frac{1}{\omega^2 L_{f2}} \tag{119}$$

$$C_2 = \frac{1}{\omega^2 (L_{22} - L_{f2})} \tag{120}$$

From (108), (118), (119) and (120) one can see that the values of the capacitances depend on the values of the inductances. Before computing the values of the inductances, it is helpful to consider the phase relations between the input and output voltages and currents. The output current I_{f2} shown in Fig. 27 is the ac input to a full-bridge diode rectifier, and hence is in-phase with the ac voltage at the input to the rectifier. This voltage corresponds to the output/battery, when the current is positive, and the negative of the battery voltage when the voltage is negative. The value of I'_{f2} can be computed as:

$$\tilde{I}'_{f2} = \tilde{V}_1 \frac{Z_{Lm}}{Z_{Lf1} Z'_{Lf2}} \tag{121}$$

From (121) it can be observed that the current $\tilde{I}'_{f2}$ lags the input voltage by 90 degrees. Hence the voltage $\tilde{V}'_2$ lags the input voltage by 90 degrees. Similarly, the input current $\tilde{I}_{f1}$ can be calculated as follows:

$$\tilde{I}_{f1} = -V'_2 \frac{Z_{Lm}}{Z_{Lf1} Z'_{Lf2}} \tag{122}$$

From (122) it is clear that the input current leads the voltage $\tilde{V}'_2$ by 90 degrees, and hence is in phase with the input voltage $\tilde{V}_1$.

The inductances of the compensation circuit are now considered.

From (109),

$$L_{f1} = \frac{|\tilde{V}_1|}{\omega |\tilde{I}_{tx}|} \tag{123}$$

Next the formula for the inductance L_{f2} is derived. The circuit used to employ the second part of the superposition principle is shown in Fig. 28 for convenience.

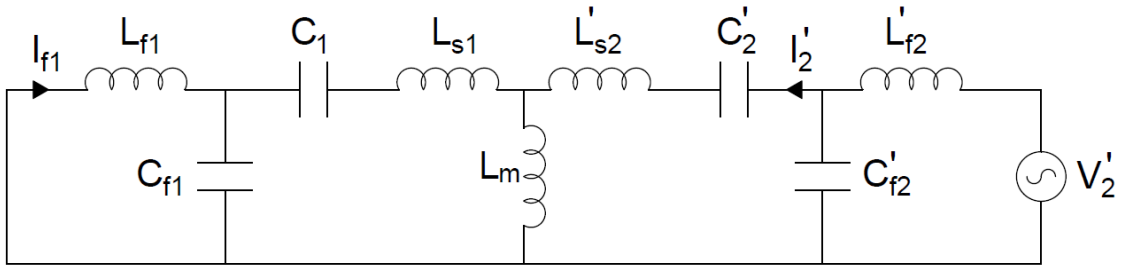

Figure 28. Circuit used to employ superposition principle

Making similar arguments when viewing the system from V'_2 as was done when viewing from V_1 the value of L_{f2} is derived to be:

$$L'_{f2} = \frac{|\tilde{V}'_2|}{\omega |\tilde{I}'_2|} \tag{124}$$

The value of the input current through inductance L_{f1} is computed as:

$$\tilde{I}_{f1} = -\frac{Z_{Lm}\tilde{I}_2'}{Z_{Lf1}} = -\frac{L_m\tilde{I}_2'}{L_{f1}} \tag{125}$$

Since the input current $\tilde{I}_{f1}$ and the voltage $\tilde{V}_1$ are in phase, the average power can be calculated as:

$$P = \tilde{V}_1\tilde{I}_{f1} = -\tilde{V}_1\frac{L_m I_2'}{L_{f1}} \tag{126}$$

From (126) the value of I_2' can be derived as:

$$I_2' = -\frac{P}{\tilde{V}_1}\frac{L_{f1}}{L_m} \tag{127}$$

Substituting the value of I_2' into (124) one obtains:

$$L_{f2}' = \frac{\left|\tilde{V}_2'\right|\left|\tilde{V}_1\right|L_m}{PL_{f1}} \tag{128}$$

Using (96), (97) and (98) the value of L_{f2} is expressed as:

$$L_{f2} = \frac{\left|\tilde{V}_2\right|\left|\tilde{V}_1\right|M}{PL_{f1}} \tag{129}$$

Thus, in review, the compensation circuit components are dependent on the ac input frequency, the power being delivered, the transmitter/receiver parameters, and the input/output voltage magnitude The compensation circuit components contribute to the mass and power loss occurring within the system. The power loss occurring within these components reduces the efficiency of the system and leads to temperature rise. The mass relates to the circuit cost, and in the case of the vehicle, additional power for propulsion.

4.1 Inductor Mass and Power Loss Estimation

To estimate the size and loss of the compensating circuit components, metamodels described in [14] have been used to estimate the inductor mass and power loss. The metamodels are based upon the design if the inductors used in dc-dc converter. To ensure the accuracy of the circuit model and the metamodel, the following assumptions have been made:

1. The conduction power loss occurring within the inductor is negligible compared to the core loss. Therefore, $r_{Lf1} = r_{Lf2} = 0$.
2. The hysteresis and eddy current loss occurring within the inductor is negligible. This assumption is made to ensure the accuracy of the metamodel which was applied for dc-dc converters. In dc-dc converters the variation in current traces a small internal loop within the

B-H curve and hence results in low hysteresis loss. On the other hand, the sinusoidal variation of the current in the DWPT application traces the entire B-H curve and results in higher hysteresis loss. Therefore, the power loss calculated by this metamodel is an optimistic estimate and the actual power loss may be higher.

The metamodel for mass and power loss described in [14] has been given in (130) and (131) respectively.

$$Mass = c_M E_{mi} \prod_{k=1}^{7} \left(J_{pk} E_{mi}^{1/3} + b_{M,k} \right)^{n_{M,k}} \tag{130}$$

$$Power\ Loss = 0.5 \cdot c_P E_{mi}^{1/3} \prod_{k=1}^{7} \left(J_{pk} E_{mi}^{1/3} + b_{P,k} \right)^{n_{P,k}} \tag{131}$$

where,

$$J_{pk} = \sqrt{2} \cdot J_{rms} \tag{132}$$

$$E_{mi} = 0.5 L i_{pk}^2 \tag{133}$$

$$c_M = 5.9851$$

$$c_P = 1.1021 \times 10^{-5}$$

Table 9. Inductor Metamodel Parameters

k	$b_{M,k}$	$n_{M,k}$	$b_{P,k}$	$n_{P,k}$
1	0	0.24700	0	0.54482
2	100.05	0.24673	1.1658×10^3	0.25254
3	100.05	-1.3215	1.1658×10^3	0.17114
4	3.4677×10^6	-1.2423	1.1659×10^3	0.24906
5	8.2537×10^6	2.4809	5.1412×10^4	-0.15241
6	7.3079×10^7	-2.0633	4.4344×10^5	0.52755
7	1.0430×10^8	1.5530	1.2330×10^6	-0.59614

In (132) – (133),

J_{rms}: RMS current density in the inductor windings. This value has been restricted to 5 A/mm^2.

L: Inductance of the inductor

i_{pk}: Peak current through the inductor

The value of the inductance L is calculated using (123) or (129) depending on whether it is the transmitter or receiver side inductor. The calculation of the i_{pk} is done using circuit analysis by employing phasor technique. The calculation of i_{pk} for the transmitter side inductor is explained below.

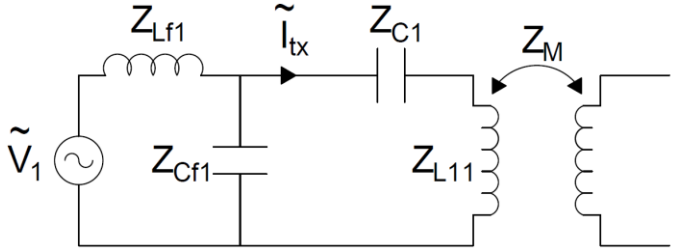

Figure 29. Circuit representation of transmitter side

Consider Fig. 29 which shows only the transmitter side components and the receiver winding for clarity. The voltage across the transmitter winding can be expressed in phasor form as in (134).

$$\tilde{V}_{tx} = Z_{L11}\tilde{I}_{tx} + M\tilde{I}_{rx} \tag{134}$$

The voltage across the parallel capacitor C_{f1} can be calculated as in (135).

$$\tilde{V}_{Cf1} = \tilde{V}_{tx} + Z_{C1}\tilde{I}_{tx} \tag{135}$$

The current through inductor L_{f1} is calculated using (136).

$$\tilde{I}_{Lf1} = \frac{\tilde{V}_1 - \tilde{V}_{Cf1}}{Z_{Lf1}} \tag{136}$$

The peak current is then calculated using (137).

$$i_{pk,Lf1} = \sqrt{2}\left|\tilde{I}_{Lf1}\right| \tag{137}$$

4.2 Capacitor Mass and Power Loss estimation

STHVF-AN : 20000Vdc / 4500Vac

P/N	Cn uF	Diameter D mm	Length L mm	dv/dt v/us	Peak Current $I_{p\sim p}$ A	ESL nH	ESR (mohm) 100KHz	Max. Amp 70C	Max. Amp 85C
STHVF-AN104K20kD	0.1	65	295	12900	1290	80	6.2	20	17
STHVF-AN124K20kD	0.12	65	295	12900	1548	80	5.6	20	17
STHVF-AN154K20kD	0.15	90	295	12900	1935	80	5	25	20
STHVF-AN204K20kD	0.2	90	295	12900	2580	80	4.5	30	25
STHVF-AN224K20kD	0.22	90	295	12900	2838	80	4	35	30
STHVF-AN254K20kD	0.25	90	295	12900	3225	80	3.4	40	35

Figure 30. Capacitor datasheet

To develop a metamodel of the capacitor, it was first assumed that a poly-propylene capacitor would be applied. This type of capacitor is often used in power electronic circuits and have advantages over alternatives that include capability to withstand high voltages in the range of several kilo volts, low dissipation factor and high quality factors. The manufacturer data sheet shown in Fig. 30, which was obtained from [15], shows the part of the datasheet used to obtain the data for capacitors. From Fig. 30 it can be seen that the capacitors have a voltage rating of 4.5 kV and the current rating of the capacitors vary from 20 A to 40 A depending upon the capacitance. In DWPT applications, the voltage across capacitors could be much higher than 4.5 kV. Moreover, the current through the capacitors is generally in the range of several hundreds of amperes. In order to avoid damage to the capacitors caused by high voltages and currents, a series- parallel combination of capacitors is assumed to be necessary. The circuit representation of this capacitor bank is shown in Fig. 31.

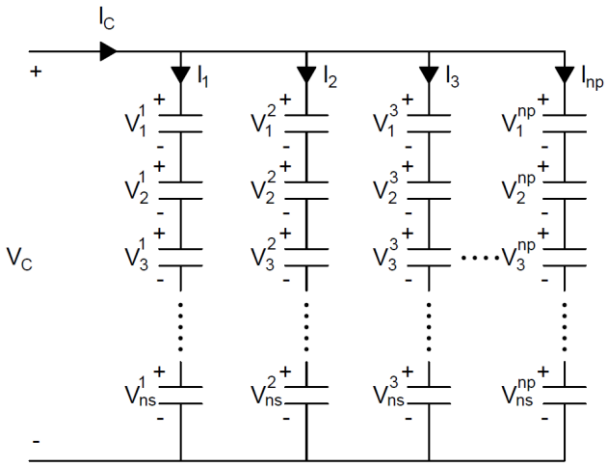

Figure 31. Capacitor bank

From Fig. 31 it is evident that the total number of capacitors is given by:

$$N_C = n_s \cdot n_p \tag{138}$$

where n_s is the number of capacitors connected in series and n_p is the number of parallel branches. The relationship between the variables shown in Fig. 31 are given in (139) – (144).

$$I_1 + I_2 + \cdots + I_{np} = I_C \tag{139}$$

$$\forall\, I_x \leq I_{rated} \tag{140}$$

where,

$$x \in \{1,2,3, \ldots\ n_p\} \tag{141}$$

I_{rated}: Minimum value of rated current in parallel branch x

$$V_1^x + V_2^x + \ldots + V_{ns}^x = V_C \tag{142}$$

$$\forall\, V_y^x \leq 4.5\ kV \tag{143}$$

where,

$$y \in \{1,2,3, \ldots\ n_s\} \tag{144}$$

While in reality each the capacitance of each capacitor in the capacitor bank could be different, it is assumed here that the capacitance of each capacitor in the capacitor bank is the same. This assumption makes the analysis relatively straightforward. This assumption results in the following relations among the individual branch currents and capacitor voltages:

$$I_1 = I_2 = \cdots = I_{np} = I \tag{145}$$

$$V_1^x = V_2^x = \ldots = V_{ns}^x = V \tag{146}$$

The current rating of a capacitor depends upon the capacitance and hence the number of parallel branches depend upon the capacitance value. Furthermore, the equivalent capacitance of the capacitor bank must be equal to the calculated value of the capacitance.

It can be seen from Fig. 30 that the equivalent series resistance(ESR) also depends upon the value of the capacitance. Using the data from Fig. 30 a map between capacitance and ESR was established (147):

$$ESR = \frac{\alpha}{C} + \beta \tag{147}$$

where,

$$\alpha = 4.224 \times 10^{-10}$$

$$\beta = 0.0020799$$

C: Capacitance of the specified capacitance

The values for α and β are obtained by minimizing the error between the computed ESR value and the ESR value obtained from the datasheet using a genetic optimization. In order to select the value of capacitance the following step by step procedure is adopted:

1. Calculate the minimum number of capacitors to be connected in series to meet the rated voltage constraint

$$N_{s,min} = ceil\left(\frac{V_C}{4.5 \times 10^3}\right) \quad (148)$$

2. Calculate the minimum number of parallel branches to meet the rated current constraint:

$$N_{p,min}^{C} = ceil\left(\frac{I_C}{I_{rated}^{C}}\right) \quad (149)$$

where,

$$C \in \{0.1, 0.12, 0.15, 0.2, 0.22, 0.25\}\ \mu F \quad (150)$$

$$I_{rated}^{C} \in \{17, 17, 20, 25, 30, 35\}\ A \quad (151)$$

The values in the sets C and I_{rated}^{C} are shown in Fig. 30.

3. Calculate the number of series connected capacitors needed to obtain the calculated equivalent capacitance using (152):

$$N_s^C = ceil\left(\frac{N_{p,min}^{C} C}{C_{eqv}}\right) \quad (152)$$

where,

C_{eqv} is the calculated equivalent capacitance of capacitor bank

4. Check if $N_s^C \geq N_{s,min}$. If yes, then proceed with step 5. If no, then calculate the new number of series and parallel connected capacitors as follows:

$$N_{p,new}^{C} = ceil\left(N_{p,min}^{C} \cdot \frac{N_{s,min}}{N_s^C}\right) \quad (153)$$

$$N_{s,new}^{C} = \ ceil\left(N_{p,new}^{C} \cdot \frac{C}{C_{eqv}}\right) \tag{154}$$

5. Declare the new values of series and parallel connected capacitors:

$$N_{p,new}^{C} = \ N_{p,min}^{C} \tag{155}$$

$$N_{s,new}^{C} = \ N_{s}^{C} \tag{156}$$

6. Calculate the branch current:

$$I_{br}^{C} = \frac{I_C}{N_{p,new}^{C}} \tag{157}$$

7. Calculate the power loss occurring in the capacitor bank for each capacitance value in C:

$$P_{loss}^{C} = \ N_{s,new}^{C} \cdot (I_{br}^{C})^2 \cdot ESR^{C} N_{p,new}^{C} \tag{158}$$

where,

$$ESR^{C} \ \in \ \{6.2, 5.6, 5, 4.5, 4, 3.4\}\, m\Omega \tag{159}$$

8. Find the capacitor series-parallel combination with the least power loss. This will be the selected number of series and parallel combination which will be used for making the capacitor bank. Let's denote the number of series capacitors as: n_s, and the number of parallel branches as: n_p.
9. Calculate the value of individual capacitance as:

$$C_{ind} = \frac{n_s C_{eqv}}{n_p} \tag{160}$$

10. Calculate the ESR using the metamodel in (147).
11. Calculate the equivalent ESR of the capacitor bank as follows:

$$ESR_{eqv} = \frac{n_s ESR_{calc}}{n_p} \tag{161}$$

12. Calculate the power loss occurring within the capacitor bank as follows:

$$P_{loss} = \ (I_C)^2 ESR_{eqv} \tag{162}$$

The calculation of the mass of the capacitor bank is now discussed. The dielectric used in the capacitor is poly-propylene. Assuming that the dielectric constitutes the majority of the mass of the capacitor, the mass of the capacitor bank can be calculated as follows:

$$Mass = \frac{\pi}{4} d^2 h \rho n_s n_p \tag{163}$$

where,

d: diameter of the capacitor

h: height of the capacitor

ρ: density of poly-propylene(dielectric)

5. POWER ELECTRONICS

The transmission of power from the transmitter to the receiver through electromagnetic fields requires high frequency operation. This is achieved by employing high frequency power electronic converters at both the transmitter side and the receiver side. At the transmitter end the conversion from DC-AC power is achieved by means of an inverter and the receiver side the high frequency AC power is converted to power using a rectifier. In this application the dominant or fundamental frequency of the power converters is in the range of several kilohertz. This excludes the operation of the converters using sine-delta modulation since this form of modulation requires the power electronic switches to switch at frequencies at least ten times the fundamental frequency. This requires that the switches should be able to operate at megahertz frequencies while handling power levels in the hundreds of kilowatts. The lack of market availability of such switches necessitates the operation of the power electronics converters utilizing phase-controlled modulation. An example of the output waveform of an inverter controlled using phase modulation is shown in Fig. 32.

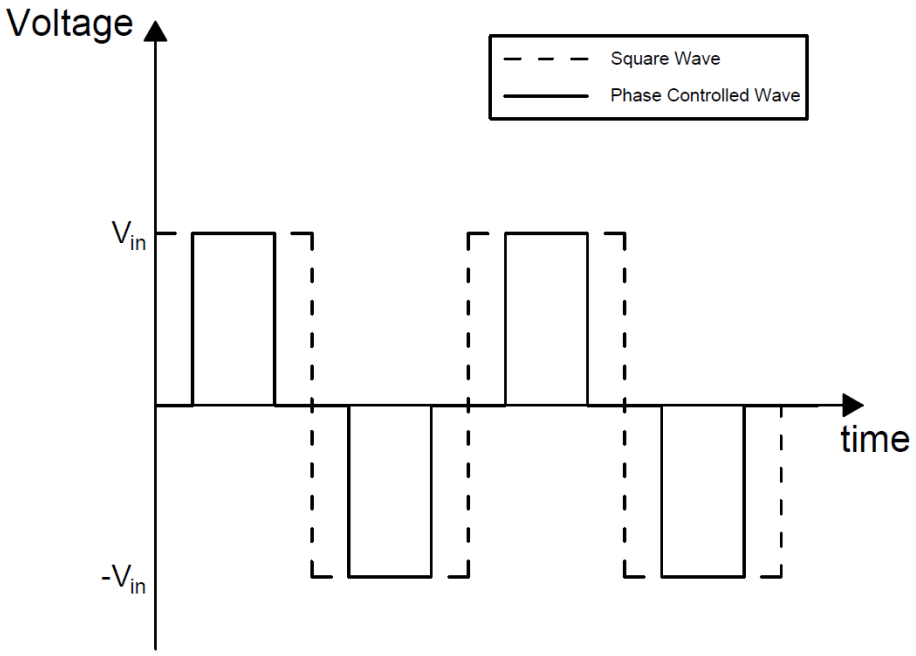

Figure 32. Phase controlled modulation output

It is visible that part of the square has been eliminated and hence the power provided to the load is reduced. This form of operation can be obtained by comparing an alternating square waveform with an alternating triangle wave and switching when the magnitude of the square waveform is less than the magnitude of the triangle waveform[16]. Note that in this form of modulation the frequency of the duty cycle waveform and the modulating triangle waveform are the same, which is in stark contrast to the sine delta modulation. This operation is shown in Fig. 33.

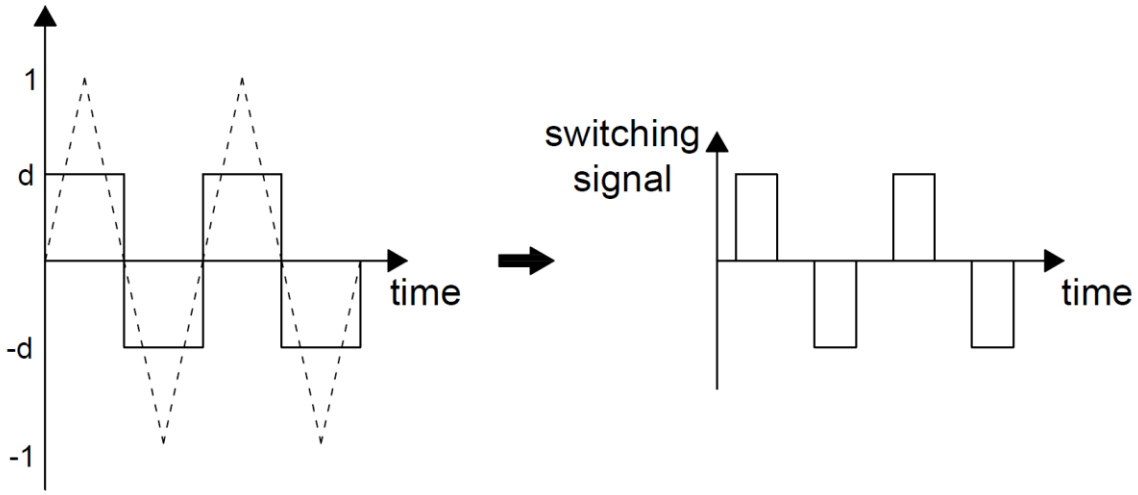

Figure 33. Switching signal generation

Using this switching strategy, the relation between the fundamental component of the voltage waveform and the magnitude of the duty cycle waveform is derived. In order to derive the expression the triangular modulation wave's amplitude is assumed to be 1 and the duty cycle waveform has an amplitude of 'd' as shown in Fig. 33.

The triangular modulation wave can then be described by:

$$M(t) = \begin{cases} \dfrac{t}{T/4}, & 0 \le t \le T/4 \\ -\dfrac{t}{T/4} + 2, & T/4 \le t \le 3T/4 \\ \dfrac{t}{T/4} - 4, & 3T/4 \le t \le T \end{cases} \quad (164)$$

The duty cycle waveform can be described by:

$$d(t) = \begin{cases} d, & 0 \le t \le T/2 \\ -d, & T/2 \le t \le T \end{cases} \tag{165}$$

and the time points of intersection are established using:

$$t_{ip} = \frac{dT}{4} \tag{166}$$

$$t_{fp} = \frac{(2-d)T}{4} \tag{167}$$

$$t_{in} = \frac{(2+d)T}{4} \tag{168}$$

$$t_{fn} = \frac{(4-d)T}{4} \tag{169}$$

Since the voltage waveform has an odd wave symmetry, the average value and the coefficients of the co-sinusoidal terms of the Fourier series of the voltage waveform are zero. The coefficients can be sinusoidal terms which are calculated using:

$$b_n = \frac{1}{T/2}\int_0^T V_{in} \sin\left(\frac{n\pi t}{T/2}\right) dt \tag{170}$$

$$b_n = \frac{1}{T/2}\left\{\int_{t_{ip}}^{t_{fp}} V_{dc} \sin\left(\frac{n\pi t}{T/2}\right) dt - \int_{t_{in}}^{t_{fn}} V_{dc} \sin\left(\frac{n\pi t}{T/2}\right) dt\right\} \tag{171}$$

$$b_n = \frac{4V_{dc}}{n\pi} \sin\left(\frac{n\pi}{2}\right) \cdot (1-d)\cos(n\pi) \sin\left(-\frac{n \cdot \pi}{2}\right) \tag{172}$$

The fundamental component is given by $n = 1$:

$$b_1 = \frac{4V_{dc}}{\pi} \sin\left(\frac{\pi}{2}(1-d)\right) \tag{173}$$

Therefore, the fundamental component of the voltage waveform can be expressed as:

$$V_1 = \frac{4V_{dc}}{\pi} \sin\left(\frac{\pi}{2}(1-d)\right) \sin(\omega t) \tag{174}$$

Although the above formula appears interesting from a control perspective, controls are not of primary interest in this research. Rather, it is used to establish the expected losses. In order to calculate the power loss occurring within the power electronics we focus on calculating the maximum value of power loss. It must be noted that it is assumed that this control strategy is applied only at the transmitter end to control the power output of the inverter. It is further assumed that at the receiver end the rectifier operates as a diode rectifier and phase control is not employed. The power loss occurring within the power electronic converters is maximum when the transmitter is operated at its maximum rated power capacity. During this operation the voltage at the inverter output terminals will be a complete square wave, the amplitude of the fundamental component of which can be obtained by making the value of d in (174) equal to zero. The amplitude of the fundamental component of the voltage waveform is given in (175).

$$V_1 = \frac{4V_{dc}}{\pi} \tag{175}$$

At the receiver end the rectifier switches are controlled in such a manner that the converter acts as a diode rectifier.

The two main types of losses occurring within power electronics switches during operation are the following:

1. Conduction Loss: Conduction loss occurs within each switch when the switch is ON and is conducting current.
2. Switching Loss: Switching loss takes place whenever a switch transitions from an ON state to an OFF state or vice versa.

In order to calculate the losses occurring within the power electronics converters, it has been assumed that the converter is made up of Wolfspeed CAS300M17BM2 switches. The datasheet of this device is used to obtain relevant information to calculate the switching and conduction losses and the number of the switches in each converter is calculated using the optimization algorithm. The maximum current rating of the Wolfspeed CAS300M17BM2 switch is 300 A which is less than the typical current value in high power DWPT applications. In order to limit the current to rated values and also to reduce the junction temperature of the power electronic converters multiple devices are used to form one phase leg as shown in Fig. 34. It can be seen from Fig. 34 that each phase leg is made up of three Wolfspeed CAS300M17BM2 switches.

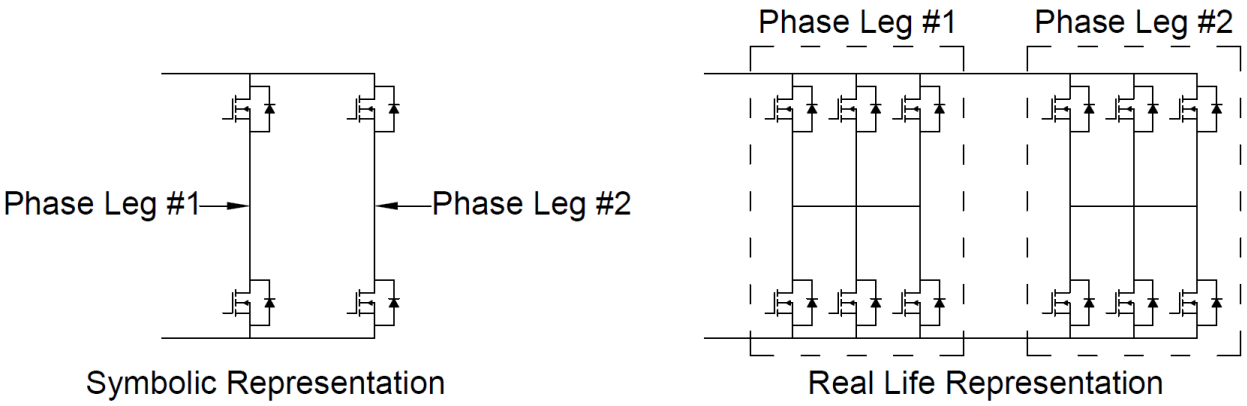

Figure 34. Phase legs made of multiple representation

Before providing an explanation for the calculation of the losses a description of the metamodels of the inverter and rectifier is given.

5.1 Power Electronics Metamodel

In order to approximate the dimensions and loss associated with the power converters, a metamodel has been established using data from a commercial 200 kW 3-phase inverter that utilizes Wolfspeed CAS300M17BM2 modules [17]. The mass and volume of this inverter was used as a basis to estimate the mass and volume of the inverter and rectifier. The mass includes that of the power switches and their respective heatsink, the associated filter, the common mode choke and the enclosure of the converter. The inputs and outputs of the metamodel are listed in Tables 10 – 11.

It can be seen that the only changes in the inputs are the differences in the voltage inputs. In order to calculate the current for the inverter and the rectifier (176) and (177) are employed respectively.

Table 10. Power Electronics Metamodel Inputs

Converter	Input Variable	Description
Inverter	V_{dc}	Input DC voltage to the inverter
	P_{out}^{inv}	Output power of the inverter
	pf_{inv}	Power factor
	dev_{inv}	Number of devices
	fsw_{inv}	Triangle wave frequency
	fac_{inv}	Desired AC frequency
	T_{amb}	Ambient temperature
Rectifier	V_{ac}	Input AC voltage to the rectifier
	P_{out}^{rec}	Output power of the rectifier
	eff_{recd}	Desired efficiency of the rectifier
	pf_{rec}	Power factor (= 1)
	dev_{rec}	Number of devices
	fsw_{rec}	Triangle wave frequency
	fac_{rec}	Desired AC frequency
	T_{amb}	Ambient temperature

Table 11. Power Electronics Metamodel Output

Converter	Output Variable	Description
Inverter	eff_{inv}	Inverter efficiency
	$Tjunc_{inv}$	Junction temperature
	$mass_{inv}$	Inverter mass
	vol_{inv}	Inverter volume
Rectifier	eff_{rec}	Calculated rectifier efficiency
	$Tjunc_{rec}$	Junction temperature
	$mass_{rec}$	Rectifier mass
	vol_{rec}	Rectifier volume

$$I_{inv} = \frac{P_{out}^{inv}}{\left(\frac{4}{\pi\sqrt{2}} V_{dc} \cdot pf_{inv}\right)} \tag{176}$$

$$I_{rec} = \frac{P_{out}^{rec}}{(V_{ac} \cdot pf_{rec} \cdot eff)} \tag{177}$$

It has been assumed that the device is capable of operating at currents higher than the rated currents. In our case it has been assumed that the maximum current the device can handle is 500A. In order to measure the switching losses at these, higher current values, the plot of the switching energy loss versus drain current provided in the datasheet and shown in Fig. 35 is used.

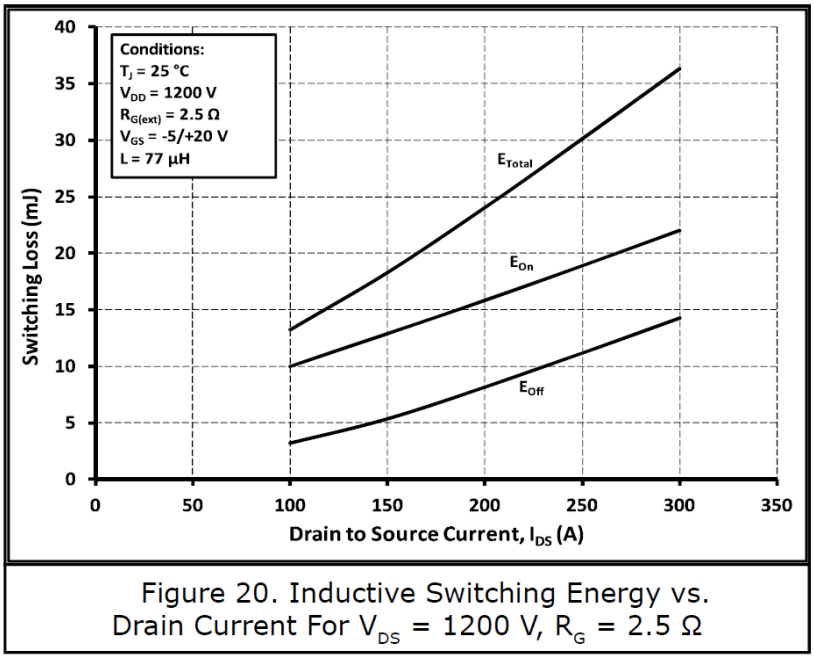

Figure 35. Switching energy loss curves

It has been assumed that the variation of E_{on} and E_{off} with the current is linear and hence a simple linear extrapolation of the characteristic is done in order to set the limits of the switching power loss. First the slope of the switching energy loss versus current characteristic is calculated using (178) and (179) for the on-state and off-state energy loss respectively.

$$E_{on,slope} = \frac{E_{on,f} - E_{on,i}}{I_f - I_i} \tag{178}$$

$$E_{off,slope} = \frac{E_{off,f} - E_{off,i}}{I_f - I_i} \tag{179}$$

The values and the description of the variables used in (178) and (179) are given in Table 12.

Table 12. Variable description for (178) and (179)

Variable	Value	Description
$E_{on,f}$	$23\ mJ$	Maximum specified on-state switching energy loss
$E_{on,i}$	$10\ mJ$	Minimum specified on-state switching energy loss
$E_{off,f}$	$14\ mJ$	Maximum specified off-state switching energy loss
$E_{off,i}$	$3.5\ mJ$	Minimum specified off-state switching energy loss
I_f	$300\ A$	Maximum specified device current
I_i	$100\ A$	Minimum specified device current
$E_{on,slope}$	–	On-state energy loss slope
$E_{off,slope}$	–	Off-state energy loss slope

The values of the on-state and off-state energy loss beyond the range specified in the datasheet is calculated using (180) and (181).

$$E_{on,val} = E_{on,i} + E_{on,slope} \times (I_{ex} - I_i) \tag{180}$$

$$E_{off,val} = E_{off,i} + E_{off,slope} \times (I_{ex} - I_i) \tag{181}$$

Here the vector I_{ex} is the vector of current values that are beyond the rated current value. The values used in the vector I_{ex} is given below:

$$I_{ex} = [400\ A,\ \ 500\ A]$$

Assuming that the total output current of the inverter or the input current of the rectifier divides equal among all the phase legs of the converter, the total on-state and off-state rated energy loss values and the corresponding current values are calculated using (182), (183) and (184) respectively.

$$E_{on.Vect} = dev_x[0, 10, 23, E_{on,val}] \cdot 10^{-3} \tag{182}$$

$$E_{off.Vect} = dev_x[0, 3.5, 14, E_{off,val}] \cdot 10^{-3} \quad (183)$$

$$I_{sw,Vect} = dev_x[0, 100, 300, I_{ex}] \quad (184)$$

where,

$$x \in \{inv, rec\}$$

In (182) – (184) the numerical values included as part of the energy and current vector are taken from the graph shown in Fig. 35. Furthermore, in (182) and (183) the multiplication by 10^{-3} comes from the fact that the values for these quantities provided in the datasheet are in milli-joules. In a similar manner the effective conductive resistance (drain to source resistance) of the device and the flyback diode connected across it is calculated using (185) and (186).

$$R_{DS} = \frac{R_{DS,dev}}{dev_x} \quad (185)$$

$$R_{diode} = \frac{R_{diode,dev}}{dev_x} \quad (186)$$

The values and description of the variables used in (185) and (186) have been given in Table 13.

Table 13. Variable Description for (185) and (186)

Variable	Value	Description
$R_{DS,dev}$	16.2 $m\Omega$	Drain to source resistance of single device
$R_{diode,dev}$	5.0 $m\Omega$	Resistance of single diode
R_{DS}	–	Equivalent resistance of MOSFET part of the converter
R_{diode}	–	Equivalent resistance of diode part of the converter

The calculation of the conduction and switching loss is done by considering only the fundamental component of the inverter output current. Using the r.m.s value of current calculated earlier in (176) and the phase difference with respect to the inverter output voltage, we can express the fundamental component of the inverter output current waveform using (187).

$$I_{out} = \sqrt{2} I_{inv} \cos(2\pi f ac_{inv} t - \varphi) \quad (187)$$

$$\varphi = \cos^{-1}(pf_{inv}) \quad (188)$$

5.2 Mass and Volume Calculation

Fig. 34 shows that each phase leg consists of multiple Wolfspeed CAS300M17BM2 modules to avoid currents more than the rated current and also to avoid overheating of the device. It is also visible from Fig. 34 that each device consists of two MOSFETs and two freewheeling diodes. In order to calculate the mass and volume of the power electronic converters the mass and volume of the following components are considered:

1. Power stage phase leg module, heatsink and connectors
2. Common mode inductor

The values assumed for each component of the power electronic converters and the base line switching frequency for the filter and the common mode choke are shown in Table 14.

Table 14. Variables used in mass and volume calculation of power electronic converters

Variable Name	Value	Description
$Mass_{pws}$	0.5 kg	Mass of the power stage of a single device
Vol_{pws}	1066 cm^3	Volume of the power stage of a single device
$Mass_{cc}$	1 kg	Mass of common mode inductor associated with a single device
Vol_{cc}	853 cm^3	Volume of common mode inductor associated with a single device
$Mass_{PWS}$	-	Mass of the power stage of the entire converter
Vol_{PWS}	-	Volume of the power stage of the entire converter
$Mass_{CC}$	-	Mass of the common mode inductor of the entire converter
Vol_{CC}	-	Volume of the common mode inductor of the entire converter
$Mass_{ENC}$	-	Mass of the enclosure
Vol_{ENC}	-	Volume of the enclosure
f_{base}	60 kHz	Base frequency of the filter
f_{sw}	-	Switching frequency of the converter

The mass and volume of the power stage phase leg, heatsink and connectors are calculated using (189) and (190) respectively.

$$Mass_{PWS} = Mass_{pws} \times dev_x \tag{189}$$

$$Vol_{PWS} = Vol_{pws} \times dev_x \tag{190}$$

In order to calculate the mass and volume of the filter and common mode choke the individual filter and common mode choke mass and volume are first scaled by the switching frequency and then multiplied by the number of devices. The calculation of the mass of the common mode inductor are shown in (191) – (192).

$$Mass_{CC} = Mass_{cc} \times (f_{sw}/f_{base}) \times dev_x \tag{191}$$

$$Vol_{CC} = Vol_{cc} \times (f_{sw}/f_{base}) \times dev_x \tag{192}$$

The summation of (189), and (191) constitutes the total mass of the power electronic components. Similarly, the summation of (190), and (192) constitutes the total volume of the power electronic components. In order to calculate the mass and volume of the converter enclosure, given by (193) and (194) respectively, are employed.

$$Mass_{ENC} = 0.7 \times (Mass_{PWS} + Mass_{CC}) \tag{193}$$

$$Vol_{ENC} = 0.33 \times (Vol_{PWS} + Vol_{CC}) \tag{194}$$

Finally, the total mass and volume of the power electronic converters are calculated using (195) and (196) respectively.

$$Mass_x = Mass_{PWS} + Mass_{CC} + Mass_{ENC} \tag{195}$$

$$Vol_x = Vol_{PWS} + Vol_{CC} + Vol_{ENC} \tag{196}$$

5.3 Conduction Loss Calculation

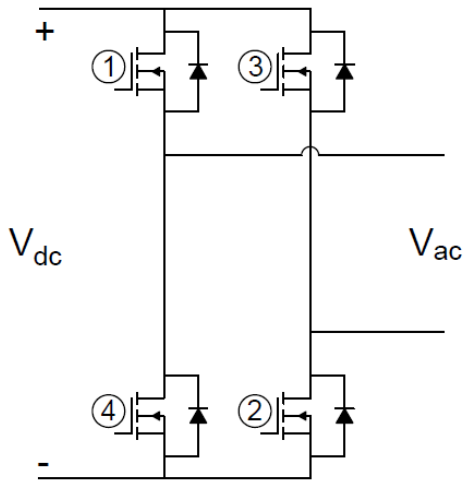

Figure 36. Power electronic converter

Fig. 36 shows the circuit representation of the converter. The switching strategy is assumed to be complimentary. This means that when the switches 1 and 2 are on then 3 and 4 are off and vice versa. In order to account for the total conduction loss occurring within the device the conduction loss occurring within the transistor and also the diode part of the device is calculated. In order to calculate the conduction loss the following procedure is adopted:

1. A vector of time values ranging from zero to the value of one period is created.
2. The value of current in a switch/diode pair corresponding to each element of the time vector is calculated using (187).
3. The conduction loss vector for each time value occurring in each switch and its corresponding flyback diode is calculated as follows:
    a. When switches 1 and 2 are on and the ac current value is positive then the MOSFET conduction loss is calculated.
    b. When switches 1 and 2 are on and the ac current value is negative then the diode conduction loss is calculated.
    c. When switches 3 and 4 are on and the ac current value is negative then the MOSFET conduction loss is calculated.

d. When switches 3 and 4 are on and the ac current value is positive then the diode conduction loss is calculated.

4. The total conduction energy loss over a period is calculated for the switch pairs and the corresponding diodes by summing the energy loss vector.
5. The conduction power loss is calculated by dividing the total conduction energy loss by the period.

The calculation of conduction energy loss occurring within the MOSFET and the flyback diode is calculated using (197) and (198) respectively.

$$E^t_{cond,MOSFET} = dt \times (I^t_{ac})^2 \times R_{DS} \tag{197}$$

$$E^t_{cond,diode} = dt \times \left(\left(V_{fd} \times I^t_{ac} \right) + \ (I^t_{ac})^2 \times R_{diode} \right) \tag{198}$$

5.4 Switching Loss Calculation

The calculation of the switching loss entails keeping track of the switching sequence of the power electronic switches. The switching energy loss is calculated by a simple linear interpolation of the curve shown in Fig. 35 by using (182) and (183). The steps involved in calculating the switching energy loss are given below:

1. A vector of time values ranging from zero to the value of one period is created.
2. The current value corresponding to each element of the time vector is calculated using (187).
3. The switching energy loss occurring at every instant of time is now calculated using the following steps.
    a. If the current value is positive and the switches 1 and 2 were off in the previous instant of time and are on at the current instant then interpolate the on-state energy loss curve.
    b. If the current value is positive and the switches 1 and 2 were on in the previous instant of time and are off at the current instant then interpolate the off-state energy loss curve.

c. If the current value is negative and the switches 3 and 4 were off in the previous instant of time and are on at the current instant then interpolate the on-state energy loss curve.
d. If the current value is negative and the switches 3 and 4 were on in the previous instant of time and are off at the current instant then interpolate the off-state energy loss curve.

4. The total switching energy loss over a period is calculated for the switch pairs by summing the switching energy loss vector.
5. The switching power loss is calculated by dividing the total switching energy loss by the period.

5.5 Junction Temperature Calculation

Another important parameter to be calculated is the junction temperature of the power electronic devices. The conduction and switching energy loss occurring within the Wolfspeed CAS300M17BM2 modules results in an increase in the junction temperature of the device. In order to keep the junction temperature within the acceptable limit, the device is attached to a heat sink which in turn dissipates the heat to the environment. Fig. 37 shows the arrangement and the various components of power loss which contribute to an increase in temperature.

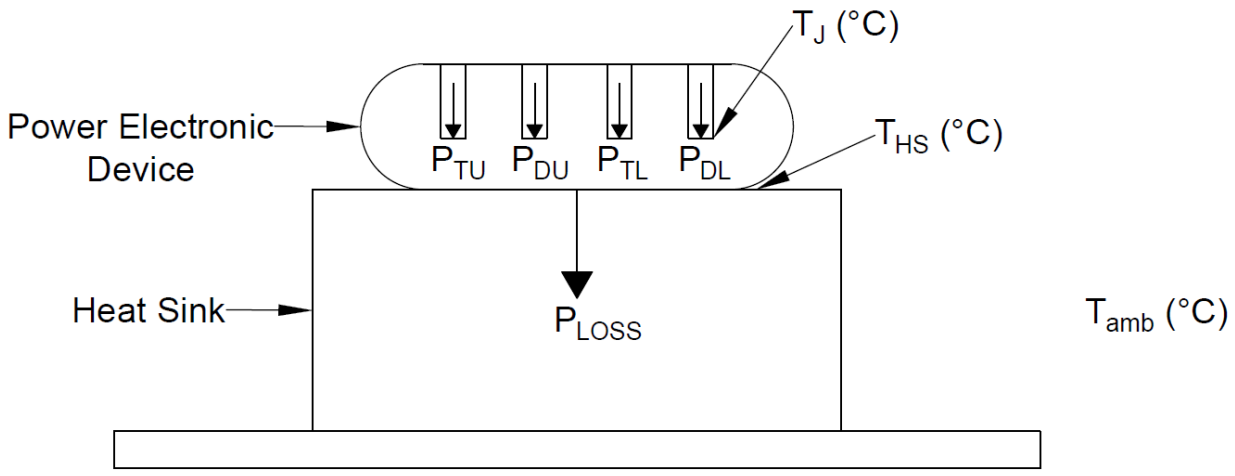

Figure 37. Power electronic device arrangement for heat loss

In order to calculate the junction temperature, the power loss occurring in the individual MOSFETs and their corresponding diode are important. Another important factor influencing the junction temperature is the ambient temperature which has been specified as an input in Table 10. The thermal equivalent circuit used to estimate the junction temperature is shown in Fig. 38.

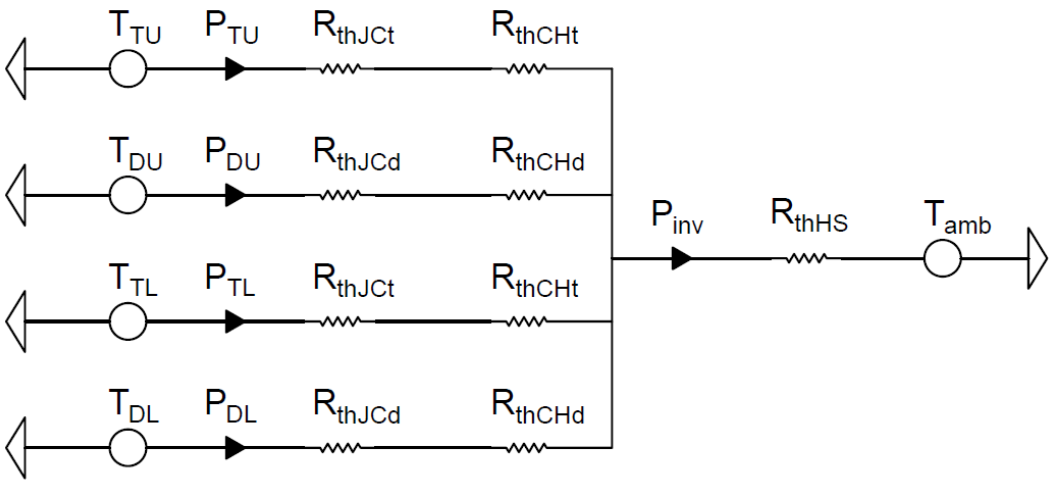

Figure 38. Thermal equivalent circuit of power electronic converter

Herein, the temperatures at different junctions have been shown analogous to a voltage source and the power being dissipated by different devices are analogous to current. The thermal impedances shown in Fig. 38 are the effective thermal impedance of different parts of the power electronic converter which have been calculated using (199) – (202).

$$R_{thJCt} = \frac{R_{thJC,MOSFET}}{dev} \tag{199}$$

$$R_{thCHt} = \frac{R_{thCH,MOSFET}}{dev} \tag{200}$$

$$R_{thJCd} = \frac{R_{thJC,diode}}{dev} \tag{201}$$

$$R_{thCHd} = \frac{R_{thCH,diode}}{dev} \tag{202}$$

Using the thermal equivalent circuit, the temperature of the heat sink is first calculated using (203).

$$T_{HS} = T_{amb} + P_x \cdot R_{thHS} \quad (203)$$

Next the junction temperature of each component of the device is calculated using (204) – (207).

$$T_{TU} = T_{HS} + P_{TU} \cdot \left(R_{thJCt} + R_{thCHt}\right) \quad (204)$$

$$T_{DU} = T_{HS} + P_{DU} \cdot \left(R_{thJCd} + R_{thCHd}\right) \quad (205)$$

$$T_{TL} = T_{HS} + P_{TL} \cdot \left(R_{thJCt} + R_{thCHt}\right) \quad (206)$$

$$T_{DL} = T_{HS} + P_{DL} \cdot \left(R_{thJCd} + R_{thCHd}\right) \quad (207)$$

Having calculated the individual junction temperature of each component, the power electronic converter junction temperature is estimated as the maximum among the all the junction temperatures.

$$T_{junc} = \max\left(T_{TU}, T_{DU}, T_{TL}, T_{DL}\right) \quad (208)$$

The definitions of the variables and the values of thermal impedances used for the calculation defined in (199) – (208) have been provided in Table 15.

Table 15. Description of variables in (199) – (208)

Variable Name	Value	Description
$R_{thJC,MOSFET}$	0.071 Ω	Thermal impedance from junction to adhesive for MOSFET part of the device
$R_{thCH,MOSFET}$	0.02 Ω	Thermal impedance from adhesive to heat sink for MOSFET part of the device
$R_{thJC,diode}$	0.065 Ω	Thermal impedance from junction to adhesive for diode part of the device
$R_{thCH,diode}$	0.02 Ω	Thermal impedance from adhesive to heat sink for diode part of the device
R_{thJCt}	-	Equivalent thermal impedance from junction to adhesive associated with MOSFET for the entire converter
R_{thCHt}	-	Equivalent thermal impedance from adhesive to heat sink associated with MOSFET for the entire converter
R_{thJCd}	-	Equivalent thermal impedance from junction to adhesive associated with diode for the entire converter
R_{thCHd}	-	Equivalent thermal impedance from adhesive to heat sink associated with diode for the entire converter
R_{thHS}	0.02 Ω	Thermal impedance of heat sink
P_x	-	Total inverter or rectifier power loss
P_{TU}	-	Upper MOSFET power loss
P_{DU}	-	Upper diode power loss
P_{TL}	-	Lower MOSFET power loss
P_{DL}	-	Lower diode power loss
T_{HS}	-	Temperature of the heat sink
T_{TU}	-	Calculated upper MOSFET junction temperature
T_{DU}	-	Calculated upper diode junction temperature
T_{TL}	-	Calculated lower MOSFET junction temperature
T_{DL}	-	Calculated lower diode junction temperature
T_{amb}	-	Ambient temperature
T_{junc}	-	Junction temperature of the entire converter

6. OPTIMIZATION AND RESULTS

6.1 Optimization

The design of the transmitter-receiver system for dynamic wireless charging involves the selection of the following components:

1. Transmitter and Receiver – core dimensions, conductor geometry, and number of turns constituting their respective windings
2. Compensation circuit components
3. Power electronics
4. Transmitter winding current and system frequency

The efficiency and the economic feasibility of the system dictates the practical implementation of the dynamic wireless charging system for public use. Therefore, the objective of the design process is to design a system with low power loss (the output power being fixed) and a low cost. The cost of the system has a direct correlation with the amount of material used. Hence, herein, it is assumed that the mass of the system serves as a proxy for the cost of the system.

The calculation of the mass and the power-loss occurring within the compensation circuit components and the power electronics have been explained in the previous sections. The calculation of the loss occurring within the transmitter and receiver involves a two-step procedure each of which requires finite element analysis:

1. Calculation of the inductance of the transmitter and receiver in order to calculate the receiver winding current
2. Calculation of the core loss and conduction loss occurring within the transmitter and receiver.

The inductance and the power loss occurring within the transmitter and the receiver are functions of the dimensions of the transmitter and receiver, the core material, the current within the windings, and the system frequency. The power loss and the mass of the compensation circuit components and the power electronic converters are functions of the transmitter and receiver inductance. Therefore, it is prudent to select the transmitter and receiver dimensions, the transmitter winding current and the system frequency as design variables.

Fig. 39 provides a view of the geometrical variables used in the design process.

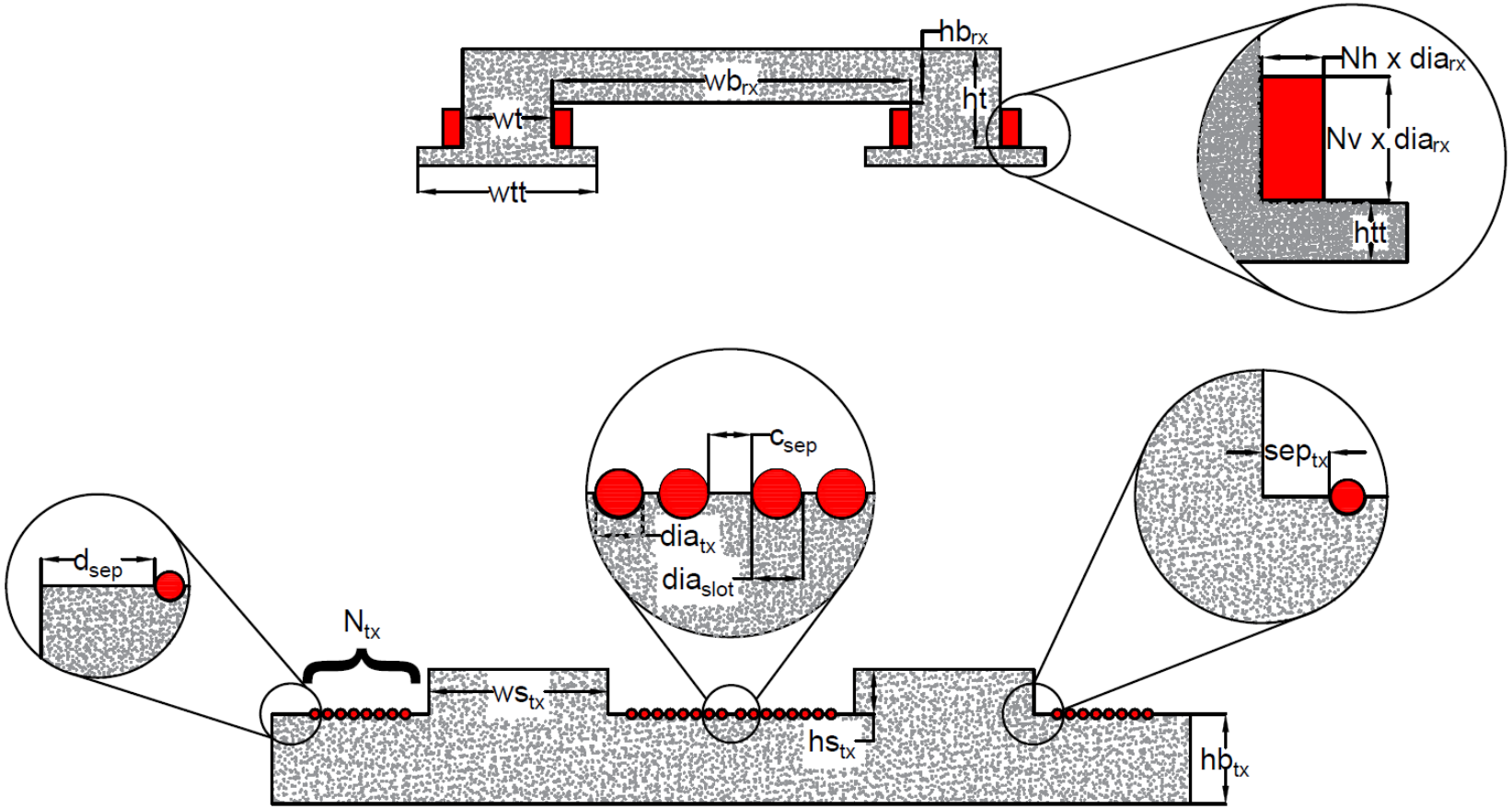

Figure 39. Transmitter and receiver geometrical design variables

Table 16. Design Variables

Type	Variable	Description
Geometrical	hb_{tx}	Height of the transmitter base
	hs_{tx}	Height of the transmitter stub
	ws_{tx}	Width of the transmitter stub
	sep_{tx}	Distance between the slot and transmitter stub
	d_{sep}	Distance between the transmitter edge and slot
	c_{sep}	Distance between the slots at the middle of the transmitter
	N_{tx}	Number of turns of the transmitter winding around a single stub
	dia_{tx}	Diameter of the transmitter winding
	s_{ratio}	Ratio of the transmitter slot diameter to winding conductor diameter
	wb_{rx}	Width of the receiver core base
	hb_{rx}	Height of the receiver core base
	wt	Width of the receiver core tooth
	ht	Height of the receiver core tooth
	wtt	Width of the receiver tooth tip
	htt	Height of the receiver tooth tip
	dia_{rx}	Diameter of the receiver winding conductor
	Nh	Number of receiver winding turns in the horizontal direction
	Nv	Number of receiver winding turns in the vertical direction
Electrical	I_{tx}	Transmitter winding current
	freq	Operating frequency of the system

The large number of design variables and the lack of functions that relate the objective functions and the design variables limits the use of derivative based methods for design optimization. Therefore, in order to develop a Pareto front consisting of non-dominant designs the genetic optimization toolbox - GOSET is employed.

6.1.1 Constraints

To ensure the feasibility of the designs constraints are imposed on the genetic optimization. These include:

1. $hb_{tx} > (0.5 \times s_{rat} \times dia_{tx})$

   This constraint is used to ensure that the diameter of the transmitter slot is less than the thickness of the transmitter base.

2. $wb_{tx} < 3.65\ m$

   The width of the transmitter is restricted to less than 3.65 m. This constraint is used to ensure that the transmitter can be accommodated within precast concrete slabs which has a width of 3.65 m (12 ft).

3. $(hb_{tx} + hs_{tx}) < 0.3\ m$

   This constraint is used to ensure that the transmitter can be accommodated within the precast concrete slabs by restricting the thickness of the transmitter to be less than that of the concrete slab which is assumed to be 0.3 m.

4. $w_{rtt} > \left(w_{rt} + 2 \cdot (Nh_{rx} \times dia_{rx})\right)$

   This constraint is used to ensure that the receiver winding can be placed securely on the receiver shoes.

5. $wb_{rx} > (w_{rtt} - w_{rt})$

   This constraint is used to ensure that the two shoes of the receiver core do not intersect thereby preventing the formation of a closed magnetic path for the receiver flux.

6. $(h_{rt} - hb_{rx}) > (Nv_{rx} \times dia_{rx})$

This constraint ensures that the height of the receiver coil is such that it can be accommodated in the receiver slot.

7. $J_{tx} < 7\ A/mm^2$

The transmitter winding current density is limited to 7 A/mm^2 to ensure that the winding does not overheat.

8. $T_{inv} < 150^{\circ}C$, $T_{rect} < 150^{\circ}C$

The junction temperature of the switching devices constituting the inverter and rectifier is constrained to be less than its rated temperature which is $150^{\circ}C$.

6.2 Results

The optimization of the entire DWPT system from the DC supply on the transmitter side to the rectifier and battery at the receiver end was performed with the aid of GOSET with a generation size of 200 and population size of 250. The desired output power of the design was set at 180 kW and the input voltage at the transmitter end was set at 500 V DC. This section puts forth the results obtained after the optimization and also discusses a few candidate designs.

Fig. 40 shows the Pareto optimal front obtained from the optimization. It can be observed that as the mass increases the power loss decreases. This reason behind this characteristic can be explained with the help of the following Figs. 41 and 42.

Fig. 41 and Fig. 42 show the contribution of the various types of losses to the overall system loss and the contribution of the mass of the various components to the system mass. It can be seen clearly that the contribution of the total core loss is higher in the lower efficiency designs. It can also be seen that the transmitter and receiver mass is much higher when compared to the compensation circuit and the power electronic converters. The increase in the mass of the transmitter and receiver corresponds to an increase in their respective volumes. As the volume increases the flux density decreases which results in a lower core loss.

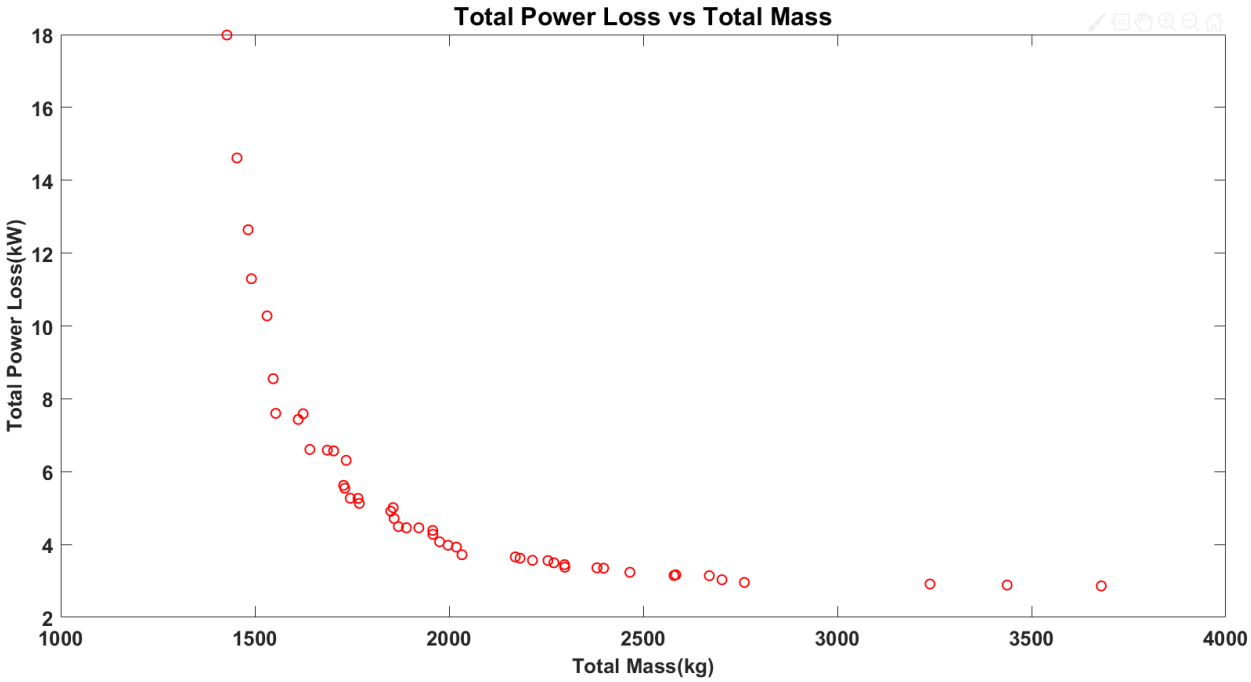

Figure 40. Pareto front (power loss vs system mass)

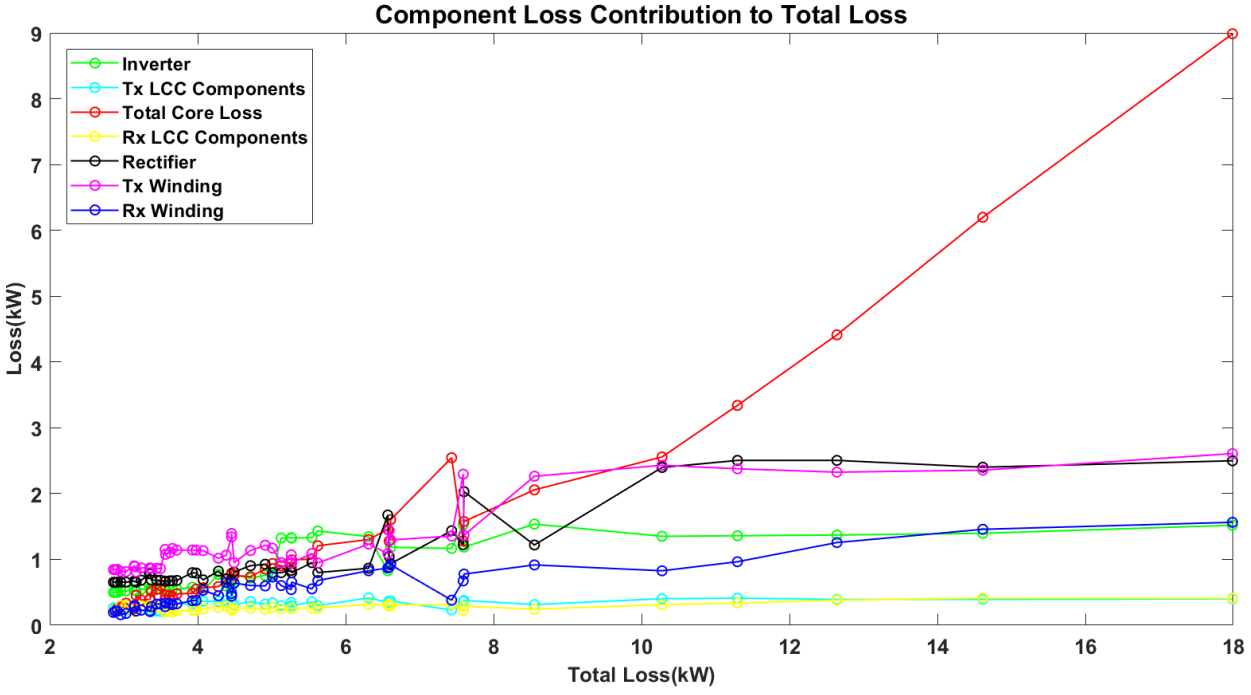

Figure 41. Power loss contribution

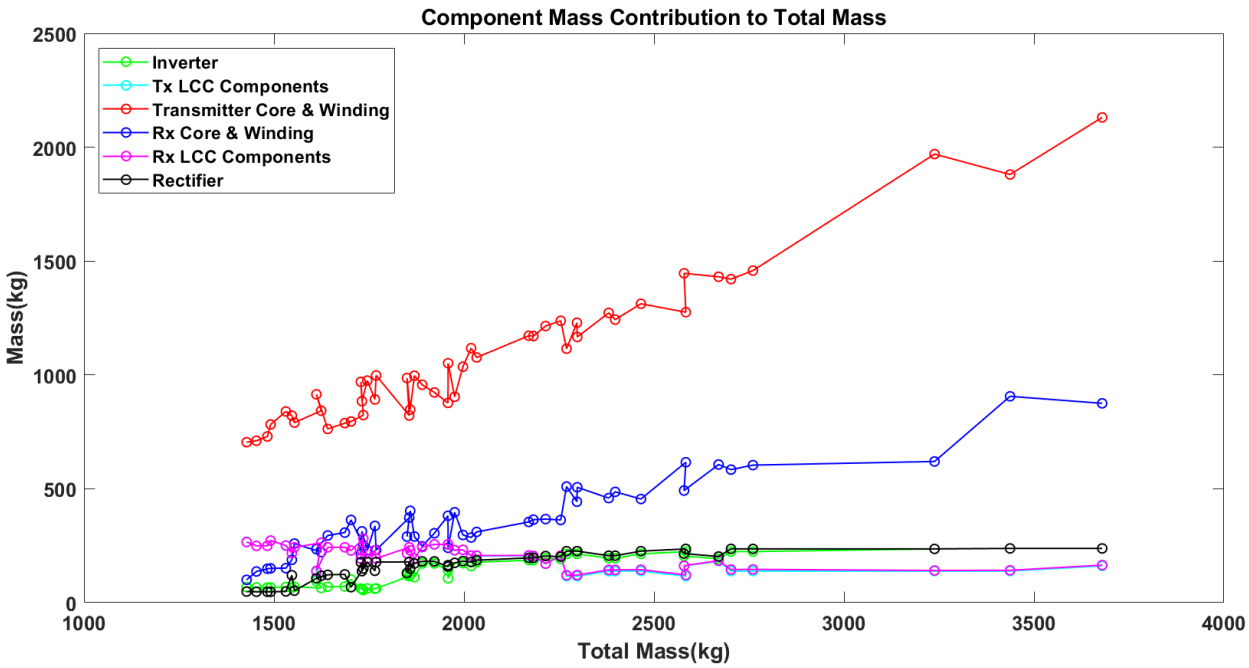

Figure 42. Mass contribution

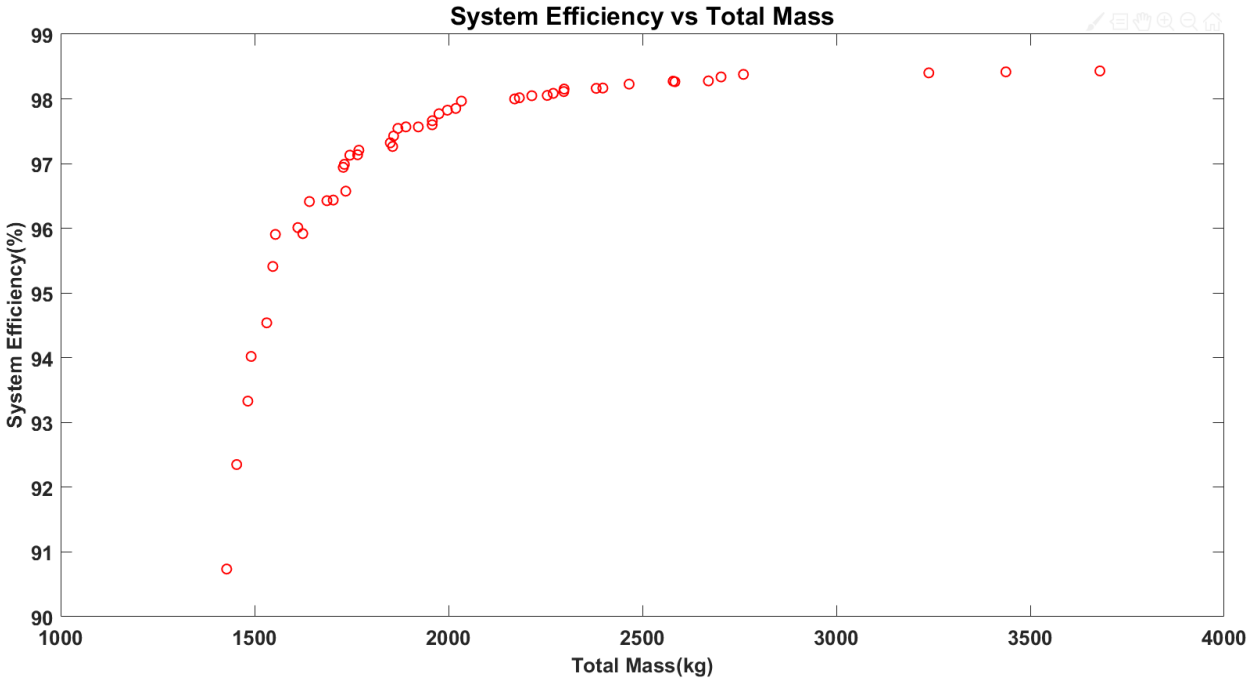

Figure 43. Efficiency vs mass

One of the most important features is the system efficiency. Fig. 43 gives an idea of how the efficiency of the system varies with the mass. It is clear from that as the mass increases efficiency of the system increases. The efficiency is calculated using.

$$\eta = \frac{P_{out}}{P_{out} + P_{loss}} \tag{209}$$

From (209) it is clear that the efficiency depends upon the output power and loss in the system. In this design optimization the output power is fixed, therefore efficiency is a function of power loss alone. Since the power loss decreases with an increase in mass the efficiency increases with mass. Another characteristic that is noticeable about the efficiency-mass curve is that the efficiency tends to saturate as the mass increases.

Fig. 44 shows the variation of the coupling co-efficient with system efficiency. From Fig. 41 it is evident that the leading contributor to the total power loss occurring in the system is core loss. Moreover, the output power delivered to the battery at the receiver end is independent of the coupling co-efficient. The coupling co-efficient is defined by (210) as:

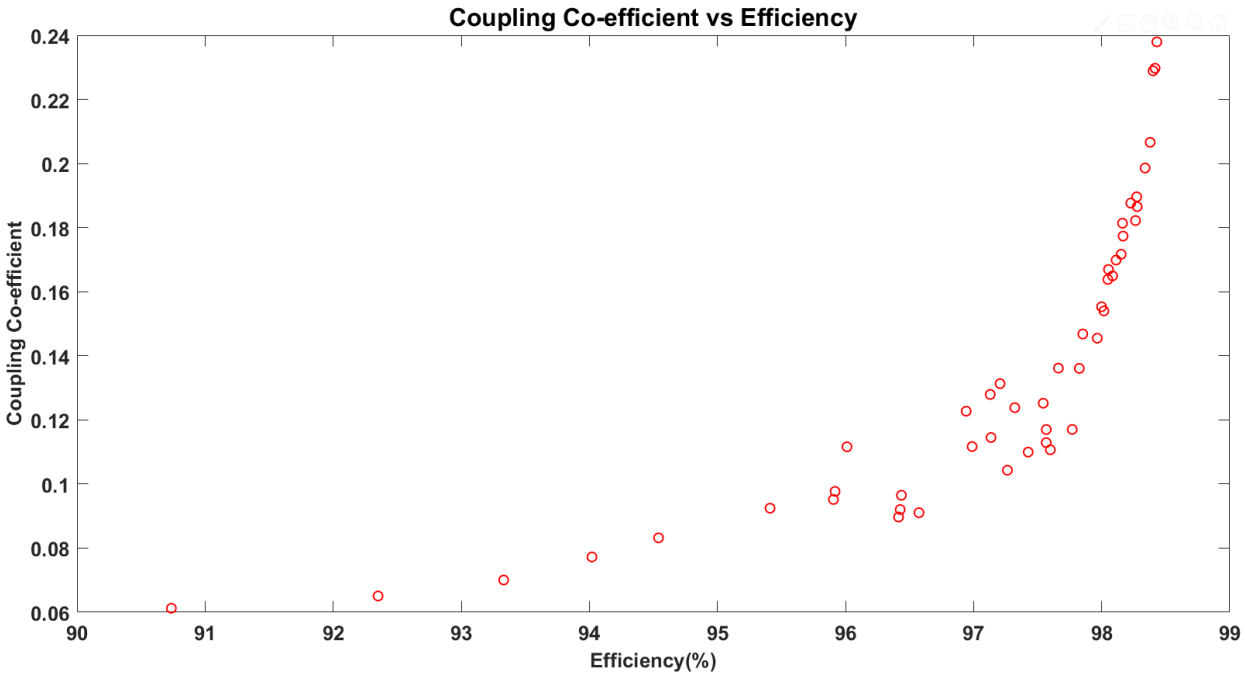

Figure 44. Coupling co-efficient vs efficiency

$$k = \frac{M}{\sqrt{L_{tx} L_{rx}}} \tag{210}$$

where,

M: Transmitter – receiver mutual inductance

L_{tx}: Transmitter self – inductance

L_{rx}: Receiver self – inductance

The coupling co-efficient is a measure of how much of the total generated flux links the receiver. Since the output power is almost constant and does not depend upon the coupling co-efficient, the only variable influencing the efficiency of the system is the power loss. A higher value of the coupling co-efficient implies that a higher percentage of the total flux generated by the transmitter/receiver links with the receiver/transmitter. Hence, the leakage flux is reduced which in turn results in a lower core loss. Therefore, Fig. 44 suggests that a system with a higher coupling co-efficient is more efficient compared to a system with a lower coupling co-efficient.

The ohmic loss associated with the transmitter winding is dependent upon the diameter of the transmitter winding conductor, the number of turns and the transmitter winding current. The length of the transmitter winding is directly proportional to the number of turns and the length of the transmitter core. Since the transmitter core length is fixed at 3.95 m, the only variable affecting the transmitter winding ohmic loss is the number of turns of the transmitter winding. Fig. 45 shows the variation of each of the above-mentioned parameters (normalized by their respective maximum values) with the ohmic loss occurring within the transmitter winding. The maximum value of each parameter is shown in the legend.

From Fig. 45, it can be seen that the number of turns vary between 3 and 4 and does not seem to vary much with increase in ohmic loss. On the other hand, the influence of the conductor diameter and current on the ohmic loss is more visible. The designs with a lower ohmic loss are characterized by larger conductor diameter and a lower current whereas the designs with a higher loss have lower conductor diameters and a higher current value.

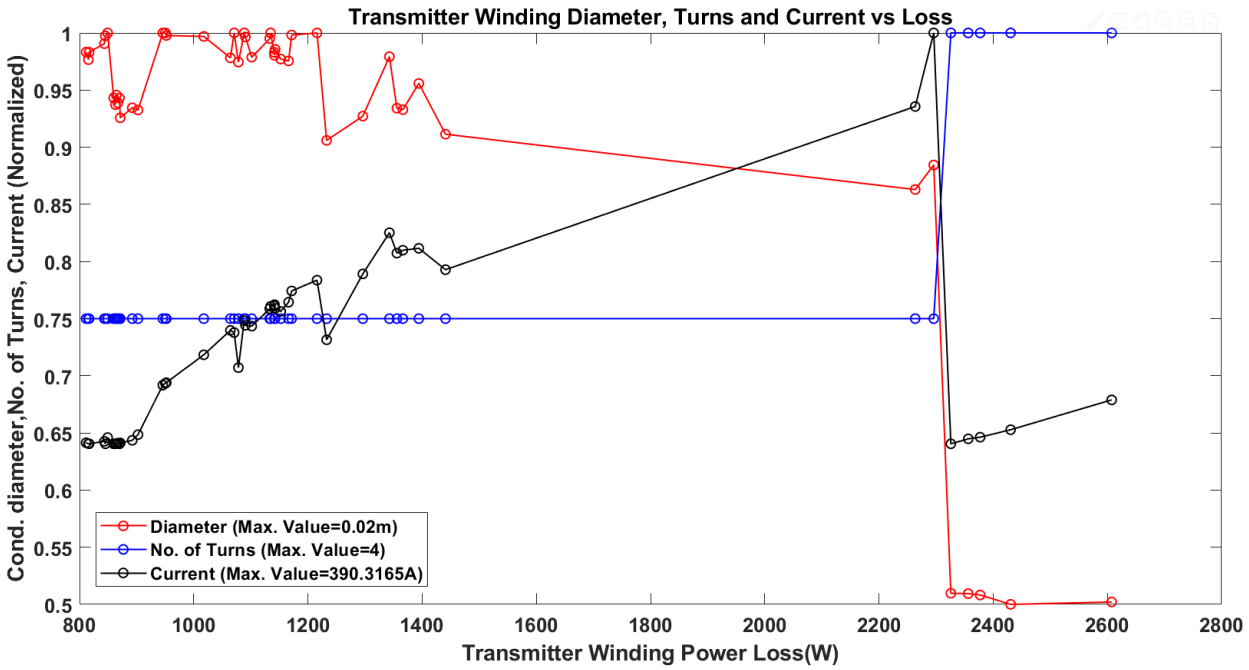

Figure 45. Transmitter winding parameters vs ohmic loss

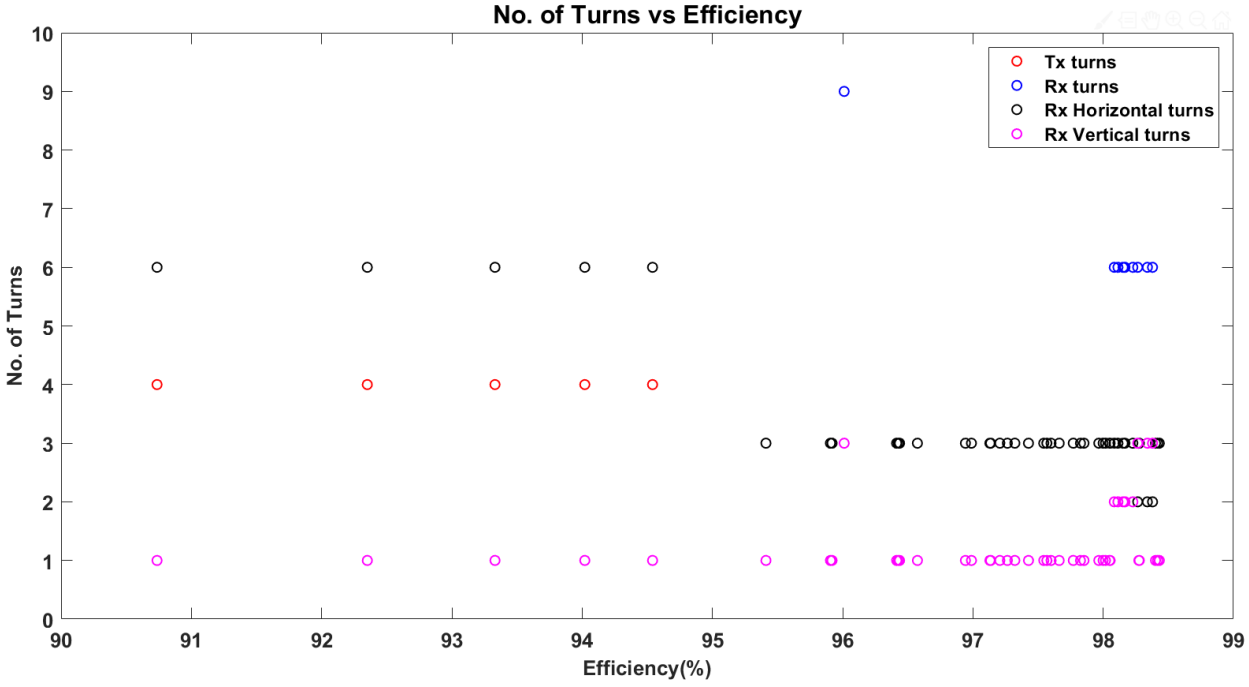

Figure 46. Number of turns vs efficiency

Fig. 46 shows the variation of the number of turns of the transmitter and receiver windings with the efficiency of the corresponding design. It is observed that the transmitter turns vary between 3 and 4. While most of the lower efficiency designs have 4 turns, the higher efficiency designs have a 3-turn transmitter. A higher number of turns results in a higher mass of the transmitter and also increases the ohmic loss. A higher number of turns also results in a larger core loss due to the large amount of leakage flux. Although the number of transmitter turns is low, it also seen that the optimization did not reduce the number of turns to its minimum value of 1. This is likely due to the fact that a lower number of turns would reduce the mutual inductance resulting in inadequate power transfer. A similar reasoning can be applied to explain the low number of receiver-turns. It can also be seen that the receiver winding has been arranged horizontally in most of the designs forming the Pareto front.

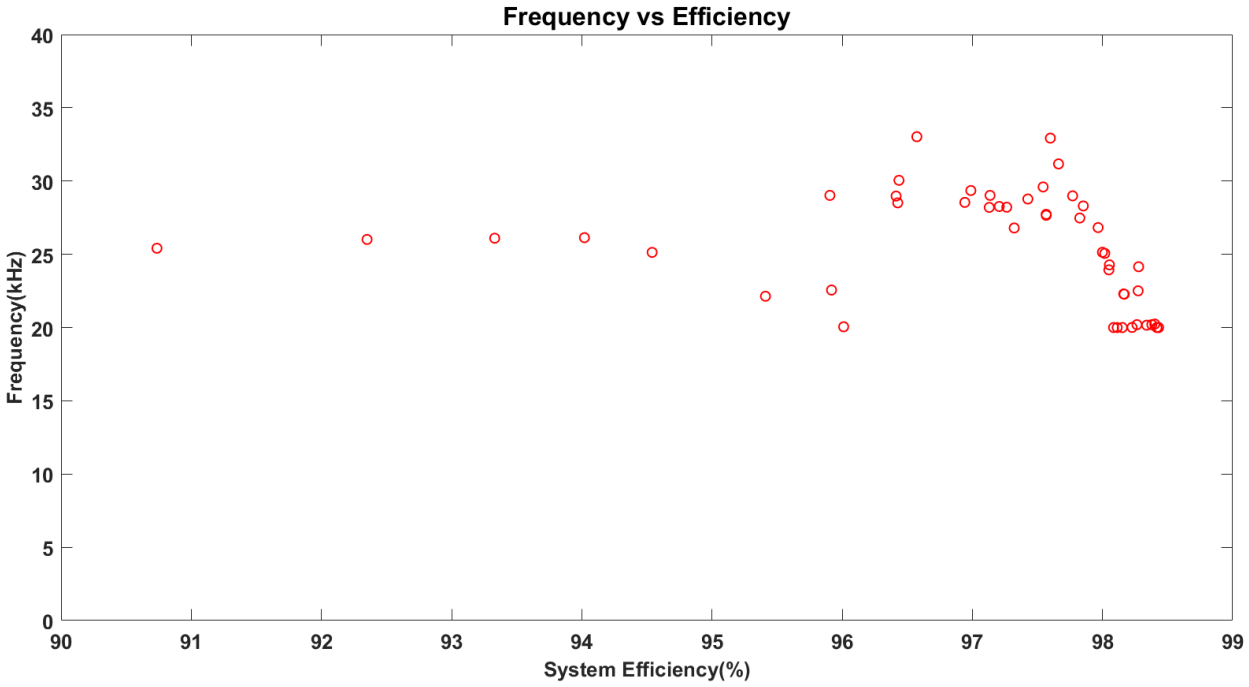

Figure 47. Switching frequency vs efficiency

One of the most important parameters of the DWPT system is the frequency of operation. In this optimization process the frequency of the system was a gene whose maximum and minimum values were 85 kHz and 20 kHz respectively. Fig. 47 shows the frequency of the designs in the Pareto front. It can be seen clearly that all the system frequencies are between 20 kHz and

32 kHz. It is observed that most of the highly efficient designs have frequencies closer to 20 kHz. This is once again explained by the fact that by reducing the frequency the core loss as well as the power electronic converter losses are reduced. An interesting observation is that the most efficient design has the lowest switching frequency.

An important parameter of the system is the length of the receiver core which was one of the genes used in the optimization. Fig. 48 shows the receiver core lengths of the designs forming the Pareto front. It is clear from Fig. 48 that the almost all designs have a core length close to 3m, which was the maximum value for this gene. A longer receiver core results in a larger amount of flux linking the receiver winding and hence a larger power transfer to the load. Therefore, in order to link the maximum amount of flux for any transmitter dimensions and current values the receiver needs to be made as long as possible.

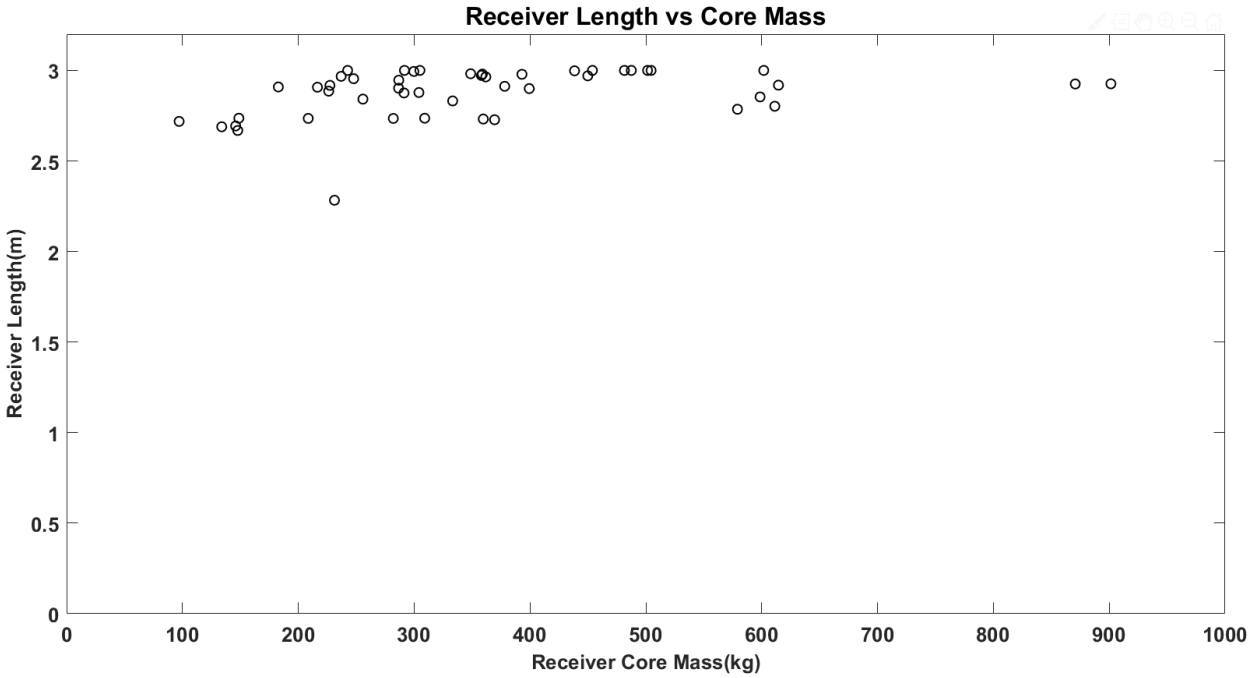

Figure 48. Receiver length vs efficiency

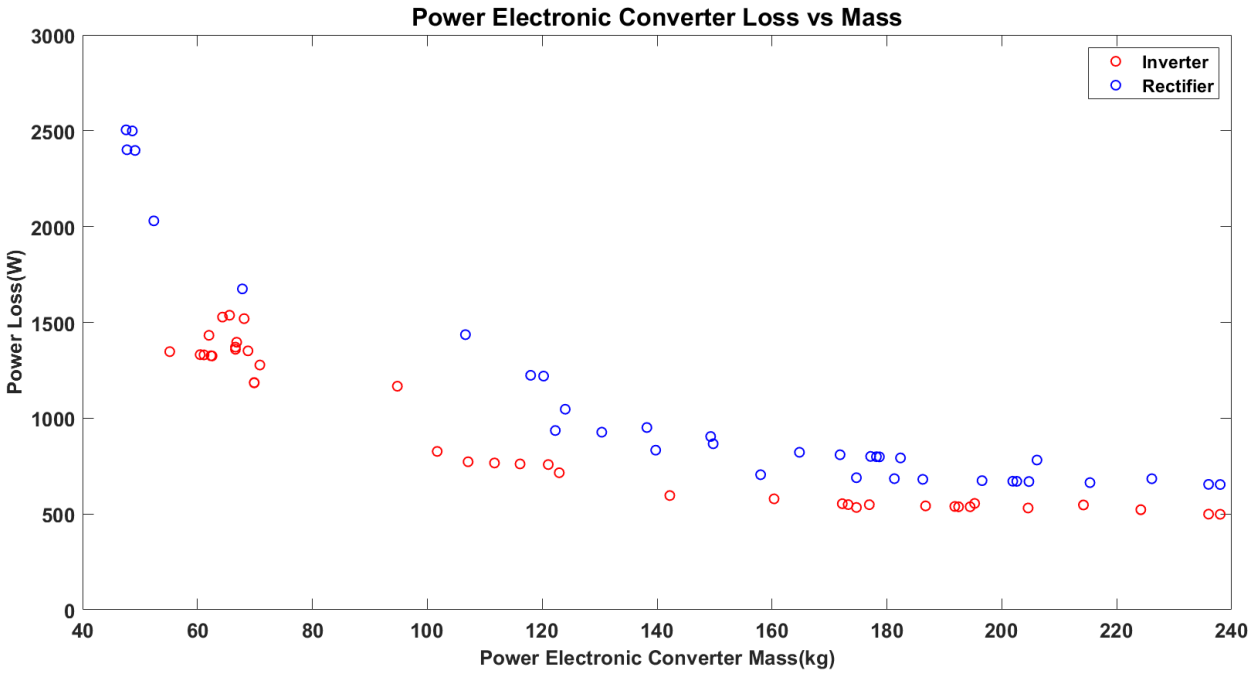

Figure 49. Power electronic loss vs mass

Fig. 49 shows the variations of the power loss occurring within the power electronic converters with the mass of the converter. It can be seen that as the mass of the converter increases the power loss decreases. It is also observed that for all designs the rectifier loss is higher than the inverter loss. The reason behind both these characteristics can be observed from Figs. 50 and 51.

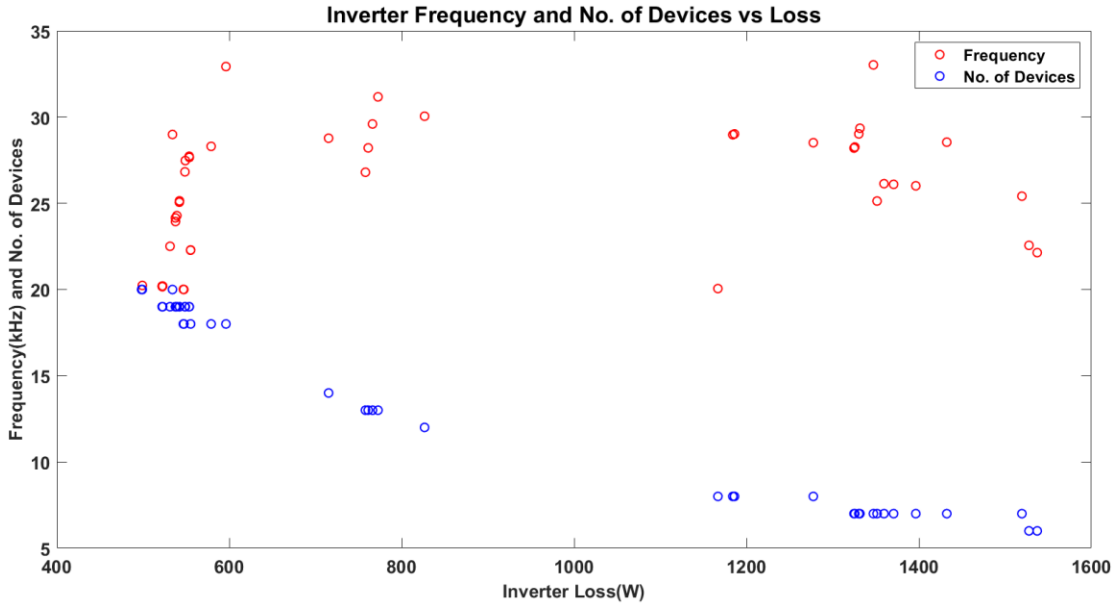

Figure 50. Inverter frequency and no. of devices vs loss

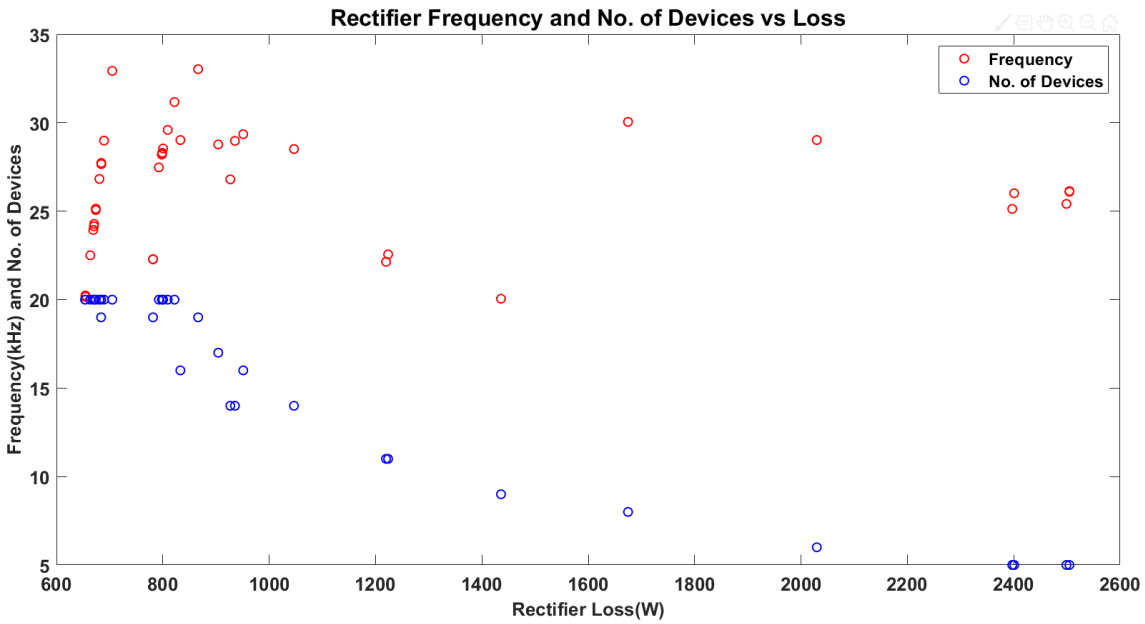

Figure 51. Rectifier frequency and no. of devices vs loss

Figs 50 and 51 shows the variation of switching frequency and number of devices with the converter power loss for the inverter and rectifier respectively. Comparing the figures, it can be seen that for low power loss designs the number of the devices in both the rectifier and the inverter are close to their maximum allowed value of 20. This results in a high mass and lower power loss since a higher number of devices means that one device needs to handle lower value of current thereby reducing the conduction loss. Furthermore, it is also observed that the number of devices constituting the inverter is generally higher compared to the number of devices in the rectifier. This results in a larger power loss in the rectifier and a lower power loss in the inverter. Furthermore, the dc voltage at the output side of the rectifier is 450 V and that at the input side of the inverter is 500 V. As a result, the inverter current is lower than the rectifier current and hence the inverter loss is generally lower than the rectifier loss.

In order to understand the key differences between the designs with the best and worst efficiency a comparison is now provided. Fig. 52 shows the most efficient design (henceforth referred to as design 1) obtained from the Pareto front.

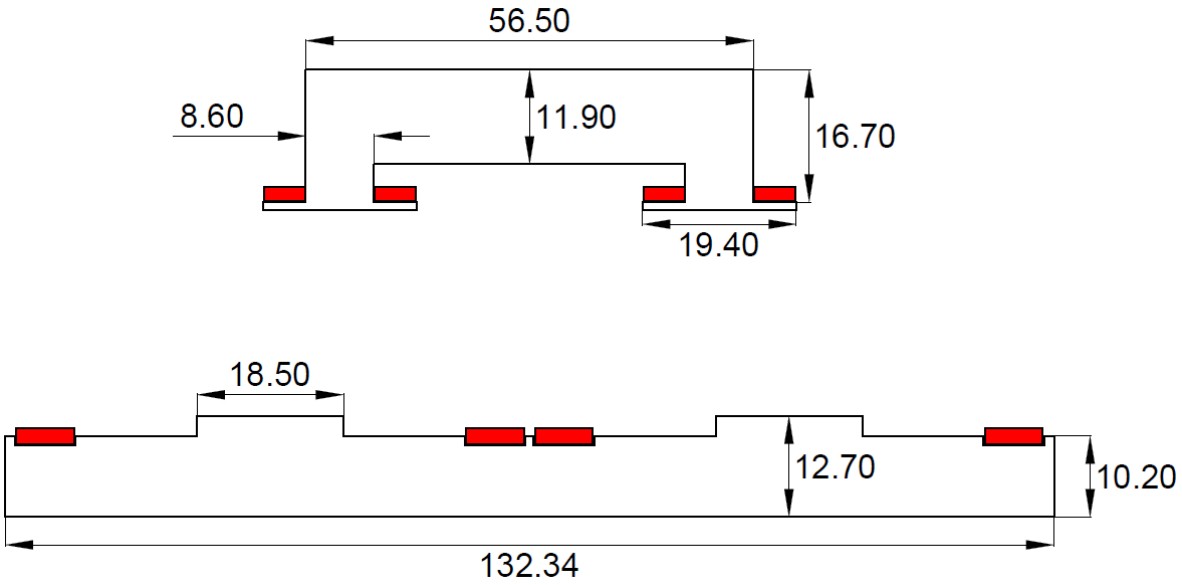

Figure 52. Design 1 dimensions

All dimensions in Fig. 52 are in centimeters. Design 1 has an efficiency of 98.43 %. This design has a. RMS transmitter winding current of 250 A and an inverter switching frequency of 20 kHz. It is to be noted that 20 kHz is the minimum allowed value of the inverter switching frequency. The diameter of the transmitter winding conductor for this design is 0.02 m, which is the maximum allowed value for the transmitter winding diameter. The high value of the conductor diameter results in a an extremely low value of transmitter winding loss. Furthermore, the receiver teeth have been aligned almost right on top of the transmitter stubs. It is noted that this feature was not specified as a constraint in the optimization and hence is a feature attained simply by the design process. Since the transmitter width is only 1.32 m and the total height is 0.102 m, it is readily accommodated within a concrete slab.

Fig. 53 and Fig. 54 show the flux density magnitude and flux density vectors for the design shown in Fig. 52. It can be seen that most of the flux generated by both the transmitter and receiver contributes to leakage and only fraction contributes to the mutual flux. Most the flux generated by the transmitter is concentrated in the middle region resulting in much less core loss. It can also be verified from Fig. 53 that the flux density at a distance of 0.8 meters(at the left and right ends of the figure) are well below 26 μT as required by ICNIRP guidelines.

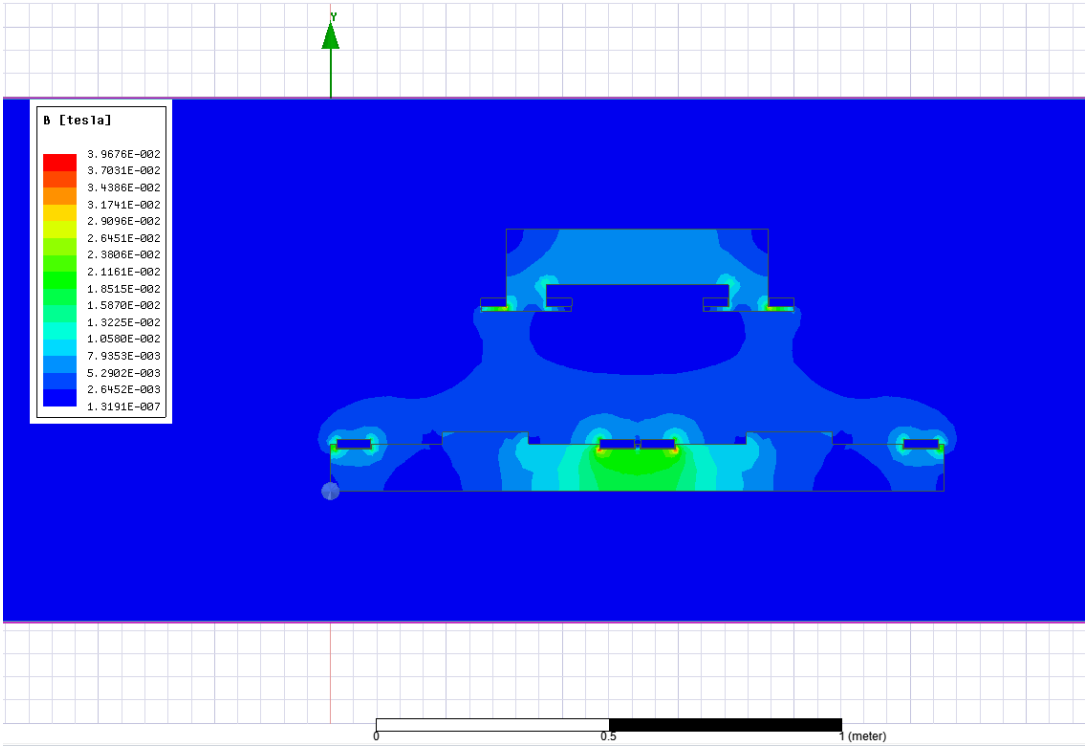

Figure 53. Flux density magnitude for design 2

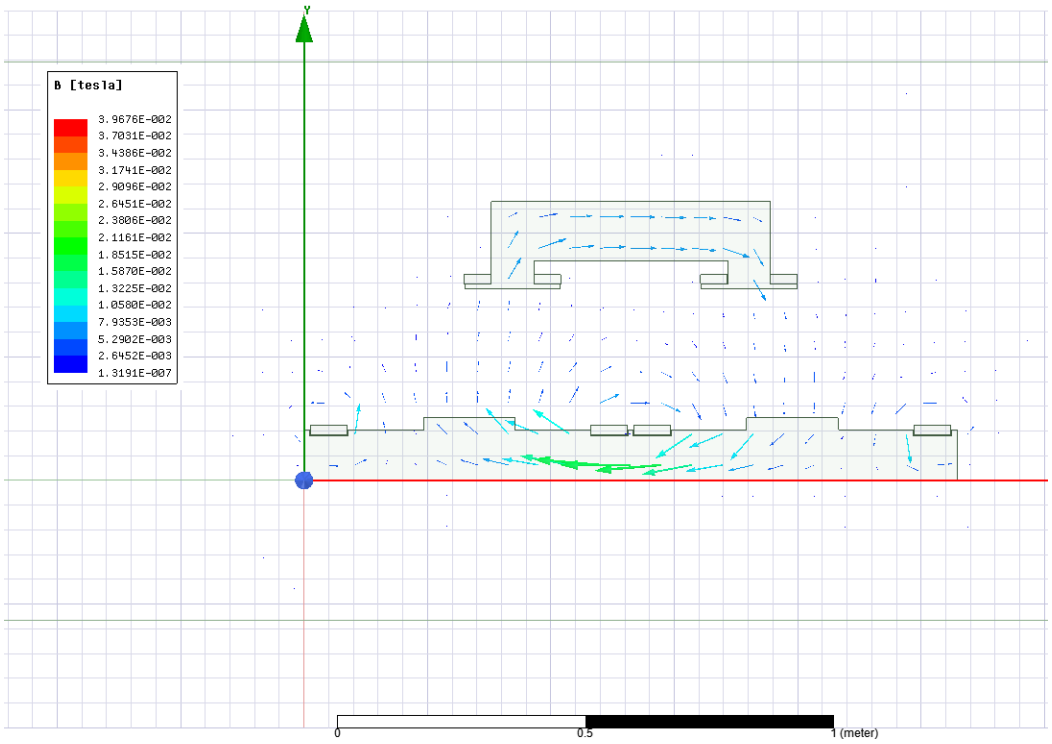

Figure 54. Flux density vector plot for design 2

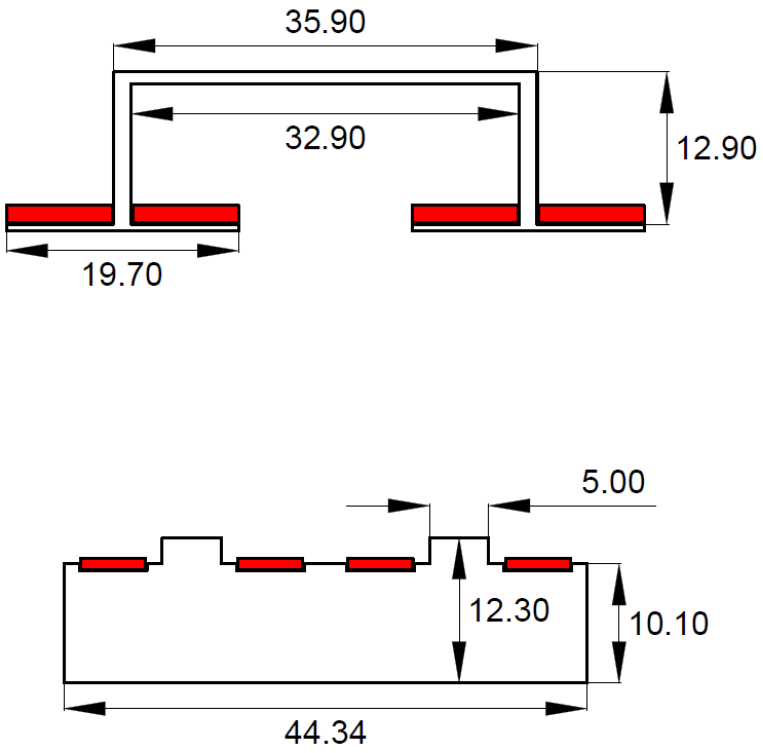

Figure 55. Design 49 dimensions

Fig. 55 shows the dimensions of the least efficient design (henceforth referred to as design 49), with an efficiency = 90.74%. All dimensions shown in Fig. 55 are in centimeters and the gene values for this design in shown in Table 17. The stark contrast between the design in Fig. 52 and Fig. 55 is visible. The transmitter winding diameter of 0.013 m combined with a current of 265 A results in a larger ohmic loss compared to design 1. The receiver core in of design 49 is in stark contrast with the receiver of design 1. The receiver base of design 49 has a very low height (= 0.010 m) resulting in large core loss. The complete alignment of the receiver tooth and the transmitter stubs indicate that this design should have a high mutual inductance, but the low height of the receiver base presents a high reluctance to the mutual flux. This results in a large share of the flux being leakage flux which in turn results in a large core loss. This can be confirmed from Fig. 56 and Fig. 57 show the flux density magnitude and vector plots respectively.

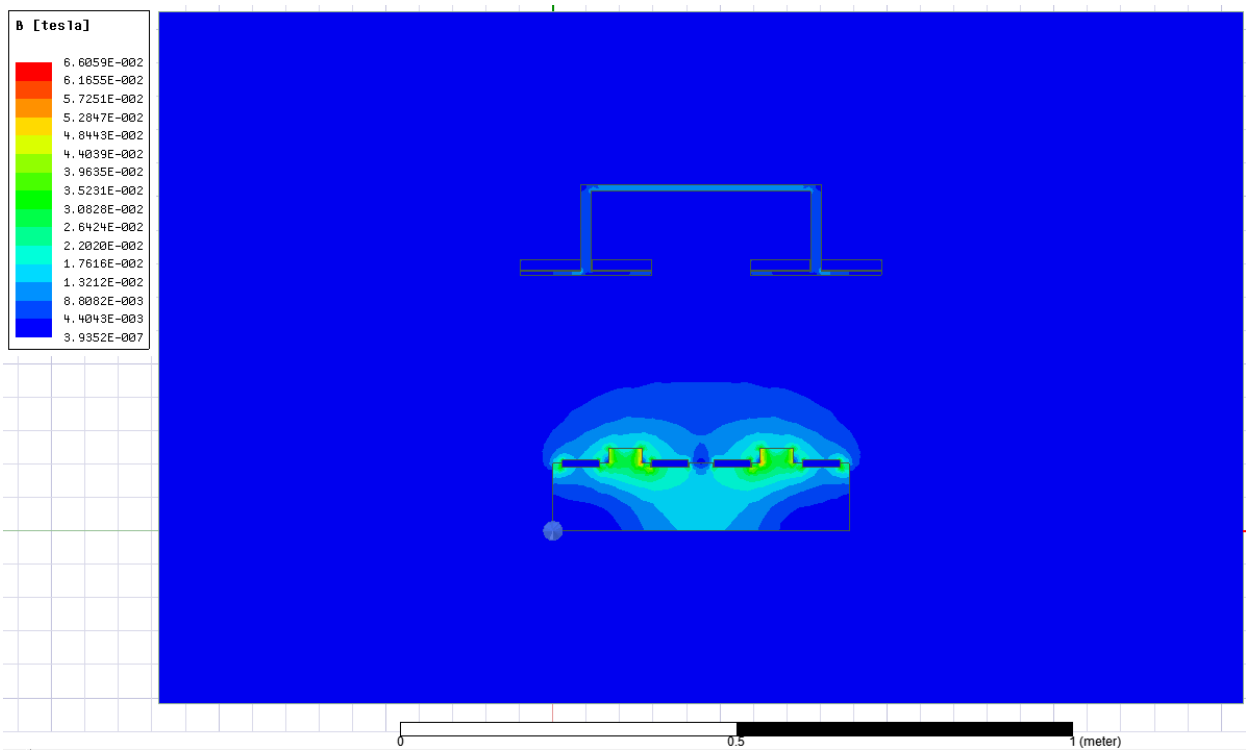

Figure 56. Flux density magnitude plot for design 49

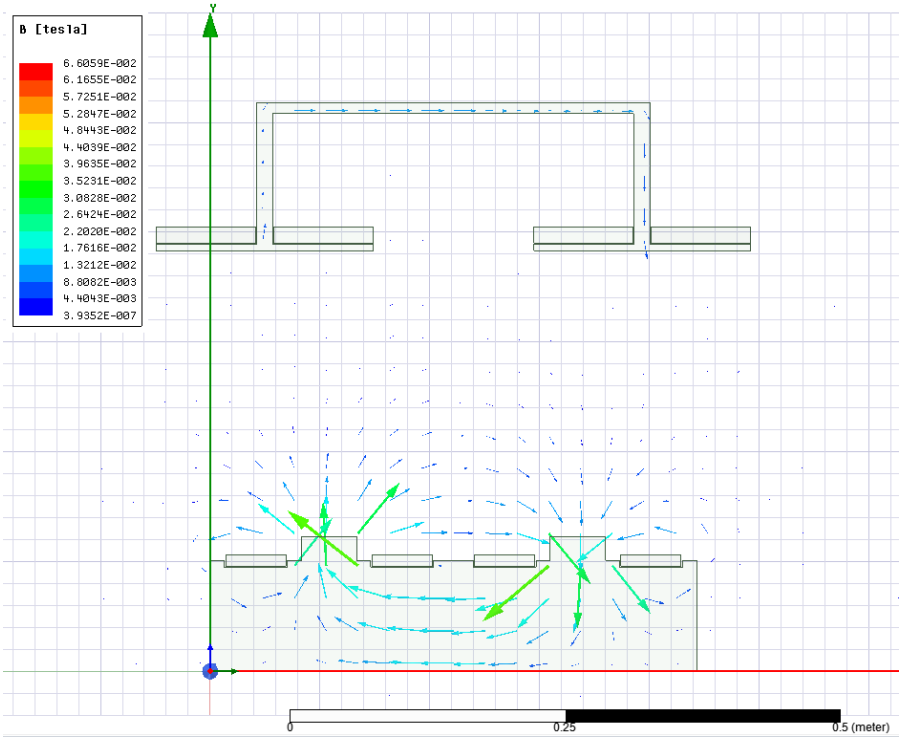

Figure 57. Flux density vector plot for design 49

It can be observed from Fig. 56 and Fig. 57 that the fraction of the flux that contributes to the mutual inductance is extremely small compared to the design 1. Almost all the flux contributes to leakage flux. This fact combined with the smaller geometry of the transmitter and receiver results in drastic decrease in efficiency. From Figs. 52 and 55 it is evident that the size of the transmitter and receiver core play a huge role in the efficiency of the design.

While design 1 has an efficiency of 98.43% the total mass of the design is 3679 kg. The mass of the transmitter and receiver alone is 2955 kg. This results in a high manufacturing cost. On the other hand, design 49 has a total mass of 1428 kg with the transmitter and receiver weighing only 778 kg. But design 49 suffers from an extremely low efficiency. From Fig. 43 it is clear that a compromise must be made between efficiency and mass/cost of the design. Therefore, design 29 which is closer to the knee of the pareto curve shown in Fig. 58 is chosen. Fig. 58 shows the relevant dimensions of design 29.

Design 29 has an efficiency of 97.32% but weighs only 1858 kg. The transmitter and receiver mass contributes about 1228 kg. This is a huge reduction in mass and hence cost, with minimal reduction in the efficiency. The transmitter current for design 29 is 305.9 A and the inverter switching frequency is 26.8 kHz. The transmitter winding diameter for design 10 is 0.02 m which is instrumental in reducing the ohmic loss in the transmitter winding.

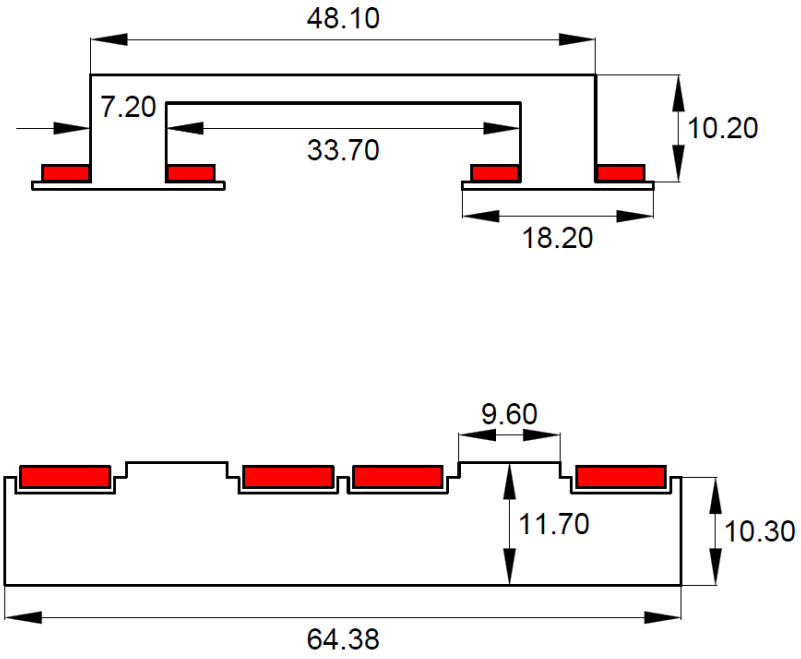

Figure 58. Design 29 dimensions

The values of the design variables for design 1, 49 and 29 have provided in Table 17.

Table 17. Gene/Design Variable of designs

Genes/Design Variables	**Design 1**	**Design 49**	**Design 29**
hb_{tx}	0.102 m	0.101 m	0.103 m
hs_{tx}	0.025 m	0.022 m	0.014 m
ws_{tx}	0.185 m	0.05 m	0.096 m
sep_{tx}	0.153 m	0.013 m	0.011 m
d_{sep}	0.012 m	0.013 m	0.01 m
c_{sep}	0.01 m	0.036 m	0.01 m
N_{tx}	3	4	3
dia_{tx}	0.02 m	0.01 m	0.02 m
s_{ratio}	1.191	1.231	1.484
wb_{rx}	0.393 m	0.329 m	0.337 m
hb_{rx}	0.119 m	0.01 m	0.027 m
wt	0.086 m	0.015 m	0.072 m
ht	0.167 m	0.129 m	0.102 m
wtt	0.194 m	0.197 m	0.182 m
htt	0.01 m	0.006 m	0.007 m
dia_{rx}	0.018 m	0.015 m	0.016 m
Nh	3	6	3
Nv	1	1	1
I_{tx}	250 A	265 A	305.8 A
freq	20 kHz	25.4 kHz	26.8 kHz
len_{rx}	2.9 m	2.7 m	2.9 m
No. of Inverter Devices	20	7	13
No. of Rectifier Devices	20	5	14

Table 18 gives the values of the compensation circuit components, their mass and volume and the mass and volume of the power electronic converters and the mass of the receiver and the transmitter for designs 1, 49 and 29.

Table 18. Component Values, Mass and Volume for designs

Components	**Design 1**	**Design 49**	**Design 29**
Lf_1	0.0143 mH	0.0106 mH	0.0087 mH
Cf_1	4.4199 μF	3.6891 μF	4.0360 μF
C_1	0.3080 μF	0.1588 μF	0.2846 μF
L_{11}	0.2201 mH	0.2582 mH	0.1328 mH
M	0.0435 mH	0.0180 mH	0.0168 mH
L22	0.1519 mH	0.3336 mH	0.1378 mH
C2	0.4974 μF	0.1216 μF	0.2794 μF
Cf2	2.586 μF	3.6618 μF	3.0576 μF
Lf2	0.0244 mH	0.0107 mH	0.0115 mH
Mass Lf_1	7.39 kg	6.25 kg	4.92 kg
Mass Cf_1	41.43 kg	43.16 kg	44.89 kg
Mass C_1	112.22 kg	217.54 kg	165.75 kg
Mass of transmitter	2084.66 kg	681.10 kg	942.08 kg
Mass of Receiver	870.66 kg	97.08 kg	286.56 kg
Mass C2	24.17 kg	207.18 kg	75.97 kg
Mass Cf2	41.43 kg	43.16 kg	43.16 kg
Mass Lf2	13.78 kg	6.61 kg	7.19 kg
Mass of Inverter	238 kg	68.12 kg	121.05 kg
Mass of Rectifier	238 kg	48.65 kg	130.36 kg
Volume Cf1	0.0456 m^3	0.0475 m^3	0.0494 m^3
Volume C1	0.1220 m^3	0.2365 m^3	0.1802 m^3
Volume C2	0.0266 m^3	0.228 m^3	0.0836 m^3
Volume Cf2	0.0456 m^3	0.0475 m^3	0.0475 m^3

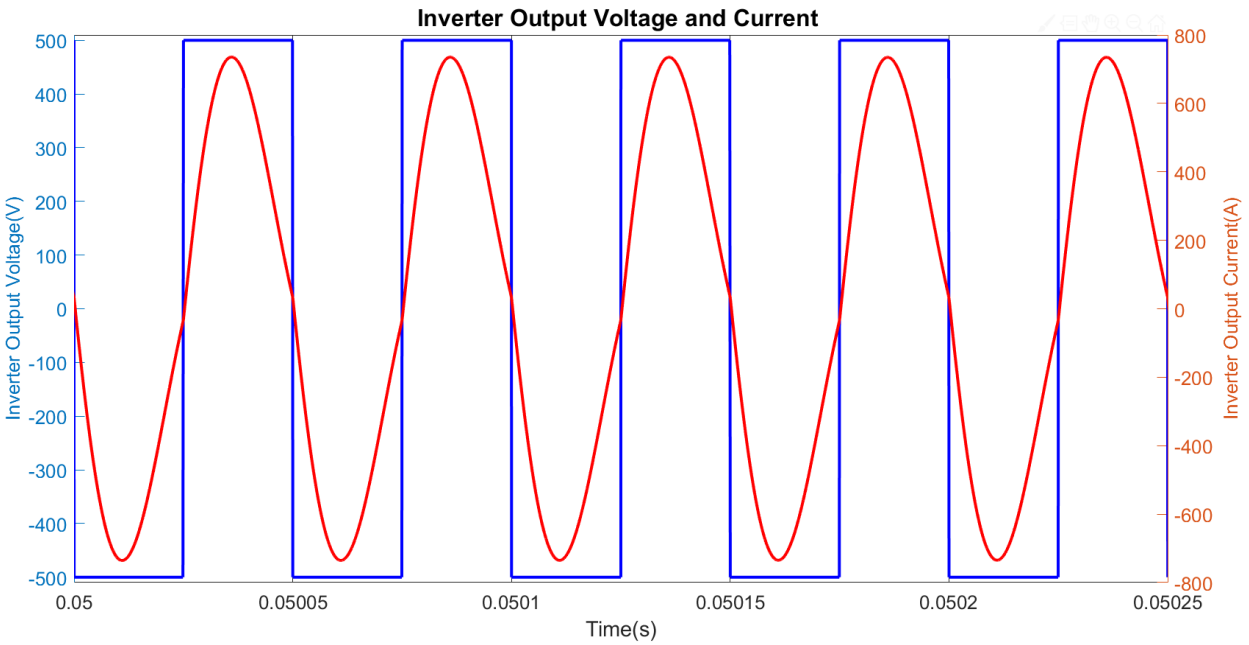

Figure 59. Inverter output voltage and current

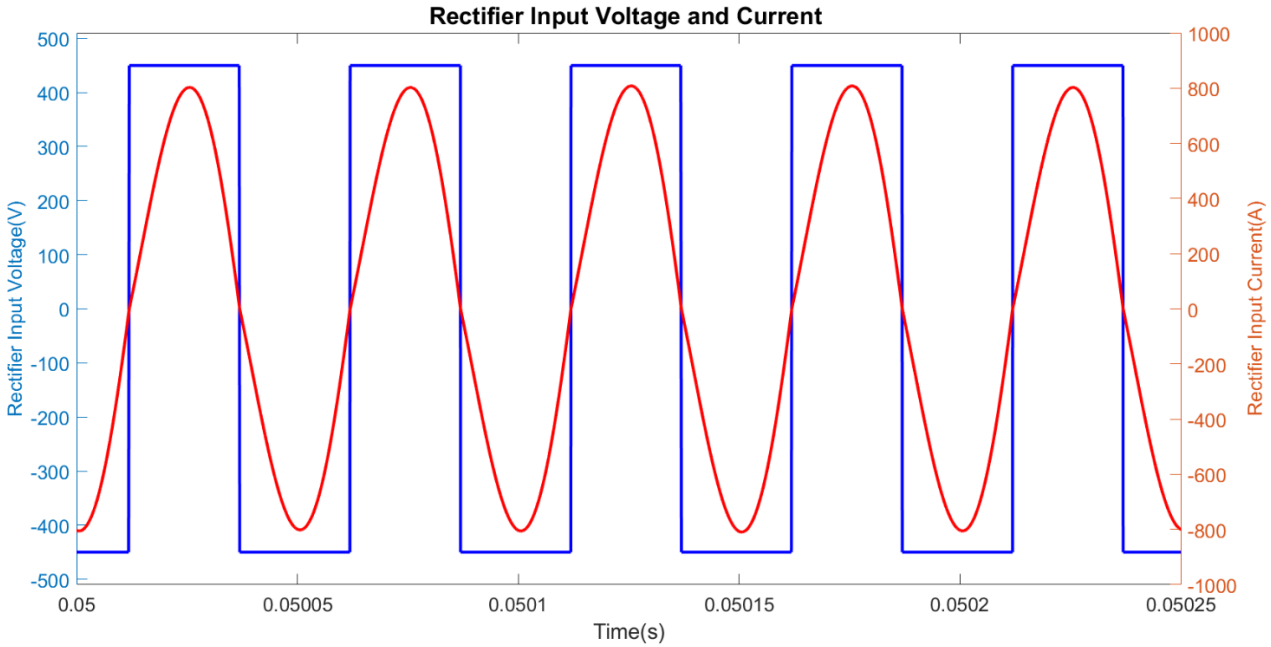

Figure 60. Rectifier input voltage and current

Fig. 59 – 62 shows the results of a dynamic simulation of the circuit conducted using SIMULINK. Fig. 59 shows the inverter output voltage and current and Fig. 60 shows the rectifier input voltage and current. It can be seen that in both cases the current and voltage are in phase. The inverter output current displays a slight distortion due to the presence of harmonics. The rectifier input current on the other hand seems almost sinusoidal.

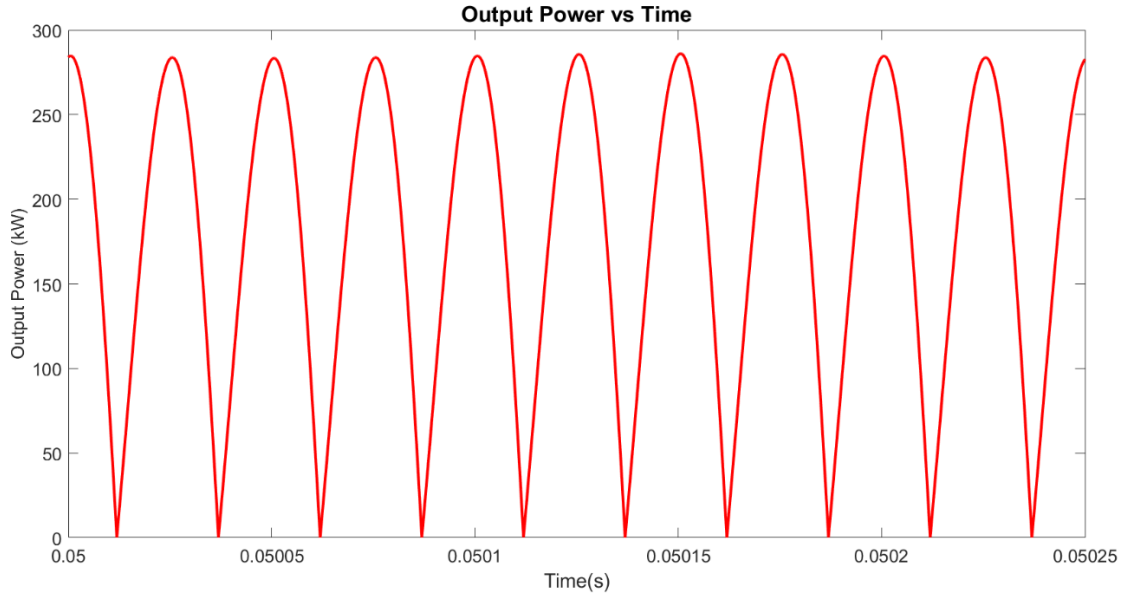

Figure 61. Output power supplied to vehicle battery

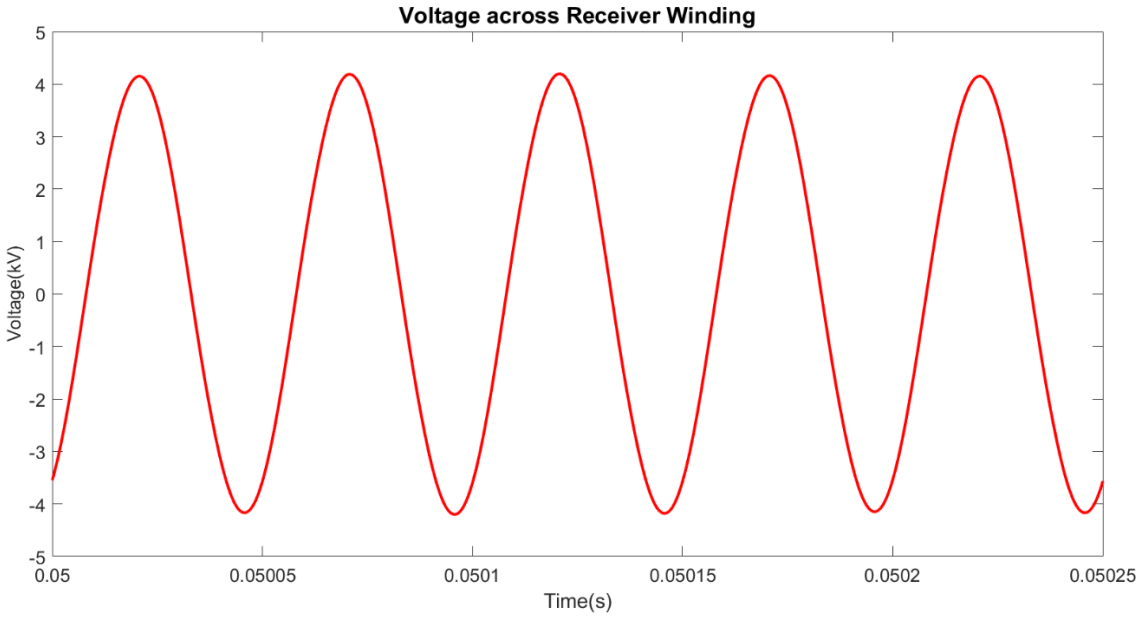

Figure 62. Voltage across receiver winding

Fig. 61 shows the variation of the power delivered to the 450 V battery at the receiver side. It can be seen that the required amount of dc power ≈ 180 kW is supplied to the battery. Fig. 62 shows the voltage occurring across the receiver winding. It can be seen that the magnitude of this voltage reaches almost 5 kV. This high voltage presents a safety hazard to the drivers. A strategy to combat this high voltage hazard has been shown in Fig. 63 [4].

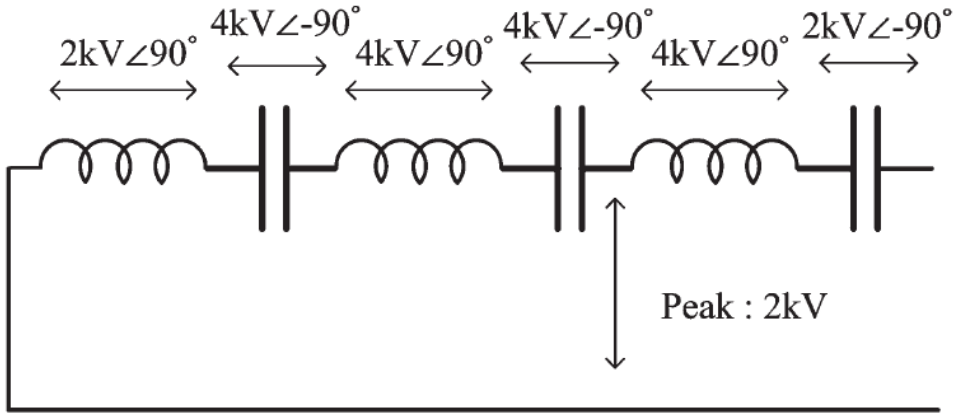

Figure 63. Winding voltage mitigation strategy [4]

In Fig. 63 the receiver winding and the series capacitor bank has been split up. It can be seen that the voltage across the capacitor and across split receiver turns have a phase difference of 180 degrees. This results in the cancellation of the voltage generated across the split receiver turns by the capacitor voltage. As a result, the voltage between the any point in the receiver winding and the reference/ground is limited to 2 kV. It must be noted that each capacitor shown in Fig. 64 is composed of multiple individual capacitors.

7. CONCLUSION

This research introduces a genetic optimization based method to determine the size of the transmitter and receiver and also the mass and power loss of the compensations circuit components and the power electronic converters. The Pareto optimal front obtained from the optimization presents a series of designs which vary from a high mass (and hence high cost) - high efficiency design to a low mass low – low efficiency design. Therefore, an informed compromise can be made between efficiency and cost while selecting a design. Although the study conducted is assumed to deliver a power of 180 kW (sufficient for a class 9 truck to maintain its state of charge), a similar study can be conducted for other power levels. Compared to [4], [5] and [6] which have developed different designs for IPT based DWPT systems, this study puts forth a method which optimizes the entire system including the compensation circuit and power electronics converters. The results obtained from the study show the dependence of the various kinds of power loss on the different parameters such as the dimensions of the transmitter and receiver cores, number of turns of transmitter and receiver winding, and the switching frequency of the inverter.

The method adopted in this research can be used to perform a number of further research studies instrumental in the development of IPT based DWPT systems. In this research the receiver is assumed to be perfectly aligned with the transmitter. In a practical scenario the lateral movement of the vehicle will cause misalignment of the receiver will result in a variation of the mutual inductance value and hence a variation in the power delivered to the receiver. The effect of lateral misalignment can be incorporated into optimization study thereby developing designs which are less susceptible to lateral misalignment. A comparative study can also be conducted which would compare the different geometries such as the E-type, I-type, and S-type transmitters described in [4], [5] and [6] to determine which geometry is best suited for IPT application. A larger generation and population size can be used to arrive at a wider array of optimal designs. Using a higher value of generations and population size a more continuous variation in efficiency can be obtained and better designs may be generated since the search space is utilized more rigorously. Finally, the FEA can be replaced by another method such as the method of moments which may prove to be computationally less time consuming.

REFERENCES

[1] Ltd., M. (2019, September 07). Internal Combustion Engines (ICE) counted for over 90% of global car sales in H1 2019. Retrieved from https://www.jato.com/internal-combustion-engines-ice-counted-for-over-90-of-global-car-sales-in-h1-2019/

[2] Wells to wheels: Electric car efficiency. (2017, April 08). Retrieved from https://matter2energy.wordpress.com/2013/02/22/wells-to-wheels-electric-car-efficiency/#:~:text=Quite%20well%20in%20fact.,at%20turning%20energy%20into%20motion.

[3] Roadway Powered Electric Vehicle Project: Track construction and testing program, Phase 3D. (1994). Berkeley, CA: California PATH Program, Institute of Transportation Studies, University of California, Berkeley.

[4] Shin, J., Shin, S., Kim, Y., Ahn, S., Lee, S., Jung, G., Jeon, S. J., and Cho, D. H. (2014). Design and Implementation of Shaped Magnetic – Resonance – Based Wireless Power Transfer System for Roadway – Powered Moving Electric Vehicles. IEEE Transactions on Industrial Electronics, 61(3), 1179 – 1192, doi: 10.1109/tie.2013.2258294

[5] Huh, J., Lee, S. W., Lee, W. Y., Cho, G. H., and Rim, C. T. (2011). Narrow – Width Inductive Power Transfer System for Online Electrical Vehicle. IEEE Transactions on Power Electronics, 26(12), 3666 – 3679, doi: 10.1109/tpel.2011.2160972

[6] Choi, S. Y., Jeong, S. Y., Gu, B. W., Lim, G. C., and Rim, C. T. (2015). Ultraslim S – Type Power Supply Rails for Roadway – Powered Electric Vehicles. IEEE Transactions on Power Electronics, 30(11), 6456 – 6468. doi:10.1109/tpel.2015.2444894

[7] Lu, F., Zhang, H., Hofmann, H., and Mi, C. (2015). A Double – Sided LCLC – Compensated Capacitive Power Transfer System for Electric Vehicle Charging. IEEE Transactions on Power Electronics, 30(11), 6011 – 6014. doi: 10.1109/tpel.2015.2446891

[8] Budhia, M., Boys, J. T., Covic, G. A., and Huang, C. (2013). Development of a Single – Sided Flux Magnetic Coupler for Electric Vehicle IPT Charging Systems. IEEE Transactions on Industrial Electronics, 60(1), 318 – 328. doi: 10.1109/tie.2011.2179274

[9] Esguerra, M. (2019, September 03). Downloads. Retrieved from https://www.magment.de/en-downloads-blog/2019/9/03-magment-wireless-charging-broschure-iaa-edition

[10] Magnetic Concrete MC. (n.d.). Retrieved from https://www.magment.de/en-magnetic-concrete-mc

[11] New England Wire Technologies – Pioneering in Litz for H.F. magnetic winding. (n.d.). Retrieved from http://litzwire.com/nepdfs/Round_Litz_Catalog.pdf

[12] Sudhoff, S. D. (2014). Power magnetic devices: A multi-objective design approach. Hoboken, NJ: John Wiley & Sons.

[13] Li, S., Li, W., Deng, J., Nguyen, T. D., and Mi, C. C. (2015). A Double – Sided LCC Compensation Network and Its Tuning Method for Wireless Power Transfer. IEEE Transactions on Vehicular Technology. 64(6), 2261–2273. doi: 10.1109/tvt.2014.2347006

[14] Sudhoff, S. D., Shane, G. M., and Suryanarayana, H. (2013). Magnetic – Equivalent – Circuit – Based Scaling Laws for Low – Frequency Magnetic Devices. IEEE Transactions on Energy Conversion, 28(3), 746 – 755. doi: 10.1109/tec.2013.2271976

[15] High Voltage Filter Capacitors STHVF. (n.d.). Retrieved from https://www.filmcapacitor-st.com/product.php?id=High-Voltage-Filter-Capacitors

[16] Krause, P. C., Wasynczuk, O., Sudhoff, S. D., and Pekarek, S. (2013). Analysis of electric machinery and drive systems. Hoboken, NJ: John Wiley & Sons.

[17] Pekarek, S., and Benavidez N. (personal communication) about characterization of PCKA inverter.